39'82

Attention is drawn to the fact that the copyright of this thesis rests with its author.

This copy of the thesis has been supplied on condition that anyone who consults it is understood to recognise that its copyright rests with its author and that no quotation from the thesis and no information derived from it may be published without the author's prior written consent.

D42689/82.

KRENAN GA

1P

192

401

LOW-ENERGY ELECTRON IMPACT SPECTROSCOPY

George Adams Keenan

Thesis submitted for the Degree of
Doctor of Philosophy

University of Stirling

September, 1981

Chemistry

Coreduation - February 1982

"They say that good intentions
pave the road to hell
if a thing is not worth doing
its not worth doing well."

R. D. Laing

I would like to dedicate this thesis to my parents and to Judith.

ABSTRACT

An electron scattering spectrometer has been constructed to explore electron impact excitation cross-sections close to threshold.

A trochoidal electron monochromator produces a low energy dispersion electron beam which interacts with target gas in a collision chamber. Inelastically scattered electrons are detected by the trapped electron technique. The design and performance of this instrument are discussed in detail.

A technique to measure total (angle integrated) inelastic cross-sections at fixed incident energy is demonstrated. We know of no other experiment in which this is achieved directly. Spectra from this technique yield

(1) the behaviour of the total electron impact ionisation cross-section for helium up to about 6 eV above threshold, and

(2) the form of $P_E(E_R)$, the energy distribution function of the post ionisation electrons.

Our helium excitation functions are placed on an absolute basis by comparison with known ionisation cross-sections.

The experimental results obtained for the excitation of He, N_2, CO_2, COS and CS_2 are presented and discussed.

CONTENTS

	Page
CHAPTER 1: Introduction	1
CHAPTER 2: Low Energy Electron Scattering	12
CHAPTER 3: Theory of Experiment	
3.1 Principle of the Trochoidal Electron Monochromator (T.E.M.)	37
3.2 Principle of the Electron Trap	43
3.3 Principle of the Modulated Trapped Electron Technique	50
3.4 Energy Loss Spectra at Fixed Incident Energies	52
3.5 Enhancement of Resonances in Energy Loss Spectra	53
3.6 Principles of Electron Transmission Spectroscopy	54
CHAPTER 4: Experimental Details	
4.1 The Electron Spectrometer	56
4.2 Monochromator Design	60
4.3 Collision Region Design	61
4.4 Beam Collector Design	61
4.5 Modes of Operation	62
4.6 Vacuum System	65
4.7 Gas Inlet System	68
4.8 Interlock Protection of Apparatus	70
4.9 Automatic Liquid Air Filling System	71
4.10 Magnetic Field	71
4.11 Electrical Equipment	72

(CONTD.)

		Page
CHAPTER 5: Results and Discussion		
5.1	Experimental Results and Discussion	75
	Introduction	
5.2.1	Helium	75
	Results	
5.2.2	Discussion	87
5.3.1	Nitrogen	127
	Results	
5.3.2	Discussion	127
5.4.1	Electron Energy Loss Spectra for CO_2, CS_2 and COS	151
5.4.2	Results	151
5.4.3	Discussion	151
CHAPTER 6: Conclusion		162

Appendix I: Electrical Apparatus

Appendix II: Construction Materials

Appendix III: Computer Program (Electron Trap)

Appendix IV: T.E.M. (Mk.II)

References

LIST OF TABLES

		Page
1.	Semantics of Resonances	5
2.	Electron Affinities	15
3.	Review of Trapped Electron Studies	23
4.	Review of Modified Trapped Electron Techniques	34
5.	Electronic Energy Levels of Helium	76
6.	Position of Structure in Helium Excitation Functions	88
7.	Magnitude of Helium 2^3S Cross-Section	116
8.	Computer Analysis of Electron Trap Operation	118
9.	Energies of Peaks in the Trapped Electron Spectra of Nitrogen	128
10.	Position of Structure in the $\tilde{E}^3\Sigma_g^+$ ($v' = C$) Excitation Function of Nitrogen	149
11.	Electronic Excitation of CO_2	156
12.	Electronic Excitation of CS_2	158
13.	Electronic Excitation of COS	161

LIST OF FIGURES

		Page
1.	Schematic Diagram of T.E.M.	38
2.	Schematic Diagram of Electron Trap	44
3.	Shape of Trapped Electron Peak	47
4.	Operation of Modulated (a.c.) Trap	51
5.	Schematic Diagram of Electrode Assembly	57
6.	Schematic Diagram of Electron Scattering Spectrometer	59
7.	Modes of Operation of Electron Trap	64
8.	Experimental System	66
9.	Vacuum System	67
10.	Gas Inlet System	69
11.	Electrical Biasing of Spectrometer	73
12a.	Energy Loss Spectrum of Helium (d.c. trap)	77
12b.	" " " "	78
12c.	" " " "	79
13a.	Energy Loss Spectrum of Helium (a.c. trap)	80
13b.	" " " "	81
13c.	" " " "	82
13d.	" " " "	83
14.	Electron Impact Excitation Functions of Helium	84
15.	Estimation of W from 2^3S Onset	86
16a.	Energy Loss Spectrum of Helium (composite $\Delta E_{in} + \Delta W$)	89
16b.	" " " "	90
16c.	" " " "	91
16d.	" " " "	92
16e.	" " " "	93

		Page
17a.	Fixed Incident Energy Spectra of Helium	94
17b.	" " " " "	95
17c.	" " " " "	96
17d.	" " " " "	97
17e.	" " " " "	98
18.	Electron Transmission Spectrum of Helium	99
19.	Threshold Energy Loss Spectrum of Helium (a.c. trap)	101
20.	FWHM of Apparatus Function	104
21.	Electron Impact Excitation Functions of Helium. Cross Sections Derived from Energy Loss Spectra	105
22.	Schematic Representation of Residual Electron Energy Strata within the Electron Trap	106
23.	Comparison of Computed and Experimental Curves at Low Residual Electron Energies in Fixed E_{in} Spectra	109
24a.	Signal Above I.P. from Fixed E_{in} Spectra	110
24b.	" " " " " " "	111
25.	Plot of h vs. $\sigma_{tot}^{ion}/(E_{in}-IP)$	113
26.	Ionisation Cross Section of Helium	115
27.	Plot of Electron Current vs. W for Various V_a in Helium	119
28.	2^3S Excitation Function of Helium	121
29.	2^1S " " "	122
30.	2^3P and 2^1P " "	123
31.	3^3S and 4^3S " "	124
32.	Total Excitation Cross-Section of Helium	125
33.	Metastable Production Cross-Sections of Helium	126
34a.	Energy Loss Spectrum of Nitrogen (d.c. trap)	129
34b.	" " " "	130

		Page
35a.	Energy Loss Spectrum of Nitrogen (a.c. trap)	131
35b.	" " " "	132
35c.	" " " "	133
35d.	" " " "	134
35e.	" " " "	135
36a.	Electron Impact Excitation Function of Nitrogen	136
36b.	" " " "	137
36c.	" " " "	138
36d.	" " " "	139
37a.	Fixed E_{in} Spectrum of N_2	140
37b.	" " " "	141
38.	2^3S Excitation Function of Helium in the Presence of Nitrogen	144
39.	Some Energy Levels of Nitrogen	145
40.	Energy Loss Spectra of Nitrogen ($^2\pi_g$ res.)	147
41.	Energy Loss Spectra of CO_2	152
42.	" " " CS_2	153
43.	" " " COS	154

CHAPTER 1

INTRODUCTION

CHAPTER 1

INTRODUCTION

Electronically excited atoms and molecules play a fundamental role in processes encountered in laser[1] and plasma[2] physics, photochemistry[3], aeronomy[5][6] etc. Electron impact provides an important means for populating these excited states[7]. The work described in this thesis concerns the design and construction of a low energy electron impact spectrometer for the study of near threshold electron energy loss processes to yield information on:

(1) direct electron excitation of both optically allowed and optically forbidden energy states,

(2) electron excitation via temporary negative ion states, and

(3) the behaviour of excitation functions (total cross-sections) near threshold.

A basic difference between photon and electron impact excitation lies in the fact that a photon is absorbed in the process whereas an electron is itself scattered and can be subsequently detected[8]. The selection rules which govern excitation by electron impact depend on the electron energy and can differ greatly from those for photon absorption. When the incident electron energy is large compared to the excitation threshold it can be assumed to a first approximation that the interaction between incident electron and bound electrons in the target atom or molecule is Coulombic in nature, the interaction time is short and the incident electrons are practically unperturbed by the target. This is known as the Born approximation[9].

Within this approximation the selection rules are very similar to those for optical excitation and scattering is predominantly in the forward direction. As the incident electron energy is decreased this approximation loses its validity, the incident electron becoming more intimately involved with the target species. Electrons of intermediate energies (30-100 eV) can excite symmetry forbidden transitions and may exhibit complex angular dependencies i.e. the angular distribution of scattered electrons can be complicated. These scattered electron distributions are often less sharply forward peaked than for an optically allowed transition. Low energy electrons allow the study of spin forbidden transitions whose excitation functions appear to maximise within a few electron volts above threshold. A simple model for this[10] proposes that the incident electron exchanges with one of the valence electrons during excitation resulting in a spin-forbidden transition while electron spin angular momentum of the colliding system is conserved. Such strong interactions are expected to lead to large angle scattering and it is observed experimentally that the relative intensities for spin-forbidden transitions with respect to spin-allowed transitions increase with increasing angle[8]. Another feature of electron impact excitation, without parallel in photon absorption studies is that, in general, the ratios of the differential cross-sections for excitation of different vibrational levels of a single progression are roughly constant with scattering angle and incident energy and equal the Franck-Condon factors. If this is not observed it can usually be

inferred that more than one transition is contributing to the signal. A possible exception has recently been cited.[16a]

Since practically all electronic transitions are allowed in low energy electron impact, results complementary to those from photon absorption and high energy electron impact studies can be obtained. The ratio of the probabilities for spin-allowed to spin-forbidden transitions in photon absorption is typically 10^6 whereas for low energy electron impact it is commonly 10^2 and at large scattering angles a spin-forbidden transition may be more intense than the corresponding spin-allowed one. A detection system such as that described in Chapter 4 which efficiently captures low energy post collision electrons at all scattering angles, yields information on the electronic energy levels of atoms and molecules including low-lying spin-forbidden states which might not be directly detected by other means[11][12].

A study of the excitation functions for electronic transitions observed in electron impact studies can give information on whether a transition is spin-allowed or spin-forbidden. The integral cross-section for a spin-forbidden transition generally maximises within about 5 eV above threshold before decreasing relatively rapidly (approximately as E^{-3}) over a range of about 50 eV,[13] whereas a spin-allowed transition maximises within a few tens of eV before falling off more gradually. Most organic molecules possess an even number of electrons and have closed shell singlet ground state configurations, S_o. The lowest excited electronic state of such a molecule is usually a triplet, T_1. The relatively long

radiative lifetime of a typical triplet state (10^{-4} - 10 secs.), and the presence of two unpaired electrons make it a chemically reactive species, and its chemistry may be quite different from that of the corresponding ground state molecule. The direct investigation of these states by electron scattering is therefore of great importance in photochemistry.

Besides causing direct electronic excitation an electron can also excite an atom or molecule via a compound state or "resonance" formed when the incident electron possesses just the right amount of energy to be accommodated temporarily in an orbital of the target species[14]-[17]. The target which traps the electron may be in its ground state or an excited state with the temporary negative ion state lying, in energy, above or below the so-called parent state. Normally a gas phase negative ion must survive for microseconds if it is to be detected. Such ions are usually formed by the attachment of an electron to a ground state atom or molecule having a positive electron affinity. However these aforementioned resonances have lifetimes of the order 10^{-10} - 10^{-15} secs and so are detectable only indirectly. A useful classification of resonances has been compiled by Schulz[14][15] (see Table 1).

A shape resonance is so called because the incident electron is trapped as a result of the shape of the effective interaction potential which comprises attractive and repulsive (centrifugal) forces. The simplest example of this is electron scattering from the spherically symmetric potential field of an atom where the incident beam can be represented by a plane wave. The angular momentum, J, of any wave about the scattering center is quantised and given by $J = \hbar[\ell(\ell + 1)]^{\frac{1}{2}}$ where $\ell = 0,1,2$ etc.

TABLE 1 - Semantics of resonances (from Schulz, ref. 15).

First name	Last name	Parent	Energy vis-a-vis parent	Some characteristics	Examples
Single-particle Shape (1 particle, 0 holes)	...	Ground electronic state	above (0-4 eV)	Vibrational excitation; dissociative attachment at low energy	N_2 (2.3 eV) H_2 (2-4 eV)
Core-excited Particle-hole (2 particles, 1 hole)	Feshbach; Type I; closed-channel	Mostly Rydberg excited state	below (∿0.5 eV)	Bands correlated to grandparent; sharp structure; many decay channels	N_2 (11.48 eV) H_2 (Bands "a" - "g")
	Shape; Type II; open-channel	Rydberg or valence excited state	above (0-2 eV)	Dissociative attachment	N_2 (9-11 eV) H_2 (8-12 eV)
Doubly core-excited (3 particles, 2 holes)	Feshbach	Doubly excited Rydberg and valence states	below	Above ionization; 2-electron decay	He (57.16 eV)
	Shape		above		N_2 (22 eV)

The atom may possess a suitable unfilled orbital which will have a particular value of ℓ, the orbital angular momentum quantum number. Since the repulsive potential requires the electron to have angular momentum, p(ℓ = 1), d(ℓ = 2) and f(ℓ = 3) wave resonances are expected but generally not s-wave resonances since these have ℓ = 0 and produce no barrier. In the case of molecules, the scattering potential field is not spherically symmetric, the unoccupied orbitals having charge distributions characteristic of the target molecule. These potential distributions determine the possible angular momentum components of the plane wave which may be captured.[47]

Shape resonances vary in lifetime (10^{-10}-10^{-15} secs.)[18][19] and favour decay to the parent atomic or molecular state. The enhancement of the inelastic cross-section for this state at the resonance energy may be the only indication of the existence of such short lived species. Shape resonances associated with the ground states of molecules are widespread. When these decay into the (parent) ground state, this state may find itself vibrationally excited. The nature of the vibrational excitation depends on the lifetime of the negative ion intermediate. When the negative ion lifetime is short, the energy dependence of the vibrational cross-sections exhibits a broad peak as found for the $^2\Sigma_u^+$ compound state of hydrogen at approximately 3.75 eV.[20] If the lifetime is long the resonance state can vibrate and the energy dependence of the cross-section to a given final vibrational state will exhibit a series of spikes associated with the vibrational levels of the compound state e.g. $^2E_{2u}$ benzene shape resonance at 1.2 eV[21]

and the $^2\pi_g$ compound state of oxygen at 0 - 1 eV[22]. For intermediate lifetimes where only one vibration may occur, the cross-section can still exhibit spikes which are characteristic of the compound state e.g. $^2B_{2g}$ ethylene shape resonance at 1.8 eV[23] and the $^2\pi_g$ N_2 resonance centered around 2.3 eV[24]. The "boomerang" model of Birtwistle and Herzenberg[25] successfully accounts for this structure and also the experimentally observed behaviour of peak positions which depend upon the channel of observation. The peaks shift to higher energies for higher vibrational states. Shape resonances associated with the excited states of atoms and molecules are called core excited shape resonances. In the case of molecules they are associated with either Rydberg or valence excited states lying approximately 0 - 2 eV higher than the parent state.

Feshbach or closed-channel resonances are associated with the excited states of atoms and molecules and lie, in energy, below the parent state. In these, the incident electron becomes bound to an electronically excited state of the target. Most Feshbach resonances are associated with Rydberg states. The positive ion core is the "grand-parent", the neutral molecule with one electron excited to a Rydberg state is the "parent" and the addition of a second electron in a Rydberg state to this system(which exhibits a positive electron affinity) yields the resonance. When Feshbach resonances occur, decay into the parent excited state is energetically forbidden if the excitation takes place near the center of the resonance, hence "closed-channel". Because decay into non-parents involves changes in electron configuration of the atoms, Feshbach resonances are usually relatively long-

lived (10^{-12}-10^{-13} secs.) and exhibit vibrational structure[26]. If excitation does not take place at the center but at the high energy wing of the resonance, decay into the parent state may be possible and is favoured.

In resonance scattering the following processes are possible after the initial formation of the temporary negative ion state (AB^{-*})

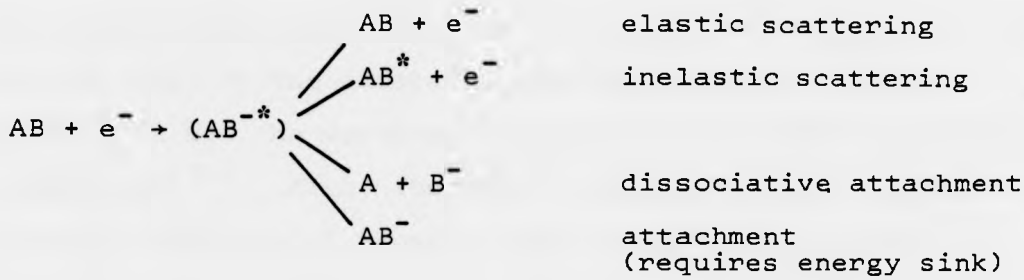

The effects manifest in the decay of these compound states can be studied experimentally, the presence of a resonance being inferred from the behaviour of the various cross-sections with energy in the vicinity of the resonance phenomena. The identification and positioning of resonances are important for several reasons: (1) They provide important routes for the excitation of molecules by electrons. This may facilitate population inversion and laser action[1][27]. (2) Although photoelectron spectroscopy yields much information which can be correlated within the context of Koopman's theorem with the filled orbitals of neutral atoms and molecules, the highest of these being the HOMO (the highest occupied molecular orbital), the complementary data in the gas phase for the lowest unfilled molecules orbitals (LUMO's) is far less comprehensive. When the lowest lying resonance can be detected it is possible to deduce

electron affinities[28]. If the lifetime of the resonance is sufficiently long to exhibit vibrational structure, the electron energy at which the (0,0) transition takes place yields the negative of the adiabatic electron affinity[29]. A survey of low lying resonances is presented in Chapter 2. If the lifetime is too short to permit vibrational structure, the resonance in the scattering cross-sections being examined will appear smooth and broad as a function of energy. In such cases a limit to the adiabatic electron affinity can be established and the vertical (most probable) electron affinity is obtained[30]. Also, the HOMO and the LUMO are the frontier molecular orbitals of Frontier Molecular Orbital Theory[31], a qualitative but very useful theory for rationalising and predicting reactivity, stereoselectivity, regioselectivity etc. in pericyclic and related chemical reactions[32]. In this theory, LUMO energies are often not well known. (3) The low-lying excitation energies for a series of related compounds may be correlated to the quantity (IP-EA), the ionisation potential minus the electron affinity. This has been illustrated by Nenner[33] in a plot of the lowest triplet, T_1, and singlet, S_1, energies versus (IP_{HOMO}-EA_{LUMO}) for a number of mono-substituted benzenes showing that both T_1 and S_1 excitation energies are approximately linear functions of (IP_{HOMO}-EA_{LUMO}). This leads to a prediction of the energies of low-lying states of molecules which are members of homologous series. Another useful correlation employing experimental values for HOMO and LUMO energies is the Coulson-Rushbrooke or "pairing" theorem[34] which can explain many of the unique features of alternant

hydrocarbons. In these molecules, the molecular orbital energy levels are "paired" and the sum (IP + EA) associated with each π,π^* pair should be constant. Usually only the first π,π^* pair (HOMO,LUMO) is considered due to the lack of accurate data for the higher lying negative ion states. Burrow and Jordan[28] have used electron transmission spectroscopy to determine the EA's of several alternant hydrocarbons and have demonstrated that the pairing theorem holds for those anion states which are predominantly associated with the molecule in its ground electronic state. They conclude that it is possible to predict from the appropriate ionisation potentials, the electron affinities associated with anions which cannot be determined directly.

(4) The so-called "harpooning" mechanism[35] accounts for many phenomena observed in reactive scattering in molecular beam studies. For example, in the case of collisions between potassium atoms and bromine molecules in the energy range 0 - 10 eV, the harpooning mechanism postulates an electron jump from K to Br_2 at a separation of about 10 a.u., further evolution of the system being dominated by the Coulomb interaction. This has been described as "the attacking alkali atom tosses out its valence electron, hooks the halogen and hauls it in with the Coulomb force".[36] This approach can lead to a qualitative correlation between the reaction dynamics and the electronic spectra of the reactant molecule since the model depends intimately on the nature of the orbitals available to the harpooning electron. It is essential to know the EA of the acceptor molecule, information which may come from electron transmission studies.

The multicenter nature of the electron/molecule interaction introduces many complex problems for the theoretician who wishes to rationalise experimental observations and develop methods for calculating electronic energy levels, collision cross-sections etc. An exact solution of the full Schrödinger equation for such systems is too complicated and all calculations depend on simplifying approximations[37]. Theories differ in the types of approximation employed and in their mathematical approach to the problem, success often being measured by agreement with experimental results. Since all experimental data contains some error, the refinement of theory and experiment goes hand in hand leading to a continually increasing understanding of the nature of electron/atom and electron/molecule interactions.

CHAPTER 2

LOW ENERGY ELECTRON SCATTERING

CHAPTER 2

LOW ENERGY ELECTRON SCATTERING

Of fundamental importance in any electron impact experiment is a knowledge of the incident electron energy. Since most convenient sources of electrons produce a primary beam having an energy spread of the order of 300 meV or more[38], it is necessary to select electrons within a narrow energy range when high resolution is required. This is often achieved by passing the beam from a thermionic source through electrostatic and/or magnetic fields arranged so as to transmit only electrons of a specific energy[39]. Post-collision electron energy analysers, of similar construction to monochromators, can be used if the energy loss of the scattered electrons is required. The analyser is tuned to transmit only electrons of a chosen energy. In spectrometers employing such devices as monochromator and analyser, electron lenses must be incorporated to ensure that the energy selected beam is parallel over a wide range of energies and that scattered electrons are focussed into the analyser. Also, electron beams of low energy are very sensitive to space charge effects, surface imperfections and various relaxation processes which can all increase the energy distribution. An essentially simple monochromator has been developed by Stamatovic and Schulz[40] which minimises some of these problems. The so-called trochoidal electron monochromator (TEM) operates in an axial magnetic field and is mechanically less complex than most electrostatic devices. It is theoretically capable of high energy resolution and can operate at very low electron energies. A detailed description of its operation is presented in Chapter 3.

The TEM has been used most extensively in the detection of transient molecular negative ions seen as structure in the

derivative with respect to energy of the electron current transmitted through a sample gas. The power of this method of locating resonances was first demonstrated by Sanche and Schulz[41]. A large number of organic molecules have been explored by Burrow et al.[28] and one or two other groups[42][43]. Table 2 surveys molecules whose electron affinities have been determined in electron transmission studies.

If the TEM is to be used as the monochromator in an electron spectrometer, then in the simplest arrangement it must be used with a scattered electron energy analyser which also functions in the presence of an axial magnetic field. The obvious analyser is another TEM and one such spectrometer has been developed[44]. An alternative energy analyser is the "electron trap" developed by Schulz[45]. In it, post collision electrons with nearly zero residual energy are collected on an electrode which is biased so as to form an electrostatic potential well. The incident electron energy is scanned and each time an inelastic threshold is passed, low energy electrons are produced and detected. A series of spectral peaks results corresponding to energy levels of the target molecule, the peak heights representing the probability of electronic excitation at an energy eW above threshold, where W is the magnitude of the trapping potential. It is, in principle, possible by recording a peak height at different W to obtain the shape of the electronic excitation function over a limited range (to approximately 0.5 eV above threshold) although in the simple trap resolution decreases rapidly as W is increased. When operated in a modulated mode[46] (see Chapter 3), resolution is retained relatively far above

threshold (to greater than 10 eV in some cases). Also, the trapped electron technique can differentiate between states excited directly and those excited indirectly, for example *via* temporary negative ion states.

The trochoidal electron monochromator and electron trap were first combined by Dance and Walker who demonstrated its usefulness in a study of threshold energy loss processes in nitrogen and several unsaturated hydrocarbons[11]. As will be demonstrated later in this thesis, this kind of spectrometer must be operated with care; nevertheless, given an understanding of the electron energy selection and trapping processes, it can be employed to give useful information on electron-molecule interactions at energies close to inelastic thresholds. Tables 3 and 4 review electron trap and modulated electron trap data respectively. Some of these polyatomic molecules have also been studied by variable angle electron impact spectroscopy, principally by Kuppermann et al. These have recently been reviewed[13].

A major disadvantage of an electron spectrometer contained in a magnetic field lies in its loss of angular discrimination of the scattered electrons; measurement of the angular distribution of inelastically scattered electrons can help elucidate electronic structure, especially in the detection and assignment of overlapping electronic energy states and resonances[13]. However, the trapped electron technique with its ability to probe interactions close to threshold provides valuable complementary evidence on electron/atom and electron/molecule interactions.

TABLE 2

Vertical Electron Affinities (eV)

Molecule		Electron Affinity	References
Substituted Benzenes			
benzene		-1.15, -4.85	[29], [41], [48]-[51]
toluene	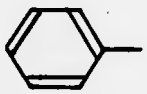	-1.11, -4.88	[48]
ethylbenzene	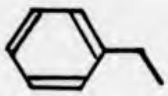	-1.17	[33]
isopropylbenzene	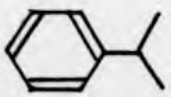	-1.08, -4.69	[33]
tert-butylbenzene	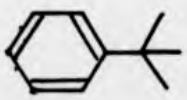	-1.06, -4.67	[33]
cyclopropylbenzene	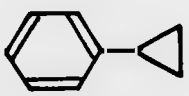	-1.06, -4.59	[28]
phenol	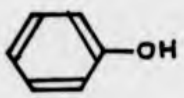	-1.01, -1.73, -4.92	[52]
anisole	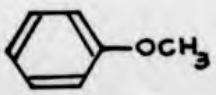	-1.09, -1.72, 4.92	[52]

Molecule		Electron Affinity	References
Substituted Benzenes			
aniline	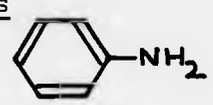	-1.13, -1.85, -5.07	[52]
methylaniline	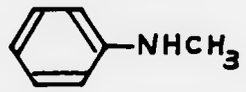	-1.19	[33]
dimethylaniline	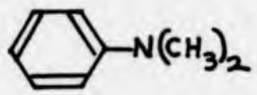	-1.24	[33]
benzaldehyde	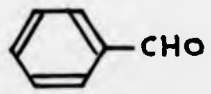	>0, -0.76, -2.21, -4.61	[28]
benzonitrile	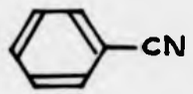	>0, -0.54, -2.49, -3.20, -4.9	[28]
styrene	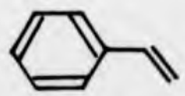	-0.25, -1.05, -2.48, -4.67	[53]
bromobenzene	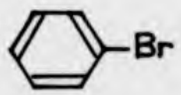	-0.70, -4.42	[52]
chlorobenzene	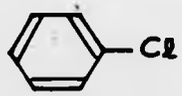	-0.75, -4.50	[52]

Molecule		Electron Affinity	References
Substituted Benzenes			
fluorobenzene		-0.89, -1.40, -4.77	[43] ,[52]
p-difluorobenzene	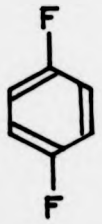	-0.53*, -1.41, -4.51	[43]
1,3,5-trifluorobenzene	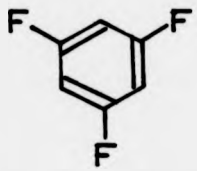	-0.77, -4.48	[43]
1,2,4,5-tetrafluorobenzene	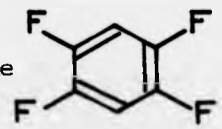	-0.34*, -1.29, -4.51	[43]
pentafluorobenzene	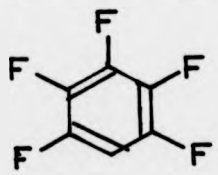	≥-0.15*, -1.19, -4.53	[43]
hexafluorobenzene	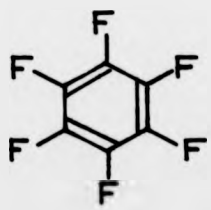	-0.42, -4.50	[43]
o-xylene	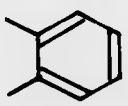	-1.12, -4.9	[48]
m-xylene	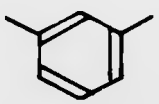	-1.06, -4.81	[48]

Molecule		Electron Affinity	References
Substituted Benzenes			
p-xylene	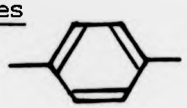	-1.07, -4.89	[48]
1,3,5-trimethylbenzene	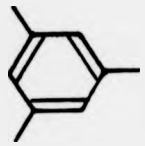	-1.03, -4.78	[48]
1,2,4-trimethylbenzene	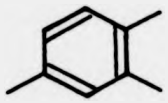	-1.07, -4.83	[48]
cis-stilbene	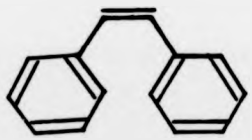	0, -0.92, -1.68, -3.4, -4.67	[28]
naphthalene	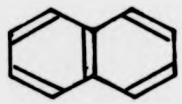	-0.19, -0.90, -1.67, -3.37, -4.72	[28]
Unsaturated Hydrocarbons			
ethylene	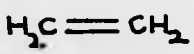	-1.78	[54]
propene	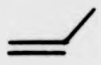	-1.99	[30]

Molecule		Electron Affinity	References
Unsaturated Hydrocarbons			
cis-butene		-2.22	[30]
trans-butene		-2.10	[28]
isobutene	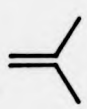	-2.19	[28]
trimethylethylene	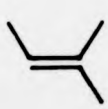	-2.24	[42]
tetramethylethylene		-2.27	[28]
cyclohexene		-2.07	[30]
1,3-cyclohexadiene	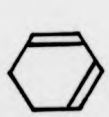	-0.80, -3.43 -0.73	[30] [109]
1,4-cyclohexadiene		-1.75, -2.67	[30]
1,3-cycloheptadiene	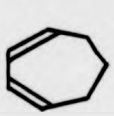	-0.63	[109]

Molecule		Electron Affinity	References
Unsaturated Hydrocarbons			
1,5-cyclooctadiene		-1.83, -2.33	[30]
cyclooctatetraene	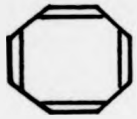	>0, -1.91, -3.60	[28]
norbornadiene		-1.04, -2.56	[30]
1,3-butadiene	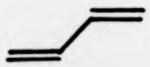	-0.62, -2.8	[54]
trans-hexatriene	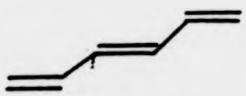	>0, -1.8, -3.54	[28]
acetylene	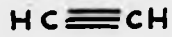	-2.6	[28]
Unsaturated Heterocycles			
pyridine	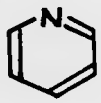	-0.62, -1.20, -4.58	[29]
pyrimidine	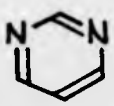	>0, -0.77, -4.24	[29]

Molecule		Electron Affinity	References
Unsaturated Heterocycles			
pyridazine	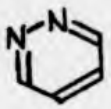	0, -0.73, -4.05	[29]
s-triazine	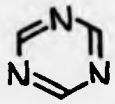	0, -4.0	[29]
pyrrole	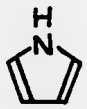	-2.38, -3.44	[55]
furan		-1.76, -3.14	[55]
thiophene		-1.17, -2.67	[55]
Miscellaneous Molecules			
formaldehyde	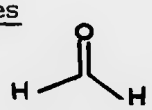	-0.86	[42] ,[56]
acetaldehyde	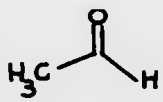	-1.19	[28] ,[42]
acetone	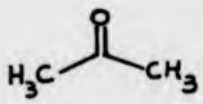	-1.51	[28] ,[42]

Molecule		Electron Affinity	References
Miscellaneous Molecules			
acrolein	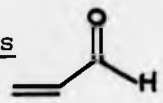	>0, -2.47	[28]
acrylonitrile	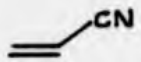	-0.21, -2.74	[28]
acetonitrile	CH_3CN	-2.84	[28]
tetrafluoromethane	CF_4	-0.32	[57]
chlorotrifluoromethane	CF_3Cl	-0.29	[57]

All EA's are vertical except those marked * which correspond to the first (v' = 0) vibrational level.

All EA's are determined by electron transmission spectroscopy.

TABLE 3

Review of Trapped Electron Studies

Atoms	Energy Loss Spectra	Excitation Functions
He	(45),(46),(58),(59),(61), (62),(68),(72),(73),(78), (88),(90),Present work (98),(150)	(46),(61), (72),(73),(81), (90),Present work,(139), (150),(111b)
Ne	(68)	
Ar	(68)	
Hg	(45)	
Diatomic Molecules		
H_2	(45),(59),(90),(94),(97),	(60)
D_2	(59),(90)	(60)
N_2	(11),(58),(61),(64),(66), (81),(87),(88),(89),(90), (94),(96),Present work	(60),(61),(87), (88),(99)
O_2	(63),(97)	
NO	(91)	
CO	(61),(81),(84),(88),(91), (93),(94),(95),(97).	(60),(61),(88),
Triatomic Molecules		
H_2O	(46),(79),(82)	
D_2O	(46)	
CO_2	(12),(61),(88)	(61),(88),(99)
COS	(12)	
CS_2	(12)	
N_2O	(83),(97)	
H_2S	(46)	

		Energy Loss Spectra	Excitation Functions
Saturated Hydrocarbons			
methane	CH_4	(62),(69),(86),(88),(89),(91),(94),(97)	
ethane	C_2H_6	(62),(86),(89),(91	
propane	C_3H_8	(86),(91)	
cyclopropane	C_3H_6	(88),(91)	
neopentane	C_5H_{12}	(91)	
cyclooctane	C_8H_{16}	(88)	
Unsaturated Hydrocarbons			
ethylene	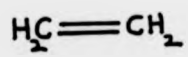	(11),(61),(62),(70),(77),(88),(111c)	(61),(88)
propylene	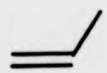	(11),(62)	
cis-butene		(11),(88)	
trans-butene		(11),(88)	

Unsaturated Hydrocarbons		Energy Loss Spectra	Excitation Functions
but-1-ene	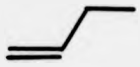	(11)	
butadiene	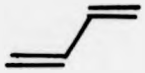	(88)	
tetramethylethylene		(88)	
1,6-heptadiene	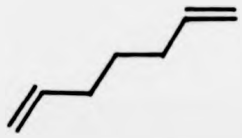	(88)	
1,4-cyclohexadiene		(88)	
isotetraline	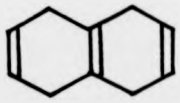	(88)	
1,3,5-transhexatriene	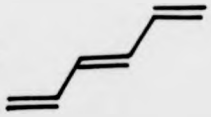	(46)	
1,3,5,7-cyclooctatetra-ene		(46)	
trimethylethylene	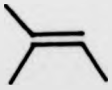	(91)	

Unsaturated Hydrocarbons		Energy Loss Spectra	Excitation Functions
1,2-dimethylcyclohexene	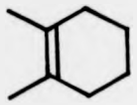	(46)	
norbornadiene		(88)	
hexamethylbicyclo-[2,2,0]hexa-2,5-diene	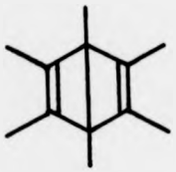	(88)	
allene		(46)	
1,1-diphenylethylene	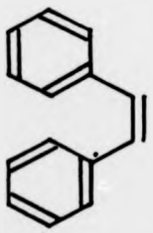	(88)	
azulene	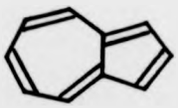	(74),(88)	
naphthalene	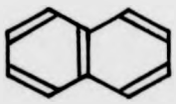	(74),(85),(89)	
1,6-methano[10]-annulene	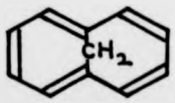	(74)	

Unsaturated Hydrocarbons		Energy Loss Spectra	Excitation Functions
benzene		(46),(61),(88), (91),(92)	(61),(88)
toluene	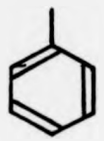	(67),(91),(92)	
acetylene		(46),(62),(71),(80), (111a)	
propyne		(46),(62),(111a)	
but-1-yne		(62),(111a)	
but-2-yne		(111a)	

Heterocyclic Molecules

pyridine	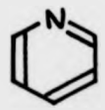	(66),(76),(88)	
pyrazine	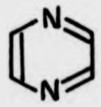	(66),(89)	

Heterocyclic Molecules		Energy Loss Spectra	Excitation Functions
pyrimidine	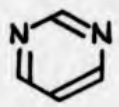	(66),(89)	
pyridazine	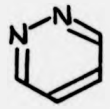	(66),(89)	
s-triazine	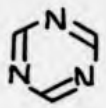	(66)	
1,6-oxido[10]-annulene	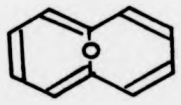	(74)	
thiophene		(55)	
furan		(55)	
pyrrole	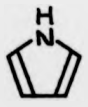	(55)	
quinoline	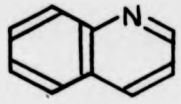	(85),(89)	

Heterocyclic Molecules		Energy Loss Spectra	Excitation Functions
isoquinoline	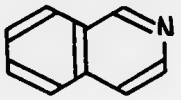	(85),(89)	
quinuclidine	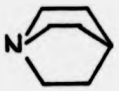	(88)	
Substituted Benzenes			
fluorobenzene	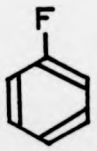	(67),(92)	
p-difluorobenzene		(91)	
hexafluorobenzene	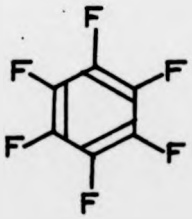	(88)	
toluene	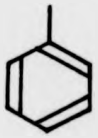	(67),(92)	
o-fluorotoluene	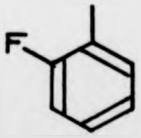	(91)	

Substituted Benzenes		Energy Loss Spectra	Excitation Functions
m-fluorotoluene	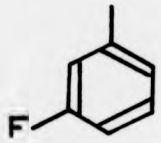	(91)	
p-fluorotoluene		(91)	
benzaldehyde	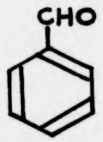	(67),(88),(92)	
benzoic acid	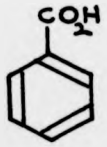	(67),(92)	
nitrobenzene	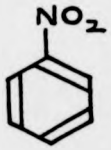	(92)	
acetophenone	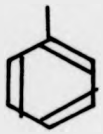	(88)	
phenol		(67),(92)	

Substituted Benzenes		Energy Loss Spectra	Excitation Functions
anisole	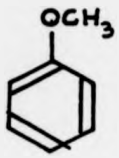	(92)	
aniline	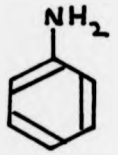	(67),(92)	
N-methylaniline	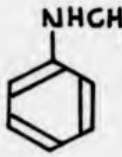	(67),(92)	
thiophenol	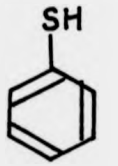	(67),(92)	

Miscellaneous Molecules			
$CFCl_3$		(57)	
CCl_4		(119)	
$CFCl_2$		(57)	
$CHCl_3$		(119)	
CF_3Cl		(57)	
CH_2Cl_2		(119)	
CF_4		(57)	
CH_3Cl		(91),(119)	
methanol	CH_3OH	(46),(79)	
perdeuterated methanol	CD_3OD	(46)	

Miscellaneous Molecules		Energy Loss Spectra	Excitation Functions
methylamine	CH_3NH_2	(91)	
ammonia	NH_3	(65),(88)	
formaldehyde	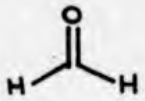	(42)	
acetaldehyde	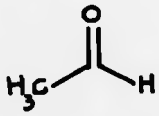	(42)	
acetone	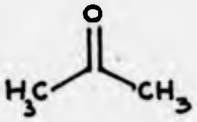	(42),(88)	
triethylamine	$(C_2H_5)_3N$	(88)	
dimethylether	H_3COCH_3	(46)	
glyoxal	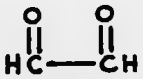	(75)	
biacetyl	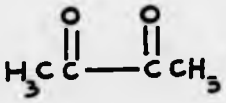	(75)	
7-dehydro-cholesterol	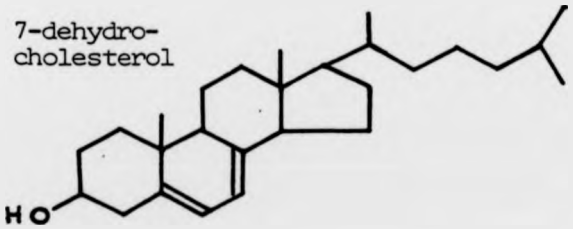	(46)	

Miscellaneous Molecules	Energy Loss Spectra	Excitation Functions
C_2H_3F	(111c)	
$1,1\text{-}C_2H_2F_2$	(111c)	
C_2ClF_3	(111c)	

TABLE 4

Review of Modified Trapped Electron Techniques

Modulated Electron Trap

Atoms	Energy Loss Spectra	Excitation Functions
He	(46),(78),(98),(104), (105),(107),(108), Present work	(78),(108), Present work
Ne	(110a),(110b),(110c)	
Ar	(110b)	(103)
N	(110e)	(110e)
Diatomic Molecules		
N_2	(100),(106), Present work	(99),(103), Present work
O_2	(101),(110d)	
Triatomic Molecules		
H_2O	(79)	
H_2S	(46)	
COS	Present work	
CO_2		(99)

Unsaturated Hydrocarbons		Energy Loss Spectra	Excitation Functions
ethylene		(77),(111c)	(77)
acetylene		(46),(80)	
propyne		(46)	
benzene		(46)	

Heterocyclic Molecules

thiophene		(55)	
furan		(55)	
pyrrole		(55)	

Miscellaneous Molecules

acetone	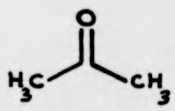	(42)	(42)

Miscellaneous Molecules		Energy Loss Spectra	Excitation Functions
acetaldehyde	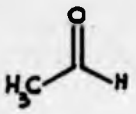	(42)	(42)
formaldehyde	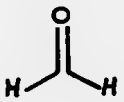	(42)	(42)
glyoxal		(75)	
biacetyl	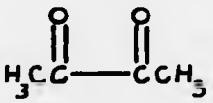	(75)	
methanol	CH_3OH	(46),(79)	
borazine		(46)	
C_2H_3F,1,1-$C_2H_2F_2$,C_2ClF_3		(111c)	
CCl_4,$CHCl_3$,CH_2Cl_2,CH_3Cl		(119)	

Energy Loss Spectra at Fixed Incident Energy in Electron Trap

He	Present work
N_2	Present work

Enhancement of Negative Ion Features in Electron Trap

He	(102)
Ne	(102)

CHAPTER 3

THEORY OF EXPERIMENT

CHAPTER 3

3.1 PRINCIPLE OF THE TROCHOIDAL ELECTRON MONOCHROMATOR (TEM)

A schematic diagram of the TEM as developed by Stamatovic and Schulz [112] is shown in Fig.1.

The theoretical treatment of the behaviour of charged particles in such a field configuration is well documented [113,114,115]. The equation of motion for an electron with initial velocity $\underline{v}_o$ moving in crossed magnetic and electric fields is

$$\frac{d\underline{v}_o}{dt} = -\frac{e}{m}\left[\underline{E} + (\underline{v}_o \times \underline{B})\right]. \qquad (1)$$

There is no component of force acting in the direction of the magnetic field, i.e. in the direction of the incident electron beam; therefore the velocities of the electrons in the z direction are constant (See Fig.1 for definition of the axes). This allows the introduction of a set of moving coordinates which move in the x direction with velocity

$$\underline{v}_x = (\underline{E} \times \underline{B})/B^2 \qquad (2)$$

and since $\underline{E}$ is perpendicular to $\underline{B}$

$$\underline{v}_x = E/B$$

By introducing a moving set of coordinates with velocity $\underline{v}_x$, the electric field is eliminated from the equation of electron motion. The velocity in the moving coordinate system is related to the velocity in the stationary system by

$$\underline{v}_o(x,y) = \underline{v}_x + \underline{v}(x',y') \qquad (3)$$

thus $$\frac{d\underline{v}_o(x,y)}{dt} = \frac{d\underline{v}(x',y')}{dt} \qquad (4)$$

where $\underline{v}_o(x,y)$ is a component of incident velocity in the xy

FIG. 1

Schematic Diagram of T. E. M.

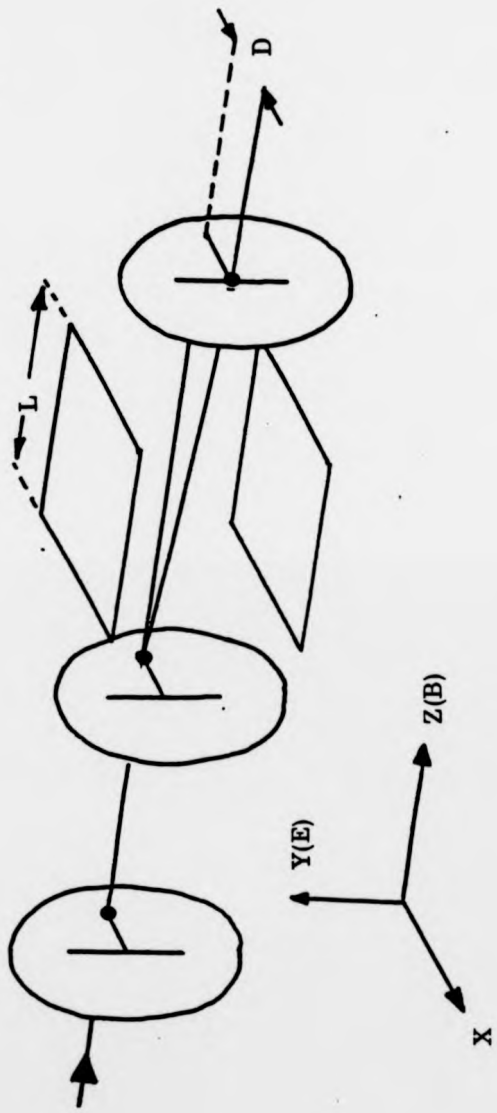

plane and $\underline{v}(x',y')$ is the corresponding component of incident electron velocity in the moving set of coordinates. Substituting (2), (3), (4) into (1) gives

$$\frac{d\underline{v}(x',y')}{dt} = -\frac{e}{m}\left[\underline{v}(x',y') \times \underline{B}\right] \qquad (5)$$

Since the electron motion is in the xy plane which is at right angles to the magnetic field and since no electric field is experienced, the force on the electron is always in a direction at right angles to both the component of the velocity vector in the xy plane and the magnetic field vector. Equation (5) represents a circular motion with radius ρ and angular velocity δ.

$$\delta = eB/m$$

$$\rho = mv(x',y')/eB.$$

This circular motion combined with the motion of the coordinate system causes the electrons to trace out trochoidal trajectories. With the magnitude of the fields encountered in the TEM, the radius of the trochoid is small and it is the net deflection due to the drift velocity $\underline{v}_x$ in passing through the cross-field region which leads to energy dispersion. That is, electrons enter and exit the TEM in the direction of the magnetic field but are displaced by an amount which depends on the number of trochoids completed while traversing the cross-field region which in turn depends on their axial velocity, so dispersion occurs as a result of the time of flight of the electrons. This displacement from the axis, D, is given by

$$D = \underline{v}_x t \qquad (6)$$

where t is the time spent by the electrons in the cross-field region.

$$t = L/\underline{v}_{oz} = L(2\omega/m)^{-\frac{1}{2}} \qquad (7)$$

$\underline{v}_{oz}$ is the initial velocity in the z direction

$\omega = \frac{1}{2} m\underline{v}_{oz}^2$ and L is the length of the cross-field region.

Combining (6) and (7)

$$D = \underline{v}_x L/\underline{v}_{oz} = \underline{v}_x L(2\omega/m)^{-\frac{1}{2}} \qquad (8)$$

this yields the energy spread

$$\frac{\Delta\omega}{\omega} = \frac{2\Delta D}{D}$$

where ΔD is the sum of the entrance and exit apertures ($\Delta D = S_1 + S_2$).

The optimum energy spread is obtained for low ω; therefore the TEM should be operated at very low electron energies. An important additional energy spread results from the transverse electric field. The maximum potential drop across the electron beam is ES_1. This causes a velocity spread in the analyser adding to the energy distribution. The expression for the full width at the base of the energy distribution at the exit from the TEM as derived by Roy [116] includes a factor for the effect of angular divergence of the beam in entering the cross-field region. It has already been stated that the relative energy dispersion $\Delta\omega/\omega$ is $2\Delta D/D$ to a first approximation [40]. However, to take into account the angular divergence of the incident beam, $\underline{v}_{oz}$ must be replaced by $\underline{v}_o \cos\gamma$ thus

$$\frac{\Delta\omega}{\omega} = \gamma^2 + \frac{2\Delta D}{D} . \qquad (9)$$

Since for a given geometry, the selected electron has an energy given by

$$\omega = \left[\frac{EL}{BD}\right]^2 m/2 \qquad (10)$$

combining (9) and (10) yields

$$\Delta\omega = \frac{m}{} \left[\frac{EL}{BD}\right]^2 \left[\gamma^2 + \frac{2\Delta D}{D}\right] + eES_1 \qquad (11)$$

where

$\Delta\omega$	= full width at base	eV
m	= electron mass	kg
e	= electron charge	c
E	= electric field strength	Vm^{-1}
L	= length of cross-field region	m
B	= magnetic flux density	weber m^{-2}
D	= displacement from axis of incidence	m
γ	= angular divergence	radians
ΔD	= $S_1 + S_2$	
S_1	= entrance aperture	m
S_2	= exit aperture	m

Angular divergence is a difficult factor to assess experimentally. However, this is not important in the present system, as $\Delta D/D = 0.47$

and $\gamma^2 = 0.01 \quad (\gamma = 5^o)$

$0.03 \quad (\gamma = 10^o)$

$0.07 \quad (\gamma = 15^o)$

A more realistic expression for the energy spread would be

$$\Delta\omega = m\left[\frac{EL}{BD}\right]^2 \left[\gamma^2 + \frac{\Delta D}{D}\right] + eES_1 + \sum_i n_i \qquad (12)$$

where the additional components, n_i, are unavoidable in the realistic operation of the instrument and are due to relatively unpredictable effects such as space charge (at

high current intensities and/or low electron energies), field penetration and fringe fields at the entrance and exit to the TEM, field inhomogeneities due to surface and contact potentials and secondary emission from surfaces. The full width at half maximum, which is the quantity usually referred to in practice, is approximately two to three times less than the above $\Delta\omega$ [40,117,118]. FWHM values of 20-40 meV have been reported [119,112].

McMillan and Moore [120] have recently carried out a study of the operation of the trochoidal electron monochromator; whereas previous analyses dealt with the electron energy spread due to the voltage drop (ES_1) across the entrance aperture as a separate additive factor, these authors assess its operation by deriving electron trajectory equations which include this voltage drop. They predict a beam shear which is a function of the field magnitudes and the mechanical dimensions of the device and suggest that the exit aperture should be eliptical with major axes lying at an angle to the plane of symmetry of the deflector plates, i.e. the exit aperture is matched to the sheared beam for optimum performance. This introduces practical problems in the construction and positioning of the exit slit. A calculated figure of merit for this system given by the ratio of the maximum of the transmission function to the FWHM energy spread shows that an ideally positioned slit is significantly better than a circular exit aperture. However, as mentioned, there may be practical problems in constructing such a system and fully realising this advantage.

3.2 PRINCIPLE OF THE ELECTRON TRAP

A monoenergetic electron beam is directed parallel to an applied magnetic field into the collision chamber containing target gas. Electrons which lose almost all of their energy in an inelastic collision, as is the case when the incident electron energy is just above the threshold for some inelastic excitation process, are trapped by an electrostatic potential well created along the axis of the interaction region. This is a highly sensitive method for the study of inelastic processes, since low energy electrons are efficiently collected over all angles.

Fig.2 presents a schematic diagram of the operation of the electron trap. The monoenergetic electron beam from the trochoidal electron monochromator is accelerated into the collision region by the applied potential V_a. The central section of this region is biased slightly positive forming a potential well of depth W. The energy of the incident electron is $e(V_a + W)$ and if an amount of energy greater than eV_a is lost in an inelastic collision, the electron will become trapped inside the well, having insufficient energy to surmount the barrier at the exit. It will then spiral back and forth following the magnetic field lines during which time it will undergo many elastic collisions with gas molecules resulting in the reorientation of its velocity vector and subsequent diffusion to the cylindrical collector. The time τ for a slow electron to reach the collector is approximated by [45]

$$\tau = 0.26 \frac{eB^2R^2}{mVv_c} \qquad (13)$$

FIG. 2

Schematic Diagram of Electron Trap

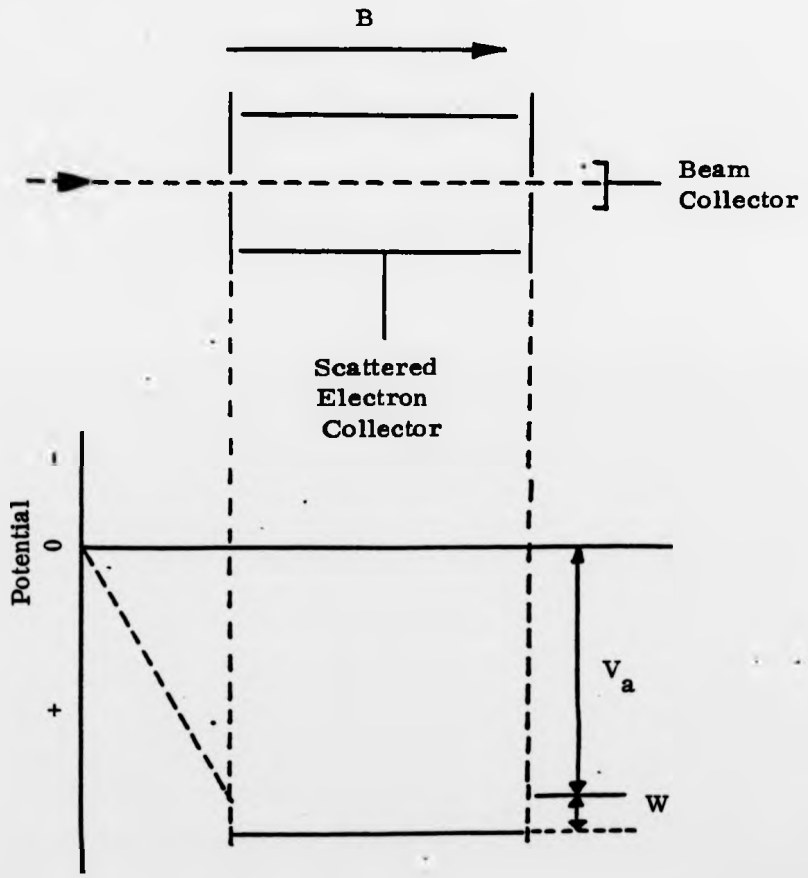

B = magnetic flux density (Wb m^{-2})

m = electron mass (Kg)

e = electron charge (c)

R = radius of collector (m)

V = energy of electron (V)

ν_c = collision frequency.

Typically, τ will be 10^{-2} - 10^{-3}s.

To illustrate the operating principles of the electron trap consider the two variables, accelerating voltage V_a and well depth W.

Variation of V_a

In the case of a transition whose threshold potential is V_{ex} and, for simplicity, whose excitation function is linear over an energy range of at least eW, as V_a is progressively increased, well depth W being constant, electrons will begin to be collected at the trapped electron collector when the incident electron energy equals the threshold energy (eV_{ex}) of a transition, i.e.

$$e(V_a + W) = eV_{ex}$$

$$\text{or} \quad eV_a = e(V_{ex} - W)$$

The trapped electron current appears at a value of V_a which equals V_{ex} - W. As V_a is increased more and more electrons will be trapped yielding the shape of the excitation function until $e(V_a + W) - eV_{ex} > eW$ at which point the inelastically scattered electrons will have sufficient energy to surmount the potential barrier at the end of the well and escape. At

this point $V_a = V_{ex}$ and the collected current will fall to zero. Fig. 3 illustrates this and also shows a computed trapped electron peak shape as a function of electron energy for an incident electron beam having a Gaussian energy distribution with a half-width of $\frac{1}{2}\epsilon$. Each time the threshold of a transition is passed a peak will occur (provided the transitions are separated by an energy of at least W eV). Only when the energy spread in the electron beam is zero will the peak maximum in a threshold excitation function coincide exactly with V_{ex}. The threshold energy generally lies between $e(V_{ex} - W)$ and eV_{ex}. As neither the beam energy distribution nor the exact shape and depth of the potential well are known, it is convenient to equate the maxima in a spectrum to the energies of the excitation processes. Since, to a first approximation, the difference between the true and the measured maxima varies little with V_a, this procedure is acceptable. Excitation may also occur via temporary negative ion states and in this case the behaviour of the trapped electron current with respect to the variation of well depth is different. An excitation function for such a resonance process might be delta shaped. If the value of W is less than the difference between the onset energy eV_{ex} and the maximum of the resonance excitation function eV_{max}, the trapped electron current maximum will lie at $V_a = V_{ex}$ as before. When W exceeds $V_{max} - V_{ex}$ in magnitude the peak in the trapped electron spectrum appears at an energy eV_{max} i.e.

$$\text{for } e(V_a + W) = eV_{max}$$

$$eV_a = e(V_{max} - W).$$

FIG. 3

Shape of Trapped Electron Peak

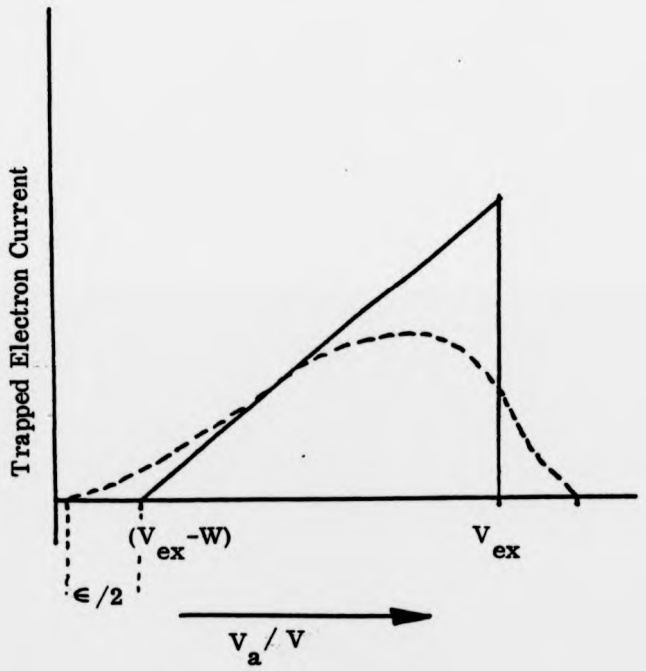

So the peak position shifts to lower values of V_a as W is increased. This provides a simple method for differentiating between direct excitation processes and those which proceed via narrow energy width resonances.

Ideally the peak height observed for a directly excited transition is proportional to the excitation cross-section at an energy eW above threshold; however as shown in Fig.3 this may not be the case for low values of W and for a practical electron beam having a finite energy spread. If the electron energy distribution in the beam is known, a correction factor can be calculated. Since the experimentally measured electron energy distribution is not usually a convenient analytical function another method is employed in the present work where such corrections are necessary. This utilises the fact that the area under the broadened trapped electron curve is equal to the area under the idealised curve for monoenergetic electrons, hence the cross-section is proportional to the area of the measured peak. However, under certain experimental conditions (low electron energy and/or deep well depth) it is possible for electrons to be elastically scattered into a solid angle such that the axial component of electron velocity is insufficient for escape through the electrostatic potential barrier at the end of the collision chamber. The measured inelastic cross-section will be larger than the true value since these elastically scattered electrons effectively add to the incident electron beam. In order for an electron in the primary beam to be trapped it must scatter elastically through an angle greater than some critical angle θ_c measured with respect to the axis of the collision chamber

$$\cos \theta_c < \left[\frac{W}{E}\right]^{\frac{1}{2}}$$

where $E = V_a + W$.

It is also possible for this mechanism to trap inelastically scattered electrons whose final energy E_r is greater than the trapping energy eW. This is normally unimportant where inelastic cross-sections are low compared to the elastic cross-sections. So, the peak magnitudes observed for given transitions are proportional, after certain allowances are made for elastic scattering, to the excitation cross-sections at an energy eW above threshold. By measuring these peak magnitudes at different well depths, the shapes of excitation functions near threshold can be plotted out. The range of well depths available in this technique is relatively limited (0 - 0.5V) as resolution decreases rapidly as W increases. This rapid decrease in resolution is due to two major factors:

(1) At a well depth W, excitation processes must be separated, in energy, by at least an amount eW if they are to be distinct from each other. As W increases this will not be the case.

(2) In the electron trap, a contributing factor to energy spread and loss of resolution is the shape of the electrostatic potential well of the collision region. Fringe fields at the entrance and exit of the well accelerate and decelerate electrons and since collection takes place over the entire scattering length, the collected signal is integrated over the energy range as defined by these fringe fields resulting in poorer resolution than expected from the trochoidal electron monochromator. This effect increases as W increases.

Another factor which must be considered in the trapped electron technique is the presence of ions in the collision chamber. The effect of positive ions is obvious resulting in a characteristic sharp fall off in signal above the ionisation potential. Negative ions are indistinguishable from electrons and may lead to confusion in interpreting energy loss spectra.

In conclusion, the restriction of the trapped electron technique to low well depths (near threshold) and the contributions to the signal by ions has suggested the following, relatively simple modification.

3.3 PRINCIPLE OF THE MODULATED TRAPPED ELECTRON TECHNIQUE

This technique differs from the original electron trap in that the potential barrier at the exit from the collision region is periodically lowered then raised, the in-phase signal being detected using a lock-in amplifier. Only electrons which retain an amount of energy between eW and $e(W - \Delta W)$ will contribute to the signal where ΔW is the amplitude of the modulated potential applied to the exit barrier at potential V_a. Ions can no longer contribute to the signal which is due only to the effects of the small modulation voltage on the trapped electron current. Perhaps the most important additional feature of the modulated electron trap is its ability to operate at relatively deep well depths without a prohibitive loss of resolution. To illustrate this consider Fig.4. Only electrons having a well-defined energy $e(W - \Delta W) \leq E \leq eW$ will be recorded, i.e. electrons having lost an amount of energy between $e(V_{ex}^{A} - \Delta W)$ and eV_{ex}^{A}. These come exclusively from process A.

FIG. 4

Operation of Modulated (a.c.) Trap

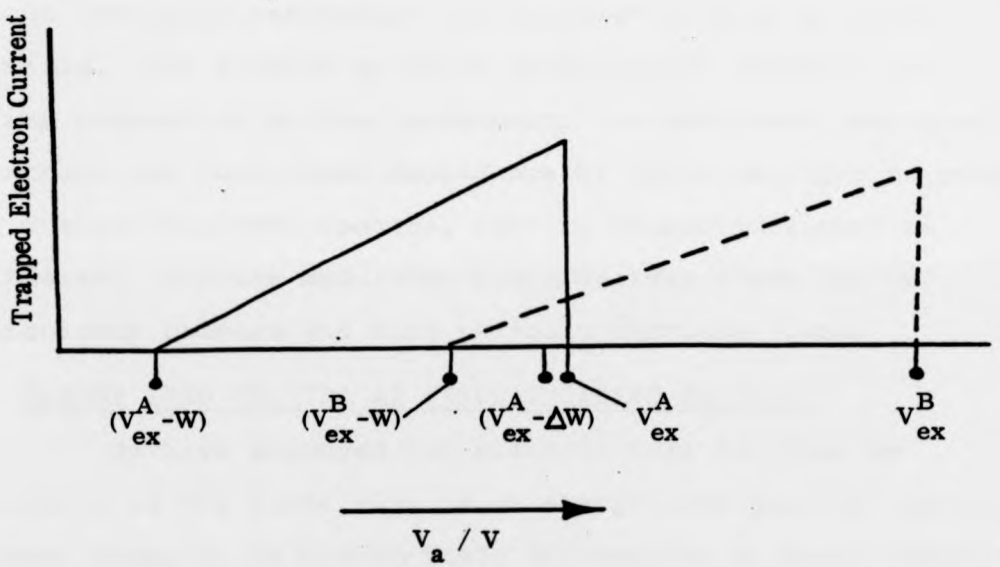

FIG. 4

Operation of Modulated (a.c.) Trap

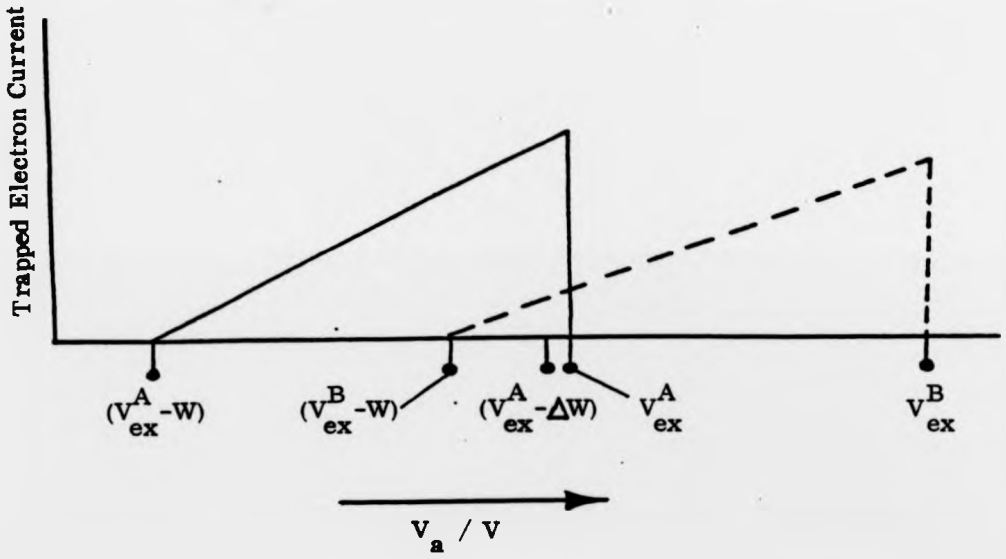

At this energy inelastic post-collision electrons from process B have an amount of energy lower than that required for detection and so are not registered, as they would be in the simple trap. As V_a is increased electrons from process A have residual energy greater than eW and so escape. However, eventually electrons which have excited process B will be collected with energies in the range eW to e(W - ΔW). A series of peaks will result whose magnitudes will be, in principle, proportional to the various inelastic excitation functions at a value eW above threshold. The breadth of these peaks yields directly the working resolution of the instrument. As mentioned previously, to extract the functional dependence of cross-sections on energy from trapped electron spectra, certain corrections must be considered. For the modulated electron trap these can be particularly complex and will be fully discussed later.

3.4 ENERGY LOSS SPECTRA AT FIXED INCIDENT ENERGIES

We have employed the electron trap for what we believe to be the first time in an energy loss mode at constant incident energy E_{in} to directly yield information on total (angle integrated) inelastic cross-sections including electron impact ionisation. As will be described in Chapter 4, this is achieved by maintaining the incident electron energy at a constant value while scanning the exit barrier W in a modulated mode as in the modulated electron trap. The energy axis of the spectrum may be considered either as variation of W (i.e. $E_{in} - eV_a$) or variation of V_a (i.e. $E_{in} - eW$), that is, either as an analysis of residual energy or as energy loss.

3.5 ENHANCEMENT OF RESONANCES IN ENERGY LOSS SPECTRA

This mode of operation differs in only one respect from the modulated electron trap described previously, the incident electron energy being modulated along with the potential barrier at the exit from the collision region. There are two independent sources of in-phase signal in such an experiment:

(1) signal due to modulation of the potential well resulting in energy loss spectra as shown in Fig.13.

(2) signal due to modulation of the incident electron energy.

Since temporary negative ion states can occur only at specific incident electron energies, it follows that electrons which lose energy in an inelastic process which occurs via such a state can be produced only when the incident electron energy equals the resonance energy. If these inelastically scattered electrons have energy less than eW they will be trapped in the collision region, eventually migrating to the scattered collector.

In this way sharp changes in the in-phase signal detected by a lock-in amplifier occur as the incident electron energy is scanned through the resonance energy. The derivative of the signal is recorded leading to enhancement of structure c.f. transmission spectroscopy. The composite spectrum consists of features which are independent of well depth (directly excited) and those which occur via temporary negative ion states. As the well depth is increased these two types of feature can be separated (see Fig.16).

3.6 PRINCIPLES OF ELECTRON TRANSMISSION SPECTROSCOPY [119]

In this technique the intensity of a beam of mono-energetic electrons is monitored after attenuation occurs in passing through a gas cell.

The transmitted current I is related to the incident current I_o by the equation

$$I(E) = I_o \exp(- nQ(E)L) \qquad (14)$$

n = gas density

Q = total scattering cross-section

L = scattering path length.

If there is any structure in Q(E) with respect to energy it will be reflected in the variation of the transmitted current I(E) as a function of energy. Structure in the inelastic cross-section is often indicative of the formation of negative ion resonances. When $nQ_tL > 1$ some amplification of the structure takes place. The percentage change in the transmitted current is larger than the percentage change in the cross-section. A further improvement in sensitivity is possible [120] by measuring the derivative with respect to electron energy of the transmitted current.

$$\frac{dI}{dE} = -(nL)(I_o \exp(-nQ(E)L)(dQ/dE) \qquad (15)$$

$$= -(nL)(I(E))dQ/dE \qquad (16)$$

The derivative of the transmitted current is then directly related to the derivative of the total scattering cross-section with respect to energy. Electron transmission spectroscopy is a highly sensitive method for the detection of resonances and has been used to position and to give information on the life-times of negative ion states in many polyatomic molecules.

However, angular scattering data is not accessible in this experiment, neither does it, by itself, allow the identification of the state to which the resonance decays.

CHAPTER 4

EXPERIMENTAL DETAILS

CHAPTER 4

4.1 THE ELECTRON SPECTROMETER

Our spectrometer has been designed to be flexible and capable of performing a number of different types of electron scattering experiment. Schematic diagrams of the electrode assembly are shown in Figs.5 and 6 along with electrode dimensions. All electrodes are machined from ARCAP AP4, a non-magnetic copper-nickel alloy with a reputation for possessing stable, uniform surface properties. The electrode system comprises three independently assembled units -

(i) Trochoidal electron monochromator and filament

(ii) Collision region

(iii) Retarding electrodes and beam collector.

Mechanical alignment is achieved in three ways -

(1) electrodes and deflector plates are spaced and positioned by sapphire balls placed in accurately oriented holes

(2) sections 1), 2) and 3) are positioned with respect to each other by accurately machined flanges and spigots

(3) the scattered electron collector is positioned with respect to the axis of the system by quartz support discs referred to the inner surface of the gas cell.

Overall alignment of the system is quickly and easily checked by a low power He/Ne laser.

In operation, electrons are emitted from a thoriated tungsten filament and directed through electrodes E_1-E_5 along a line displaced off axis by 3 mm into the space between two parallel plates D_1 and D_2, separated by 3.6 mm. The midpoint of these plates is biased to slow electrons down so that their mean energy is less than 50 meV. Additionally, the plates are

FIG. 5

Schematic Diagram of Electrode Assembly

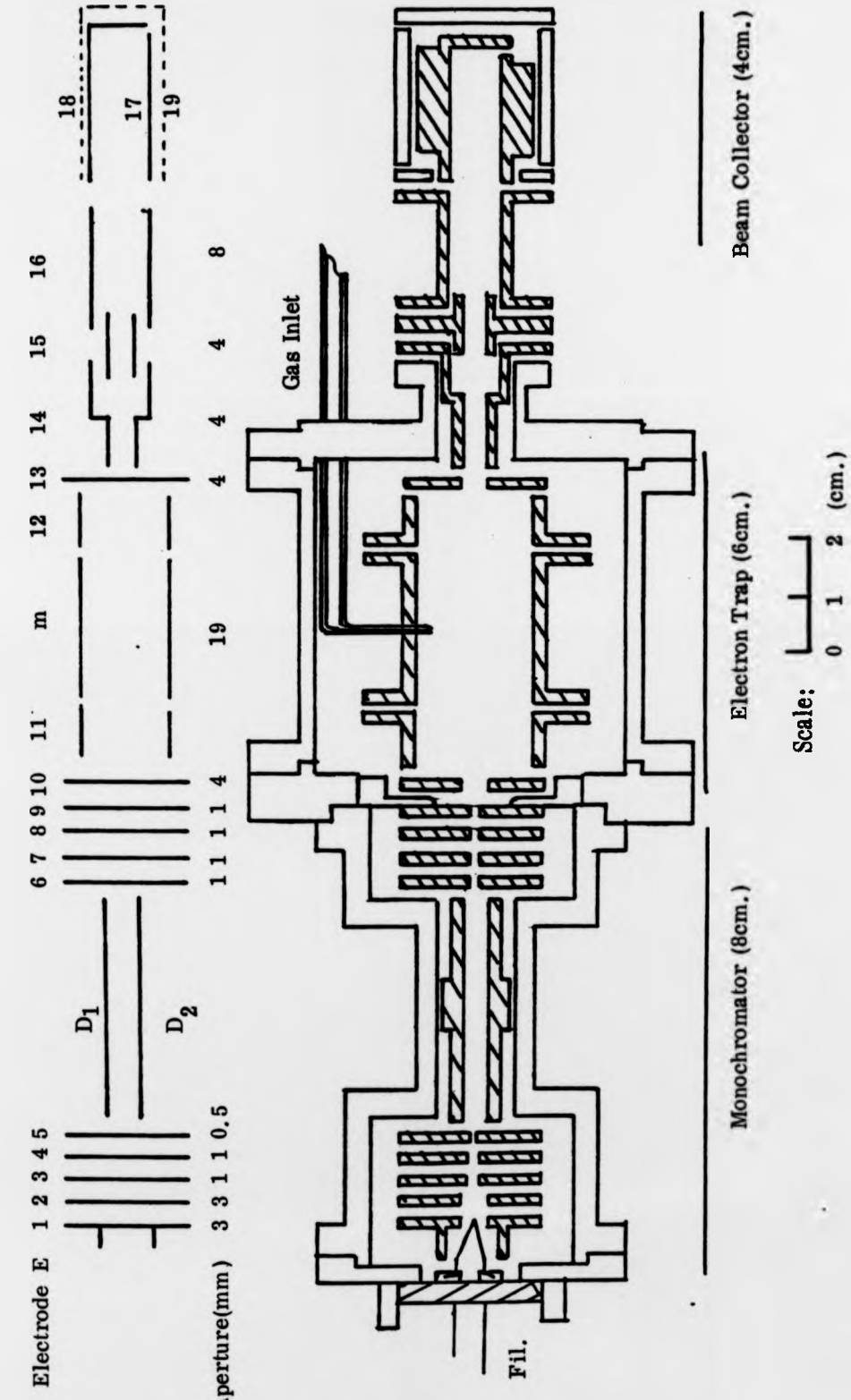

biased so that there is an electric potential between them of approximately 600 mV. In this region the action of a perpendicular electric field (167 Vm^{-1} for the above value of deflector potential) in conjunction with the axial magnetic field (approx. 10^{-2} Wb m^{-2}) present in the experiment causes the electrons to drift in a direction which is mutually perpendicular to the applied fields. Electrons exiting the crossed-field region through the axial aperture of E_6 have been dispersed by approximately the same distance and have a narrow well-defined energy spread. This monoenergetic electron beam is then accelerated into the inner collision region by the application of a potential gradient between electrodes E_8 and E_9-E_{19}. This potential V_a along with the potential W applied to electrode E_m defines the incident energy of the electrons and can be scanned from W to V_a + W, in this case 0 to > 100V. The collision region comprises a central split tubular electrode E_m, two identical cylindrical electrodes E_{11}, E_{12} and two disc electrodes E_{10}, E_{13}. The function of these components varies with the nature of the measurement being carried out and will be described later in this section. The electron beam then passes through a series of cylindrical electrodes E_{14}-E_{16} and into the collection device comprising a negatively biased deflector, E_{17}, a positive collector E_{18} and a shield E_{19}.

The axis of the electrode system and the magnetic field must be closely aligned. Electrode E_6 has two apertures, one is axial (1 mm diameter) and the other is displaced off axis by 3 mm (0.2 mm diameter) so as to coincide with the off axis apertures of electrodes E_1-E_5. With the electric field

FIG. 6

Schematic Diagram of Electron Scattering Spectrometer

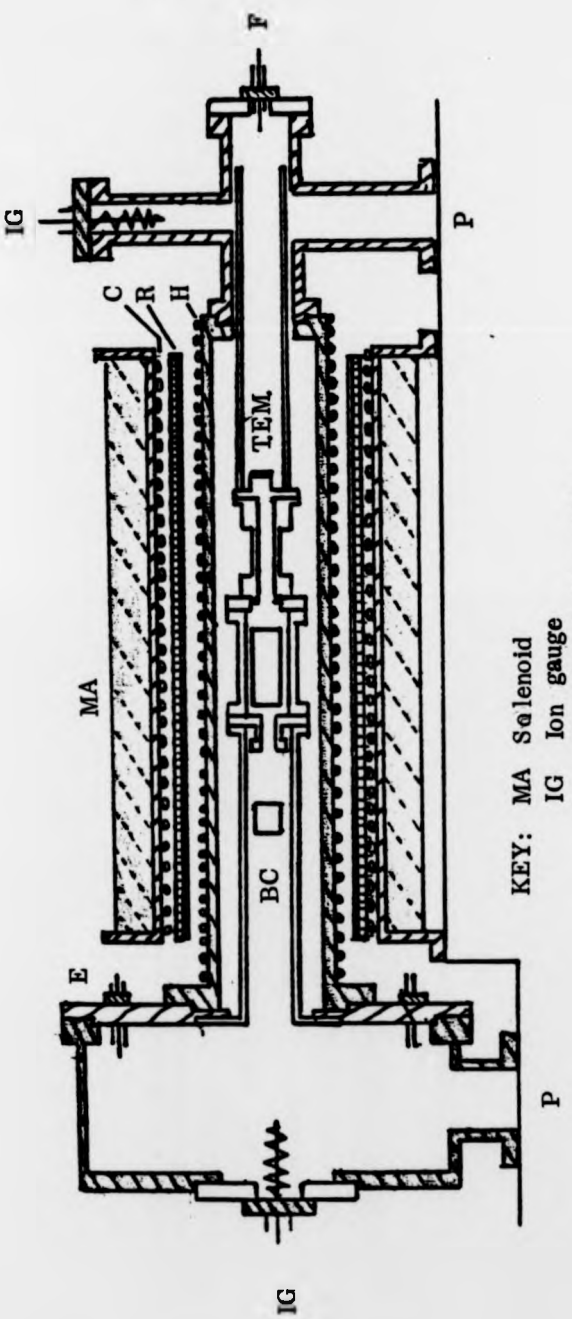

of the monochromator turned off, current is collected on E_7 which is due to electrons having passed through the 0.2 mm off-axis aperture in E_6. This current is maximised by adjusting the solenoid and magnetic field rectifier, see section 4:10. The electric field E of the monochromator is then turned on and minor adjustments to potentials and magnet complete the process.

4.2 MONOCHROMATOR DESIGN

The design parameters for the trochoidal electron monochromator in the present spectrometer were chosen after consideration of the experimental work carried out in this laboratory, the theoretical treatment of Roy [116] and the studies of Stamatovic and Schulz [112]. A compromise was reached between minimum energy spread, measurable transmitted currents and mechanical restrictions. Our monochromator produces an electron beam current of 10^{-8} - 10^{-9}A with an energy spread of better than 65 meV FWHM. The full width energy spread is typically less than 180 meV which includes the characteristic extended high energy wing of the asymmetric distribution function typical of the beam produced by a trochoidal electron monochromator. This high energy wing is minimised at low values of magnetic field flux density, about 100 gauss in the present instrument.

4.3 COLLISION REGION DESIGN

The collision region consists of three electrically insulated cylinders of 19 mm diameter plus exit and entrance disc electrodes. The central cylinder E_m is split longitudinally for two reasons (1) to allow the instrument to operate in a positive ionisation mode as described by Michejda [87] and [2] to allow more effective pumping and the introduction, at a later date, of a gas jet. In the trapped electron modes of operation only current collected on E_m, which defines the potential well, is recorded. The outer electrodes serve to guard the inner cylinder from the effects of field inhomogeneities in the vicinity of the entrance and exit discs, particularly when the system is operated in a modulated mode. The guard electrodes can be independently biased and, experimentally, a small potential difference between these and V_a can have a profound effect on the operation of the system.

4.4 BEAM COLLECTOR DESIGN

After leaving the collision region the transmitted electrons pass through a series of electrodes whose function varies with the type of experiment being carried out. In transmission spectroscopy they retard electrons scattered in the collision region. In the trapped electron mode they accelerate electrons which have escaped from the trapping potential well, into the beam collector. This type of beam collector has been used before in trapped electron work, initially by Rempt [94] and later by Hall [90]. The complicated crossed-field configuration generated by the negative deflector and the positive collector ensures that no electrons may be reflected back out of the collector while any positive ions

which may be formed in this region will be collected on the deflector.

4.5 MODES OF OPERATION

All electrodes are electrically biased with respect to one of two reference lines,(see Fig.11). These are -

(1) the cathode line: all electrodes including those associated with the monochromator up to electrode E_8 are biased with respect to this reference

(2) V_a line: all electrodes from E_9 onwards are biased with respect to this line and are scanned together when the accelerating voltage V_a (the voltage between the cathode line and the V_a line) is varied. An exception is found in fixed incident energy measurements where the scattered collector E_m is biased with respect to the cathode line.

Fig.7 shows variations in potential along the V_a line and its relation to the cathode line for the various modes of operation. These are

Mode 1: In the basic trapped electron mode, V_a is scanned with respect to the cathode line, W being constant. Scattered electrons collected on electrode E_m are detected by a Kiethley electrometer amplifier. This yields threshold energy loss spectra.

Mode 2: In the modulated electron trap the potential at the exit from the well is modulated by a small amount ΔW, the in-phase signal being detected by a Keithley lock-in amplifier. In this mode either V_a is scanned at fixed W yielding energy loss spectra or W is scanned at fixed V_a to yield information on excitation functions.

Mode 3: In the fixed incident energy mode the exit from the potential well is modulated, the in-phase signal being detected by a Keithley lock-in amplifier. Spectra obtained in this mode can be regarded either as energy loss spectra, the energy axis being eV_a or as residual energy spectra, the energy axis being eW or $e(V_{in} - V_a)$.

Mode 4: In this mode of operation, both the exit from the potential well and the incident electron energy are modulated. This results in the enhancement of structure due to excitation via temporary negative ion states and the separation, at deep well depths, of this structure from that due to direct excitation processes.

Mode 5: In the transmission mode of operation the three cylindrical electrodes E_{11}, E_m, E_{12} are modulated together with respect to V_a i.e. the incident electron energy varies between eV_a and $e(V_a + V_{mod})$. The in-phase signal on the beam collector is detected by a lock-in amplifier which yields the derivative of the transmitted current.

The electrodes between the collision region and the beam collector prevent any elastically or inelastically scattered electrons from reaching the detector.

Mode 6: Positive Ionisation Mode: Although our apparatus is capable of operating in this mode no work has yet been carried out and only a brief description will be given. For details see Michejda [87]. A small transverse crossed field voltage is applied between the two halves of E_m. Ions formed at energies near the threshold of ionisation are collected in the more negative side of E_m while low energy electrons present in the trap are collected on the more positive side. The ion current measured in this way is related to the ionisation cross-

FIG. 7

Modes of Operation of Electron Trap

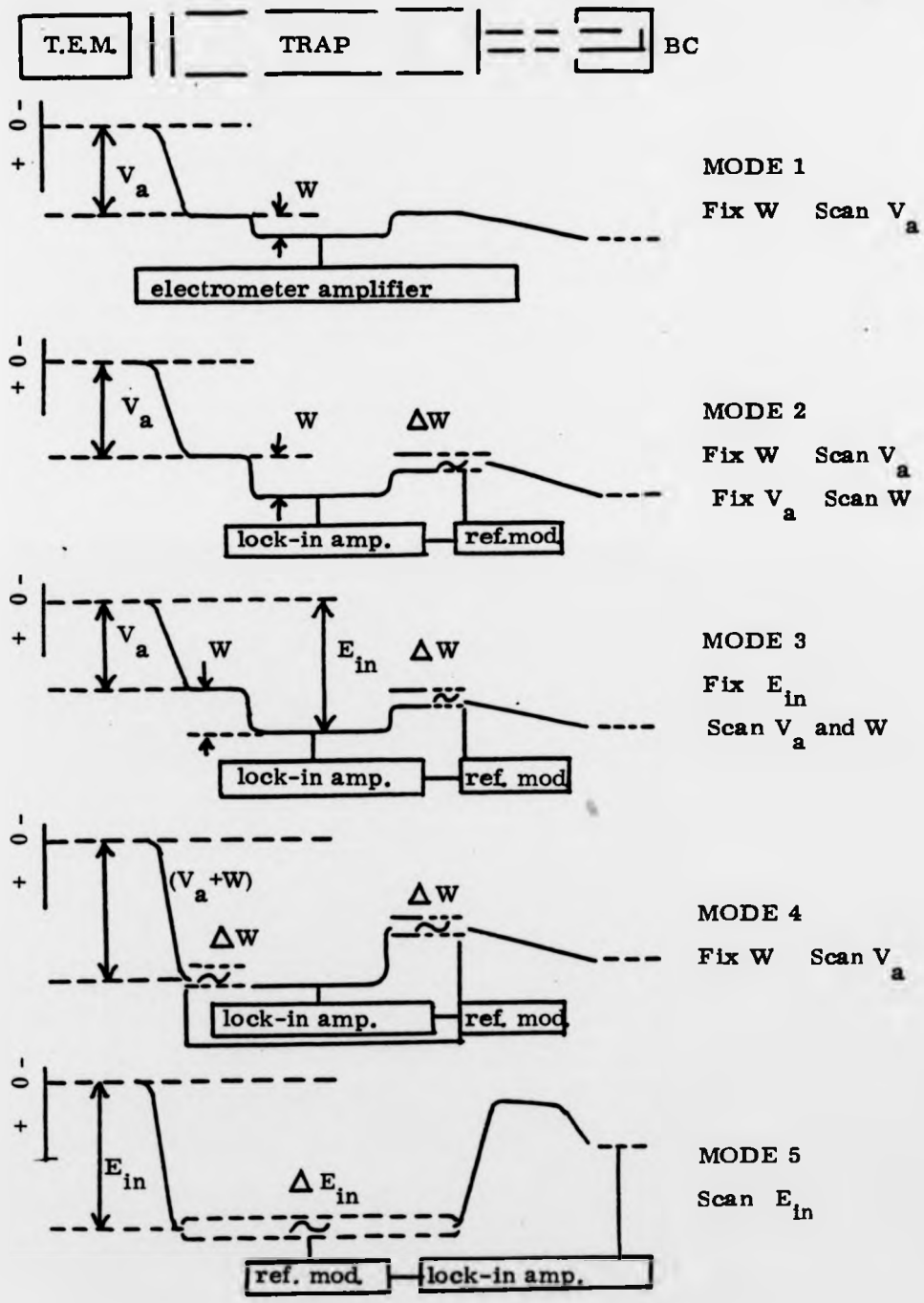

section and a knowledge of scattering gas density and scattering path length may yield quantitative results.

4.6 VACUUM SYSTEM

The main vacuum system shown in Fig. 8 is constructed entirely from EN58B stainless steel. The flanges, pump units and tanks are sealed with gold wire gaskets and the system is baked by external mineral insulated resistive heating cables wound directly onto the tanks. The internal electrode assembly is heated by Phillips Thermocoax heating cable wound directly onto support plates and cylinders. In this way the structure can be efficiently baked at 150°C.

The electrode system is installed intact including its various support tubes which allows alignment and insulation checks to be carried out before positioning in the vacuum tank. Electrical feedthroughs used are VG EF 2930 for biasing electrodes and VG EFT 91A where higher insulation is required. Pressure measurement is by means of two VG VIG 21 Bayard-Alpert type ionisation gauge heads (with thoria coated iridium filaments) placed at each end of the vacuum system as shown.

The pumping system is shown in Fig. 9 . The stainless steel vacuum tank assembly comprises two distinct pressure regions linked only by a 1 mm aperture, each region being pumped by an Edwards UHVM2 mercury diffusion pump (pumping speed 70 $\ell\ s^{-1}$) with liquid nitrogen cooled traps and Peltier cooled chevron baffles, backed by a common Edwards 2M4 mercury diffusion pump. This has a stalling pressure of 35 Torr and exhausts into a 10 dm^{-3} backing volume which can be either continuously or intermittently evacuated by a two-stage rotary

FIG. 8

Experimental System

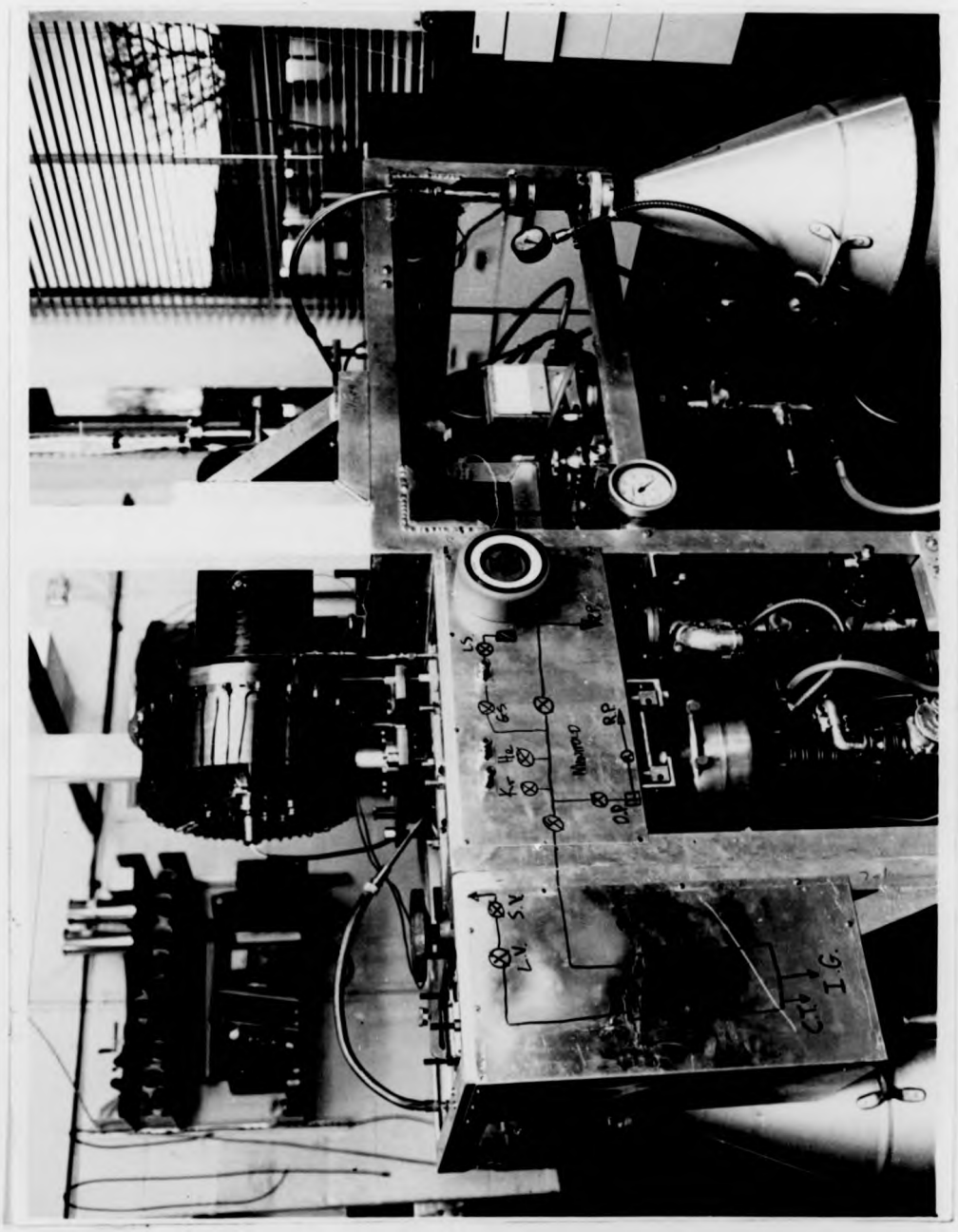

FIG. 8

Experimental System

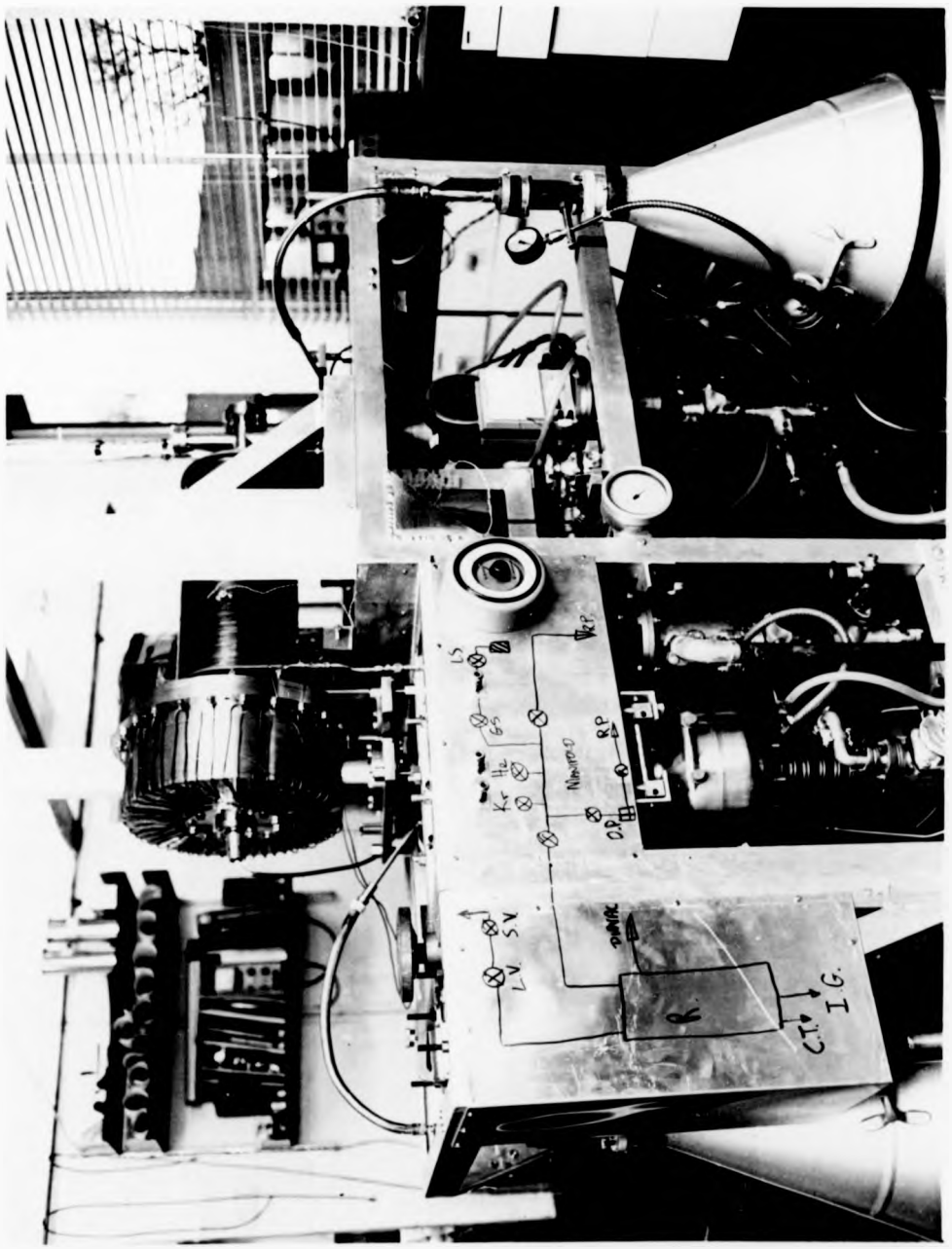

FIG. 8

Experimental System

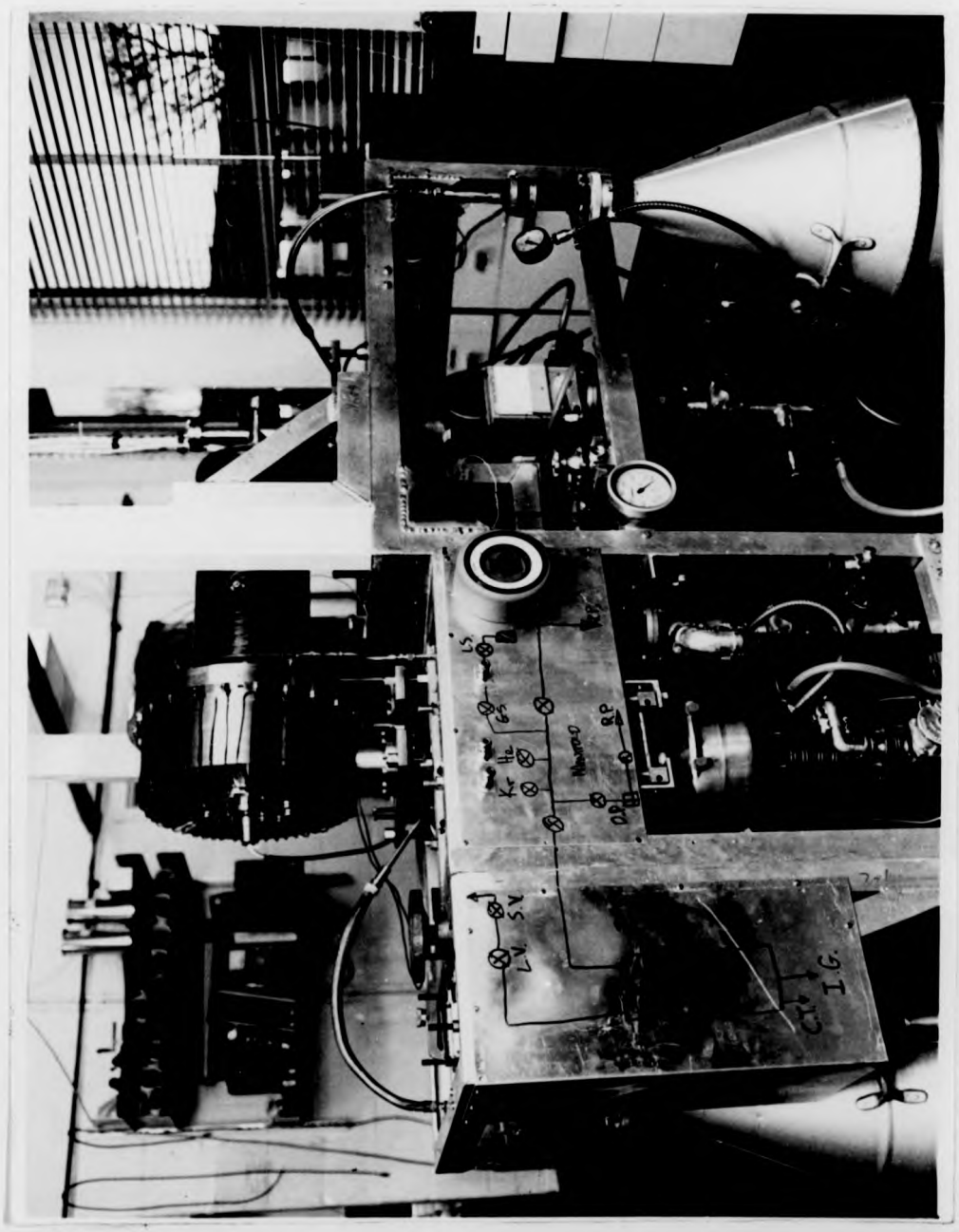

FIG. 9

Vacuum System

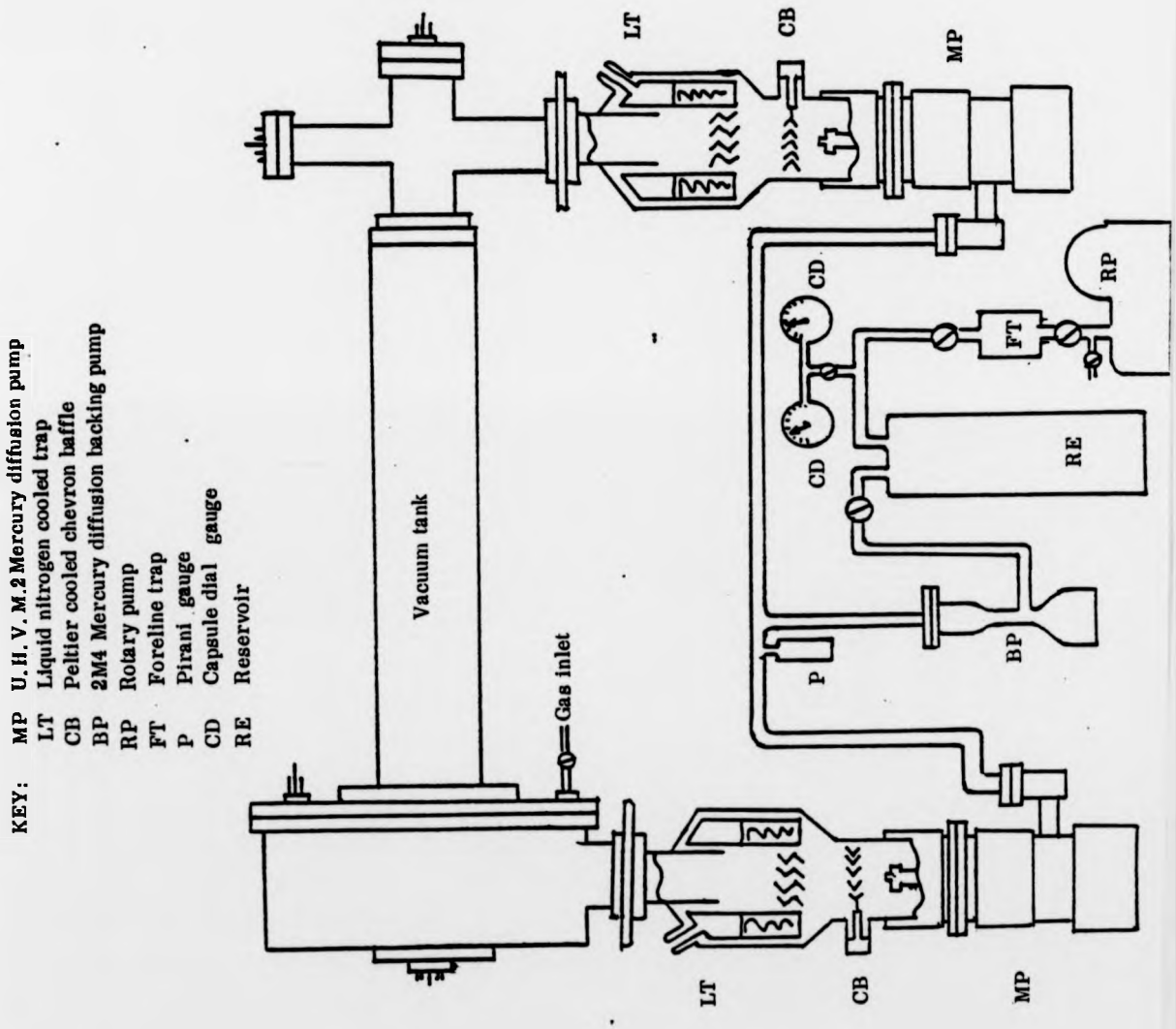

pump (Edwards ED 200) via an activated alumina foreline trap.

The combination of pumps employed provides a very clean high vacuum system with a base pressure of better than 4×10^{-9} torr after baking. There is no danger of contamination from the roughing pump, back streaming of gas from the UHVM2 is minimal, and samples can be recovered from the backing volume of the 2M4 if required. The foreline pressure of the 2M4 is measured by a Pirani gauge and the backing volume pressure is measured by capsule dial gauges.

4.7 GAS INLET SYSTEM

The gas inlet system is constructed entirely from stainless steel components connected by gold wire or copper gaskets. See Fig. 10. The system, including Hoke stainless steel bellows sealed valves, Leybold-Heraeus Diavac B corrosion proof diaphragm vacuum gauge (range 0-760 torr), VG MD6 bakeable all-metal leak valve and an ionisation gauge are located within an oven and all can be baked to a maximum temperature of 100°C. Separate gas inlets for helium, krypton, sample gas and sample liquid enter a manifold leading to a 4 dm^{-3} reservoir and then to the collision chamber via a leak valve in series with a stop-valve. A cold finger can be valved in to freeze out excess condensible gas after use. The inlet system is pumped by an Edwards 2M2A mercury diffusion pump (pumping speed 150 $\ell\ s^{-1}$) incorporating a liquid nitrogen cooled Edwards CT63 trap (charge

FIG. 10

Gas Inlet System

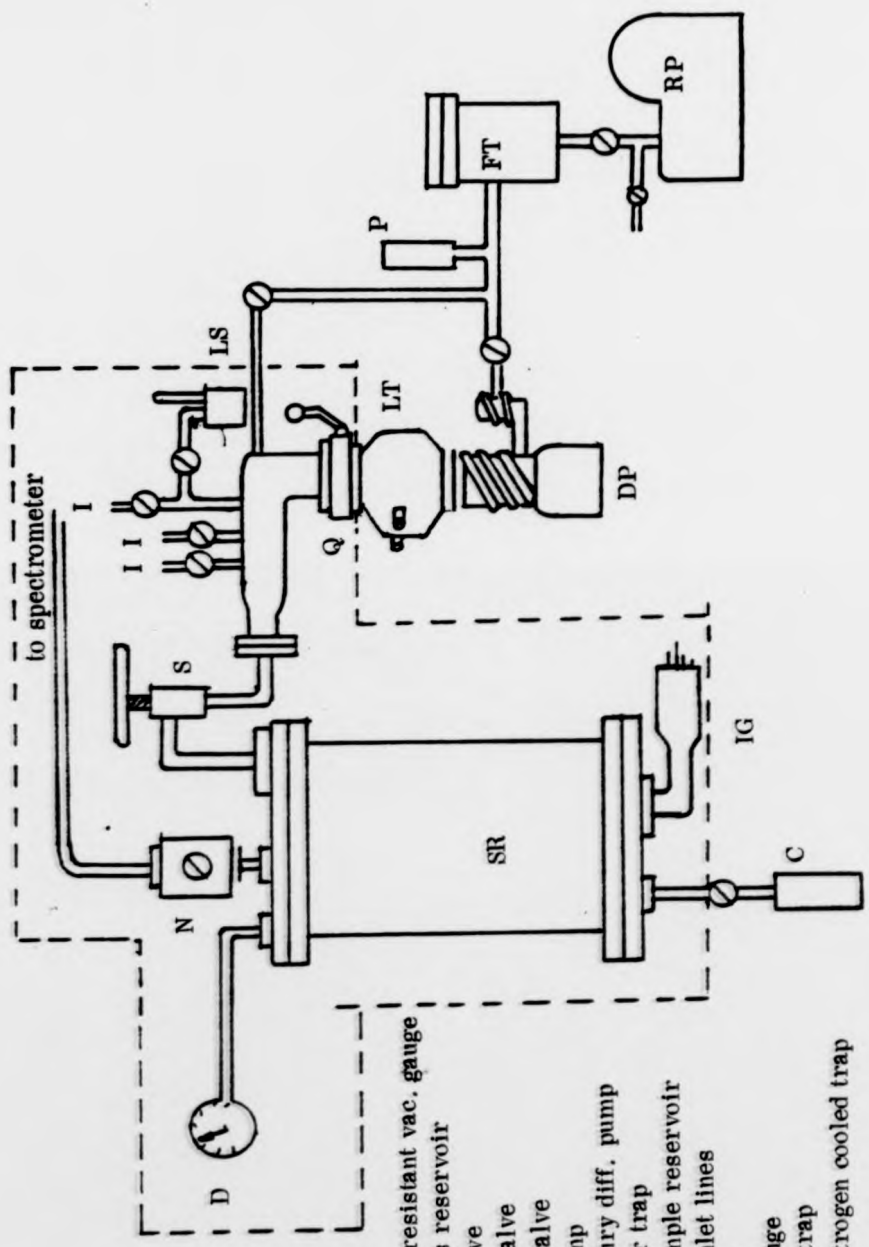

D Corrosion resistant vac. gauge
SR Sample gas reservoir
N Needle valve
S Isolation valve
Q Butterfly valve
RP Rotary pump
DP 2M2 Mercury diff. pump
C Cold finger trap
LS Liquid sample reservoir
I Various inlet lines
IG Ion gauge
P Pirani gauge
FT Foreline trap
LT Liquid nitrogen cooled trap

life 17 hours) and Edwards QSB63 quarter swing butterfly valve. It is backed by an NGN PSR/1 rotary pump via an activated alumina foreline trap. Pressures of approximately 10^{-6} torr are attainable giving a clean organic-free system.

4.8 INTERLOCK PROTECTION OF APPARATUS

The apparatus is protected against various supply failures in three independent sections as follows:-

Interlock (I)

Main System		Protection
UHVM2	mercury diffusion pump	cooling water temp.
2M4	mercury diffusion pump	cooling water flow
ED 200	rotary pump	vacuum failure
Peltier Baffles		liquid air cooled traps (UHVM2)
Filament Power Supply		power failure
Vacuum Tank Ovens		

Interlock (II)

Gas Inlet System		Protection
2M2A	mercury diffusion pump	cooling water flow
PSR/1	rotary pump	cooling water temp.
ovens		vacuum failure
		liquid air cooled traps (2M2A)
		power failure

Interlock (III)

	Protection
Solenoid	cooling water flow
	cooling water temp.
	power supply temp.

A time delay of 1 sec. on mains failure in interlocks I and II avoids the danger of mains fluctuations causing the apparatus to trip off. To aid fault diagnosis, the initial cause and time of a shut down are indicated separately from subsequent failures.

4.9 AUTOMATIC LIQUID AIR FILLING SYSTEM

Probes monitor high and low levels in the liquid air cooled traps of the UHVM2 pumps which are periodically filled during an automatic timing sequence.

The traps are filled for 15 minutes out of every 90 minutes and this filling is controlled by the high level monitors which actuate solenoid valves allowing a small compressor to pressurise storage vessels and force the liquid into the appropriate trap. The low level sensors serve as the safeguard in interlock (I).

4.10 MAGNETIC FIELD

The uniform axial magnetic field required in this experiment is provided by a solenoid. The field can be varied continuously from 0 weber m^{-2} to 3 x 10^{-2} weber m^{-2} corresponding

to a maximum current of 14 amperes stable to within 0.1%.

A mineral insulated cable comprising a copper conductor and copper sheath, wound on a water-cooled cylindrical former allows the necessary fields to be generated with the safe dissipation of power (980W max.) in the windings. The solenoid was made sufficiently long to allow the entire electrode system to be immersed in that part of the axial magnetic field sufficiently remote from the ends to avoid the need for compensating coils. Alignment of the magnetic field with the axis of the electrode system can be carried out using the system of adjusting screws incorporated in the solenoid supports. The uniformity of the magnetic field is increased by inserting a cylinder comprising alternate hoops of μ-metal and aluminium pressed together on a brass former within the solenoid (90). The effect of this is the alignment of the field perpendicular to the surface of each high permeability μ-metal hoop, thus minimising any irregularities in the field due to the solenoid windings. Alignment of the field with respect to the electrode system is also possible as the μ-metal/aluminium cylinder can be independently adjusted.

4.11 ELECTRICAL EQUIPMENT

The unit supplying variable potentials to the electrode system was built to specification for this experiment by Stirling University Shared Technical Services electronics section. The aim was to provide a versatile, high stability, low noise, unit. Fig. 11 shows a typical layout for recording trapped electron spectra. For modulation of electrodes in electron transmission and modulated trap studies, a unit is incorporated which allows any electrode, or group of electrodes, to be modulated with

FIG. 11

Electrical Biasing of Spectrometer

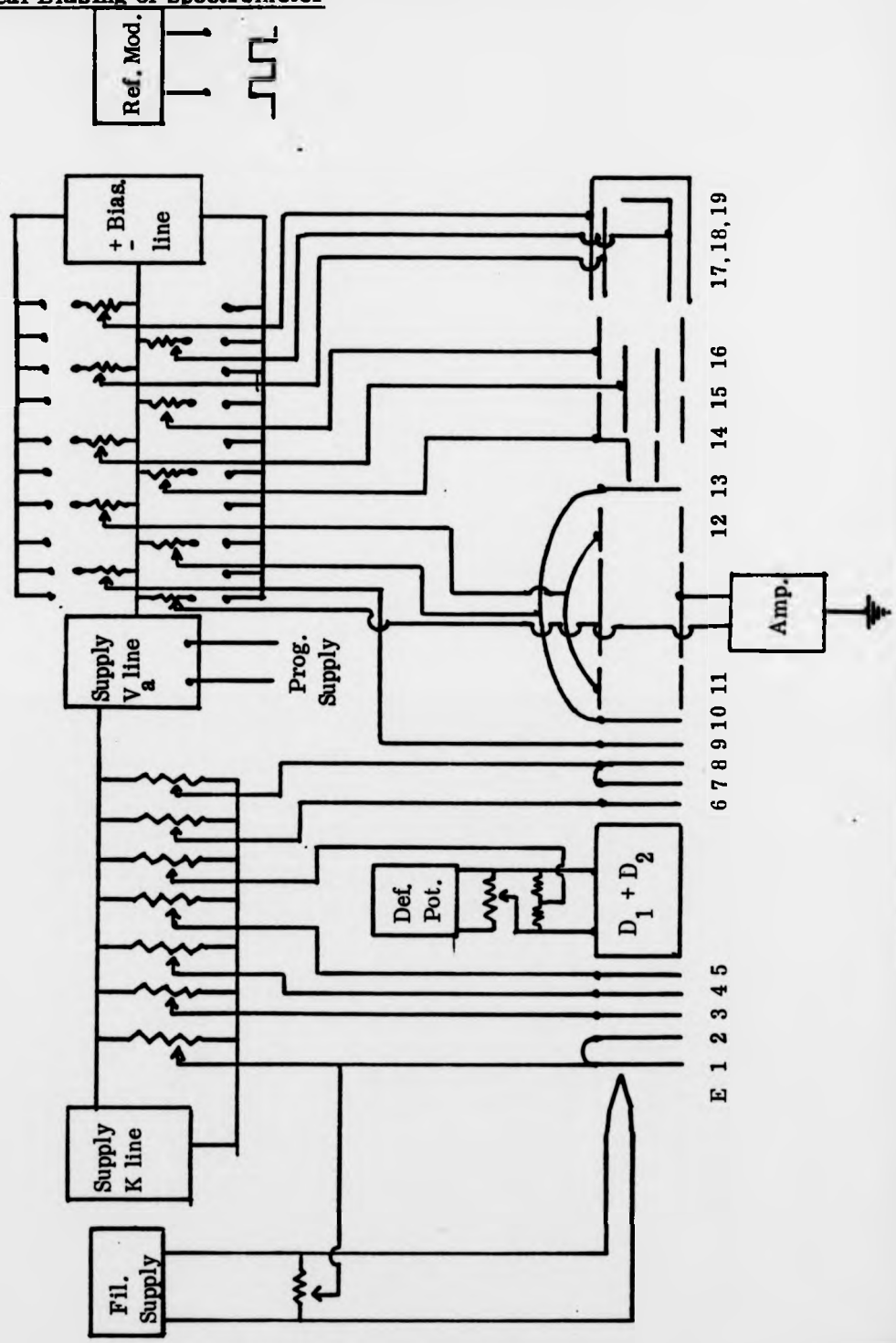

respect to any reference point in the system. A Keithley lock-in amplifier detects the in-phase signal in these modes of operation. The trapped electron current is measured by a Keithley (model 640) vibrating capacitor electrometer amplifier and recorded on a Bryans x-y recorder.

CHAPTER 5

RESULTS AND DISCUSSION

(He, N_2, CO_2, CS_2, COS)

CHAPTER 5

5.1 EXPERIMENTAL RESULTS AND DISCUSSION

Introduction

This chapter contains results obtained on the excitation of helium, nitrogen, carbon dioxide, carbonyl sulphide and carbon disulphide by low-energy electron impact. The spectra are presented as traces of signal intensity (trapped electron current) in arbitrary units versus either accelerating voltage V_a or well depth W. All spectra were recorded on an X-Y chart recorder.

5.2.1 Helium

Results

Threshold energy loss spectra obtained with the trapped electron technique in its conventional (d.c.) mode of operation are presented in Fig.12 for a variety of well depths. Optical transitions are indicated[121], the 1^1S-2^3S transition being used to calibrate the incident electron energy scale. Table 5 compares the known transition energies in helium with those observed in Fig.12. The fall-off in scattered electron current above the ionisation energy is due to the collection of positive ions which can migrate to the scattered electron collector in this instrument. Fig.13 shows the corresponding energy loss spectra obtained using the modulated (a.c.) trapped electron technique. Again the 1^1S-2^3S transition is employed for energy calibration. Note that ions do not contribute to the in-phase signal. Table 5 compares optical and observed transition energies.

The experimental curves presented in Fig.14 were obtained in the scanned well depth mode of operation of the

TABLE 5

Electronic Energy Levels of Helium

Assignment	Observed Energy (eV) Present Results				
	Spectroscopic value (eV)[121]	d.c. trap (Fig. 12)	mod. trap (Fig. 13)	fixed E_{in} (Fig. 17)	$\Delta E_{in} + \Delta W$ (Fig. 16)
2^3S	19.820	19.82	19.82	19.82	19.82
2^1S	20.616	20.59	20.60	20.60	20.61
2^3P	20.964	20.96	20.96	20.96	20.95
2^1P	21.218	21.21	21.20	21.21	21.20
3^3S	22.719	22.69	22.70	22.73	22.70
3^1S	22.921	22.92	22.96	22.95	22.97
3^3P, 3^3D, 3^1D, 3^1P	23.08	not resolved	-	-	-
n = 4	23.59-23.74	23.61	23.65	23.65	23.64
n = 5	23.97-24.04	23.99	24.00	23.97	23.96
n = 6	24.17-24.21	24.15	24.20		

FIG. 12a

Energy Loss Spectrum of Helium (d.c. trap)

Residual electron energy < 0.05 eV

FIG. 12b

Energy Loss Spectrum of Helium (d. c. trap)

Residual electron energy < 0.3 eV

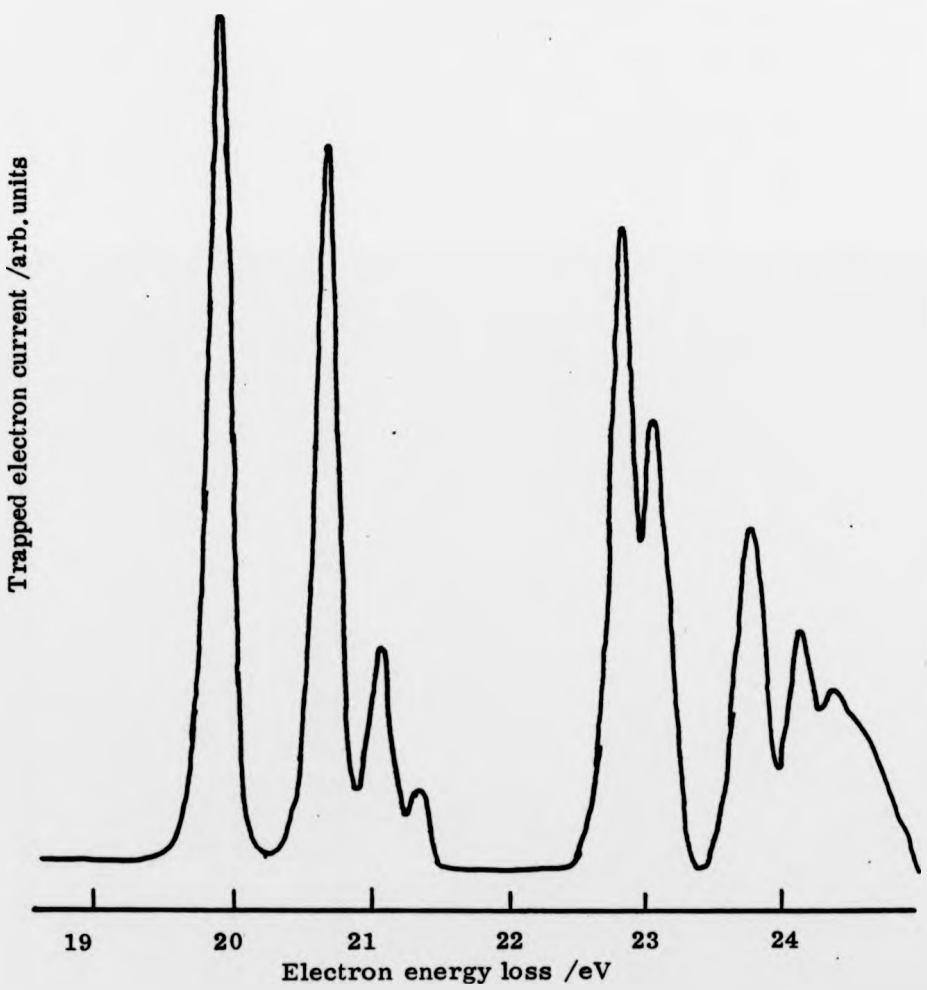

FIG. 12c

Energy Loss Spectrum of Helium (d.c. trap)

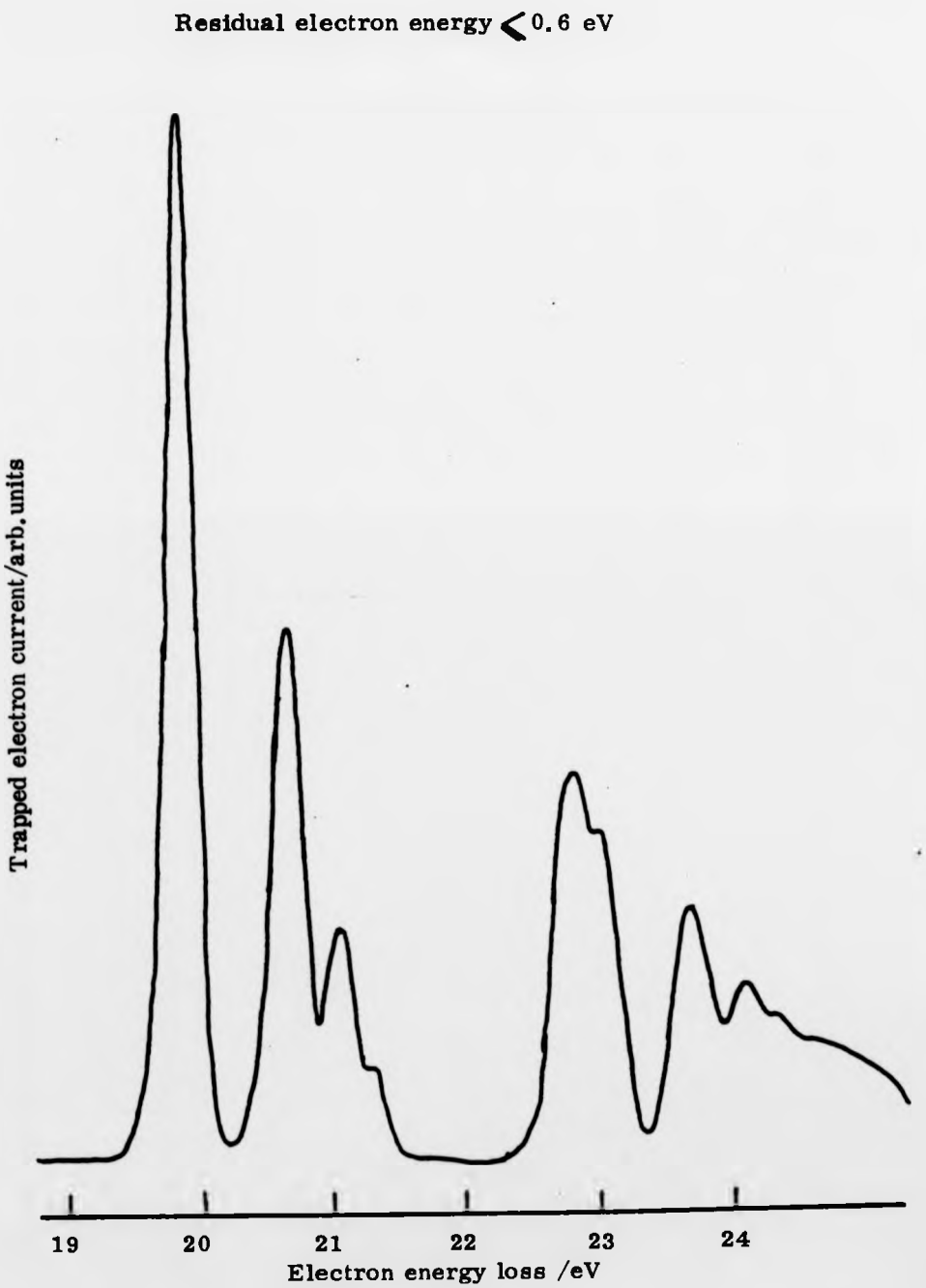

FIG. 13a

Energy Loss Spectrum of Helium (a. c. trap)

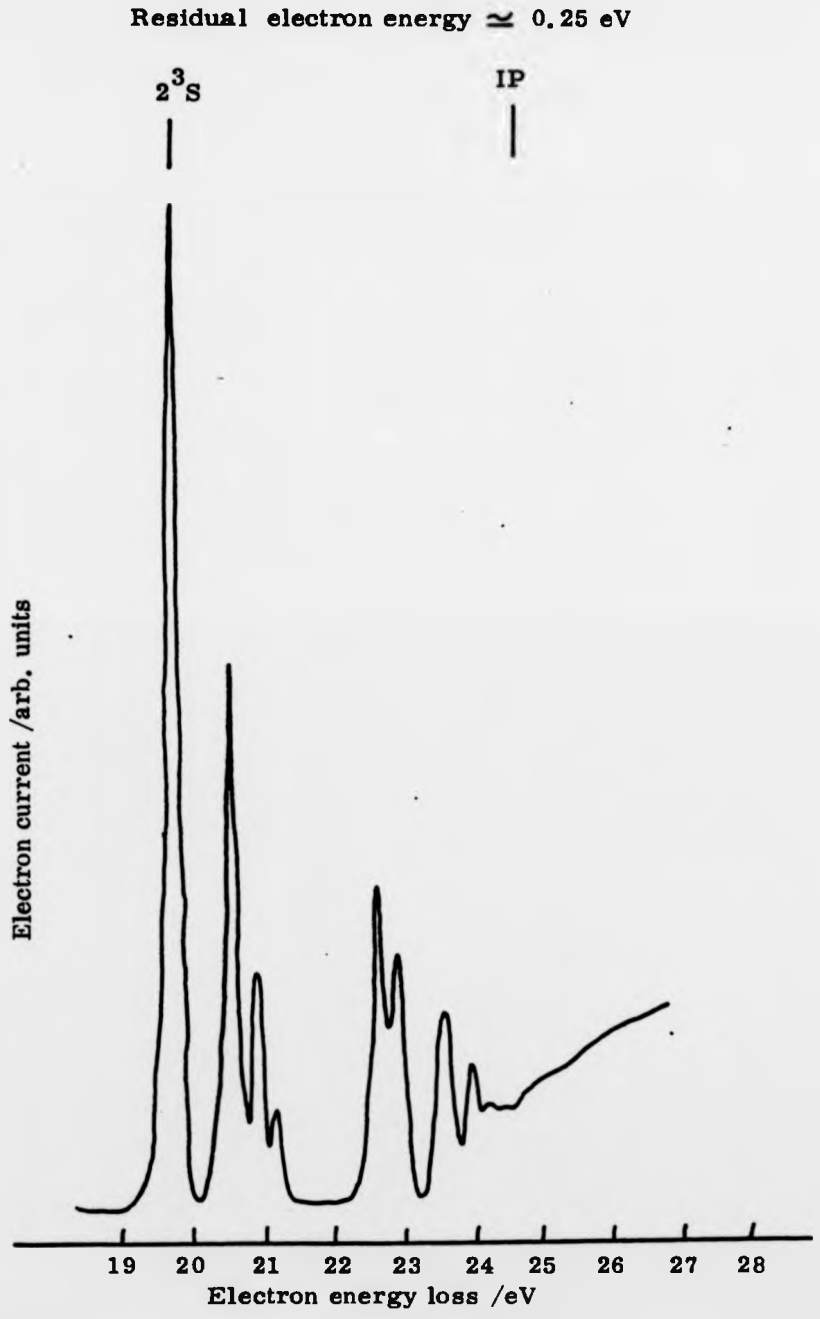

FIG. 13b

Energy Loss Spectrum of Helium (a.c. trap)

Residual elctron energy≃2.8 eV

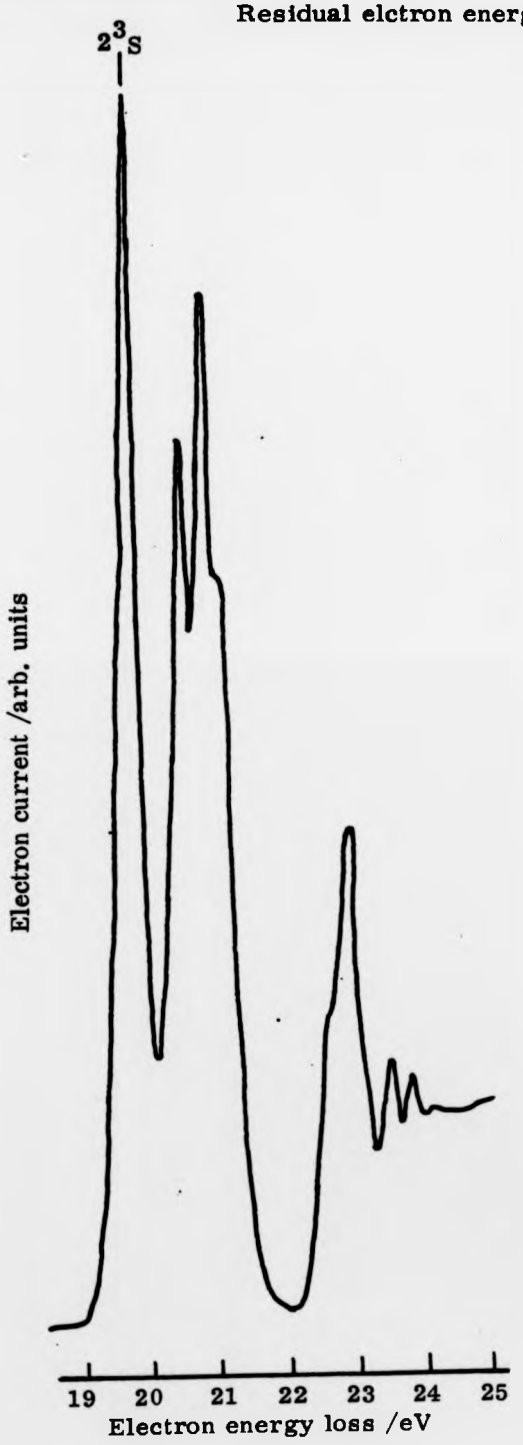

FIG. 13c

Energy Loss Spectrum of Helium (a.c. trap)

Residual electron energy $\simeq$ 5.0 eV

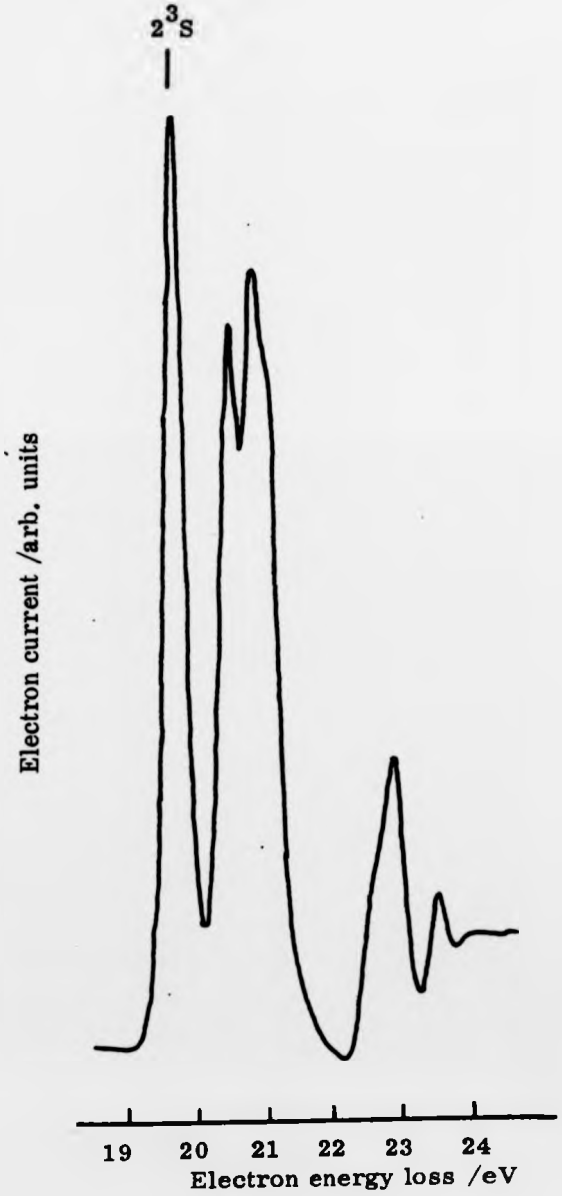

FIG. 13d

Energy Loss Spectrum of Helium (a.c. trap)

Residual electron energy $\simeq$ 11.3 eV

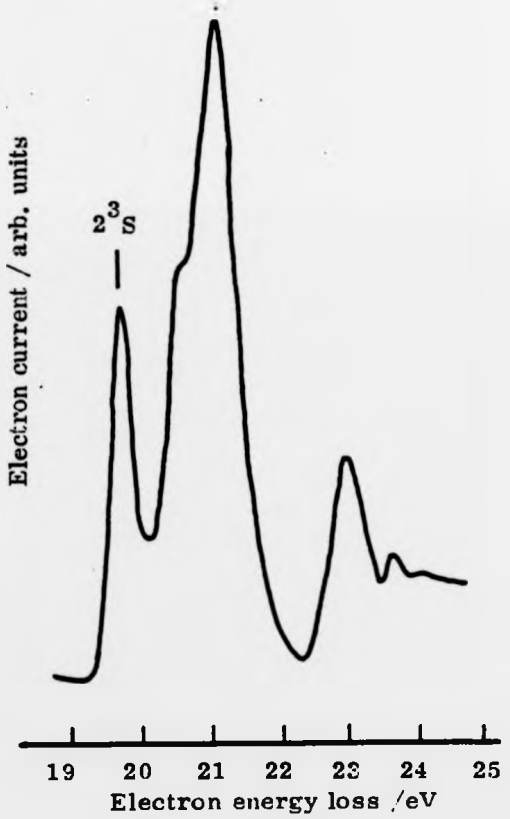

FIG. 14

Electron Impact Excitation Functions of Helium

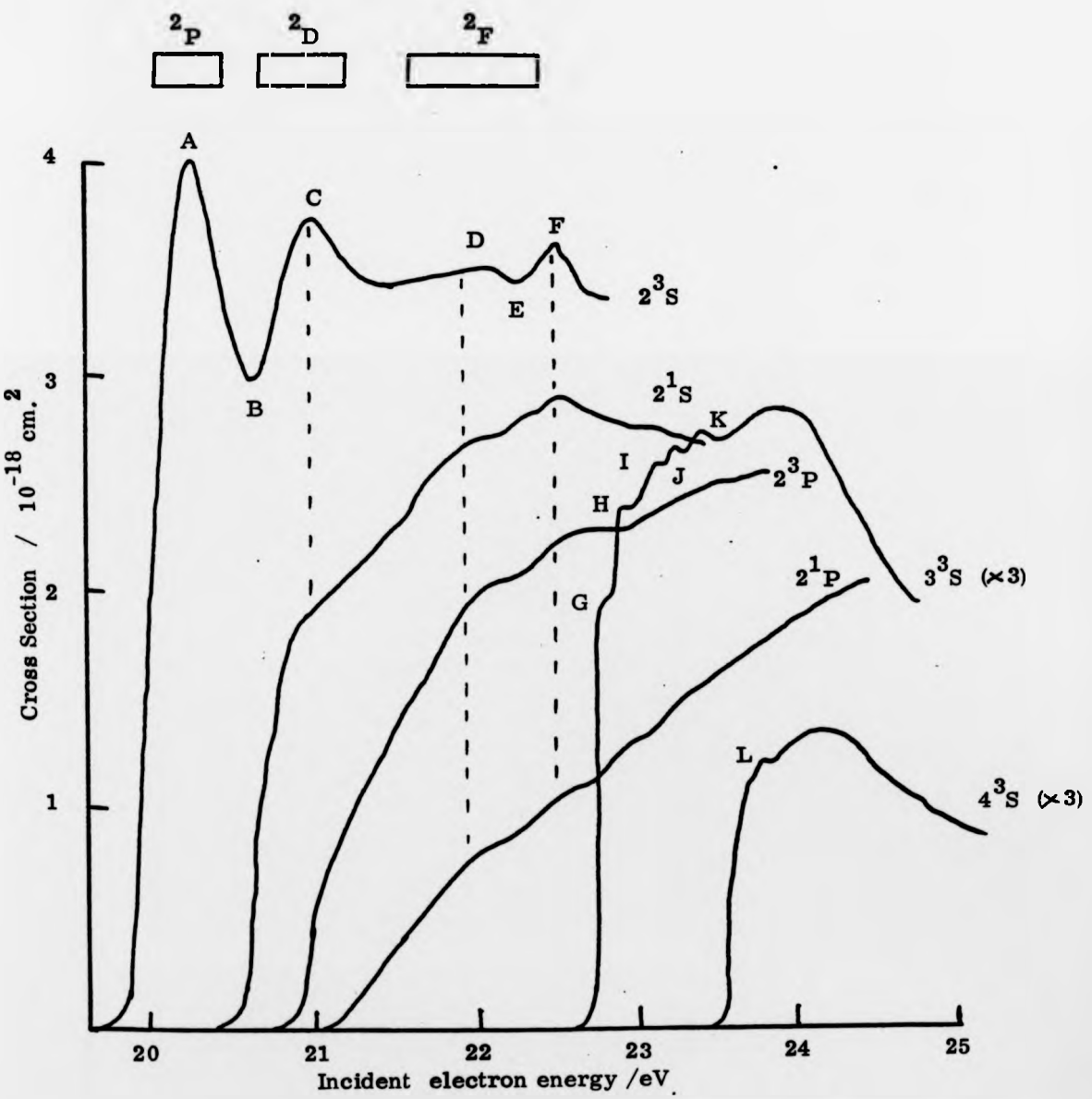

modulated trap. To obtain these, firstly V_a was tuned to the excitation energy of the relevant transition E_{ex}. This can be done very easily, as, at any W the position of maximum intensity of an energy-loss peak is at $eV_a = E_{ex}$. Then W was scanned. Although in principle the applied well depth (WDA) should be scanned from zero volts in order to trace out the individual excitation function from threshold, in practice the effective well depth W will differ from WDA by an amount dependent on contact potentials within the spectrometer,

i.e. $W = (WDA + f)$.

We must therefore determine f. This cannot be done simply by observing the experimental onset and equating W to zero at this point, since the observed threshold behaviour is a result of the convolution of an apparatus function with the excitation function. To overcome this we have digitised our apparatus function (Fig.13) and also the 2^3S threshold excitation function of Brunt et al.,[122] at 10 mV intervals. This latter excitation function was recorded with an estimated energy spread, FWHM ≈ 13 meV. Convolution of these two functions yields a curve which is a good fit to our observed threshold behaviour (Fig.15). From this we deduce that our true onset lies at a point approximately 90 mV higher than the intercept of the tangent of steepest slope. This allows us to calibrate our well depth by positioning the true onset for the 2^3S excitation function at W = 0. This yields

$$(WDA + f) = 0$$

where $$f = + 0.40 \pm 0.02V.$$

We estimate the accuracy of the positions of structures in the excitation functions obtained in this way to be ± 40 meV. These values are compared with those determined by other methods in

FIG.15

Estimation of W from 2^3S Onset

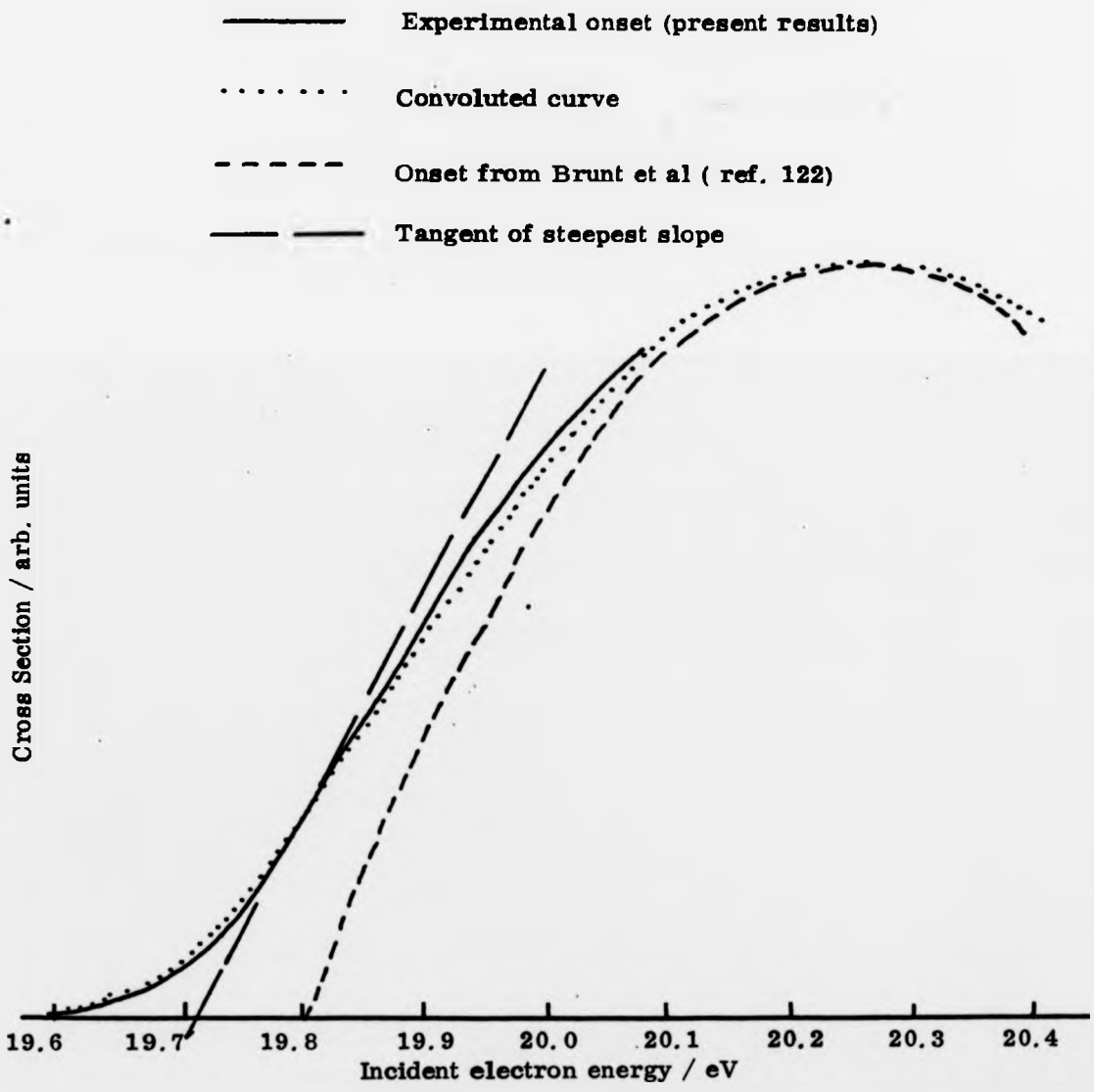

Table 6.

Fig.16 shows spectra obtained by modulating both the incident electron energy and the well depth. These composite spectra exhibit two series of peaks, one arising from direct excitation being independent of well depth, the other due to resonance excitation processes moving along the V_A axis with changing W. This has been explained in Section 3.5. The corresponding modulated trap energy loss spectra are shown for comparison. Data from these figures are tabulated in Tables 5 and 6.

Fig.17 presents spectra obtained using the fixed incident energy mode of operation. These spectra can be considered as traces of intensity versus either residual electron energy or electron energy loss. Table 5 compares transition energies observed in Fig.17 with optical values.

Fig.18 shows a typical electron transmission spectrum for helium. The derivative of transmitted current versus electron energy is plotted, the $(1s2s^2)^2S$ resonance centered around 19.34 eV being clearly shown. This particular mode of operation was not fully explored in the present work.

5.2.2 Discussion

(a) Energy Loss Spectra

The simple energy loss spectra presented show how spectral transitions may be positioned and how the magnitudes of cross-sections depend on the energy at which they are sampled. All modes of operation yield consistent results.

Fig.19 shows the total yield of electrons scattered from helium (incident electron energy E_{in} 22-26 eV, scattered electron energy ≈ 0.05 eV) as a function of the incident energy.

TABLE 6

POSITION OF STRUCTURE IN HELIUM EXCITATION FUNCTIONS (eV)

Structure in metastable cross-sections					Structure in Optical Excitation Function Experiment		Structure in Electron Scattering Differential Cross-Sections Experiment		Present Results	
Theory			Experiment		Heddle et al. (125)		Pichou et al. (126)	Andrich (127)	Excitation Functions (with channel of observation) (from Fig.14)	From total excitation cross-section (from Fig.16e)
Classification	Oberoi & Nesbet (123)	Nesbet (124)	Classification	Brunt et al. (122)	(3^3S)	(4^3S)	(3^3S)	(2^3S)		
$1s(2s2p)^2$	20.17		^2P	20.27					2^3S 20.32 A	19.94 a 20.62 b
$1s(2p^2)^2D$	20.85		^2D	20.955					2^3S 20.65 B	
									2^3S 20.96 C	20.87 c 21.37 d
									n=2 22 D	
$1s(3s^2)^2S$		22.441	^2S	22.43-22.47				^2S 22.44	2^1S 22.35 E	
$1s(3s3p)^2P$		22.608	^2P	22.64				^2P 22.60	n=2 22.52 F	22.57 e
$1s(3s3d)^2D$		22.645	^2D	22.70				^2D 22.66		
$1s(3s3p^-)^2P$		22.703	^2P	22.79	22.8		22.8	^2S 22.88	3^3S 22.82 G	22.77 f
$1s(3ss^-)^2S$		22.877	^2S	22.87-22.89						
$1s(3p^2)^2D$		22.938		22.93	22.95		22.93		3^3S 22.93 H	23.05 g
				22.99						
				23.05						
			$1s(4s^2)^2S$	23.42-23.47	23.28		23.20		3^3S 23.35 I	23.19 h
			$1s(4s4p)^2P$	23.53	23.50		23.54		3^3S 23.56 J	23.57 i
			$1s(4p^2)^2D$	23.57						
			$1s(4p^2)^2S$	23.67		23.7				
				23.86						
				23.96		23.94			4^3S 24.0 K	24.0 j
										24.3 k

FIG. 16a

Energy Loss Spectrum of Helium (composite $\Delta E_{in} + \Delta W$)

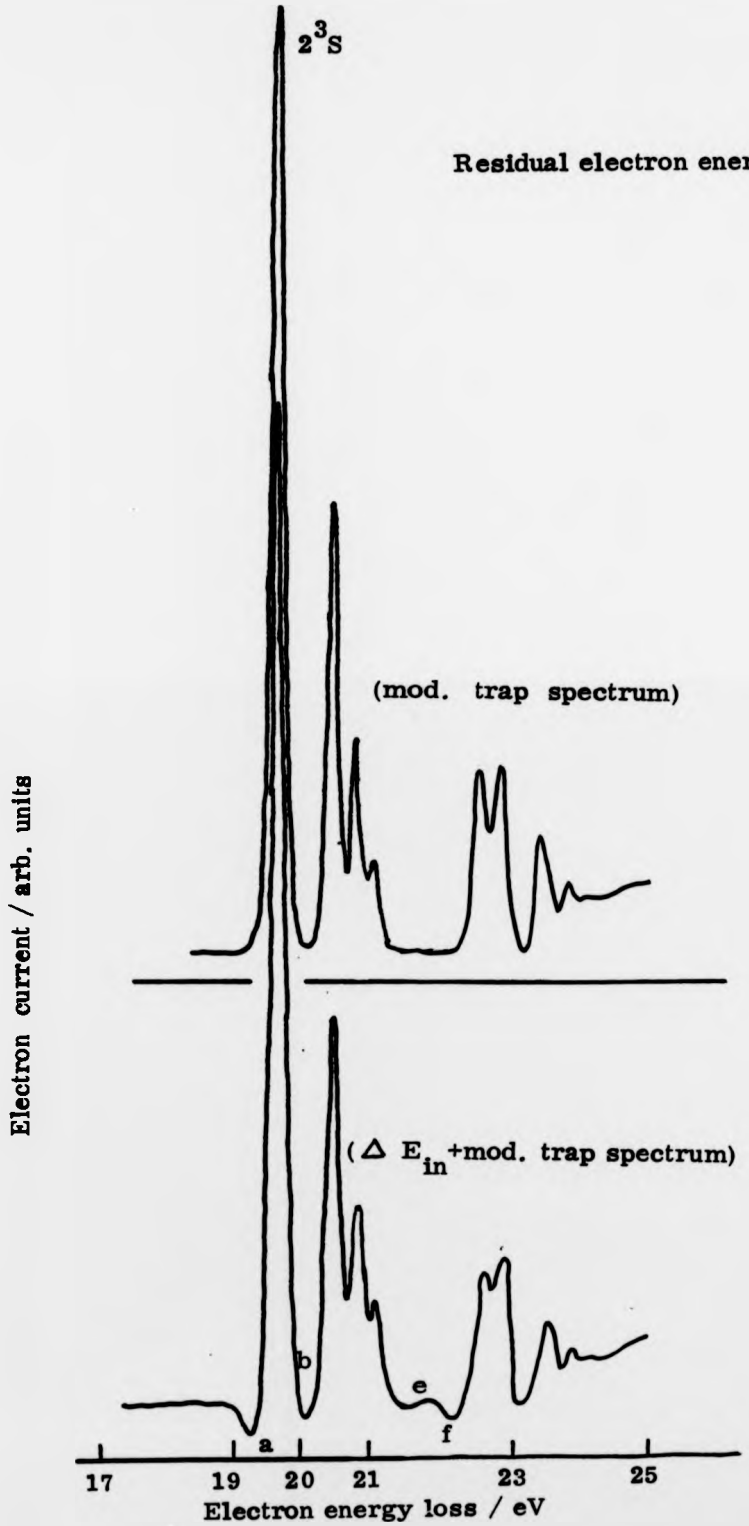

FIG. 16b

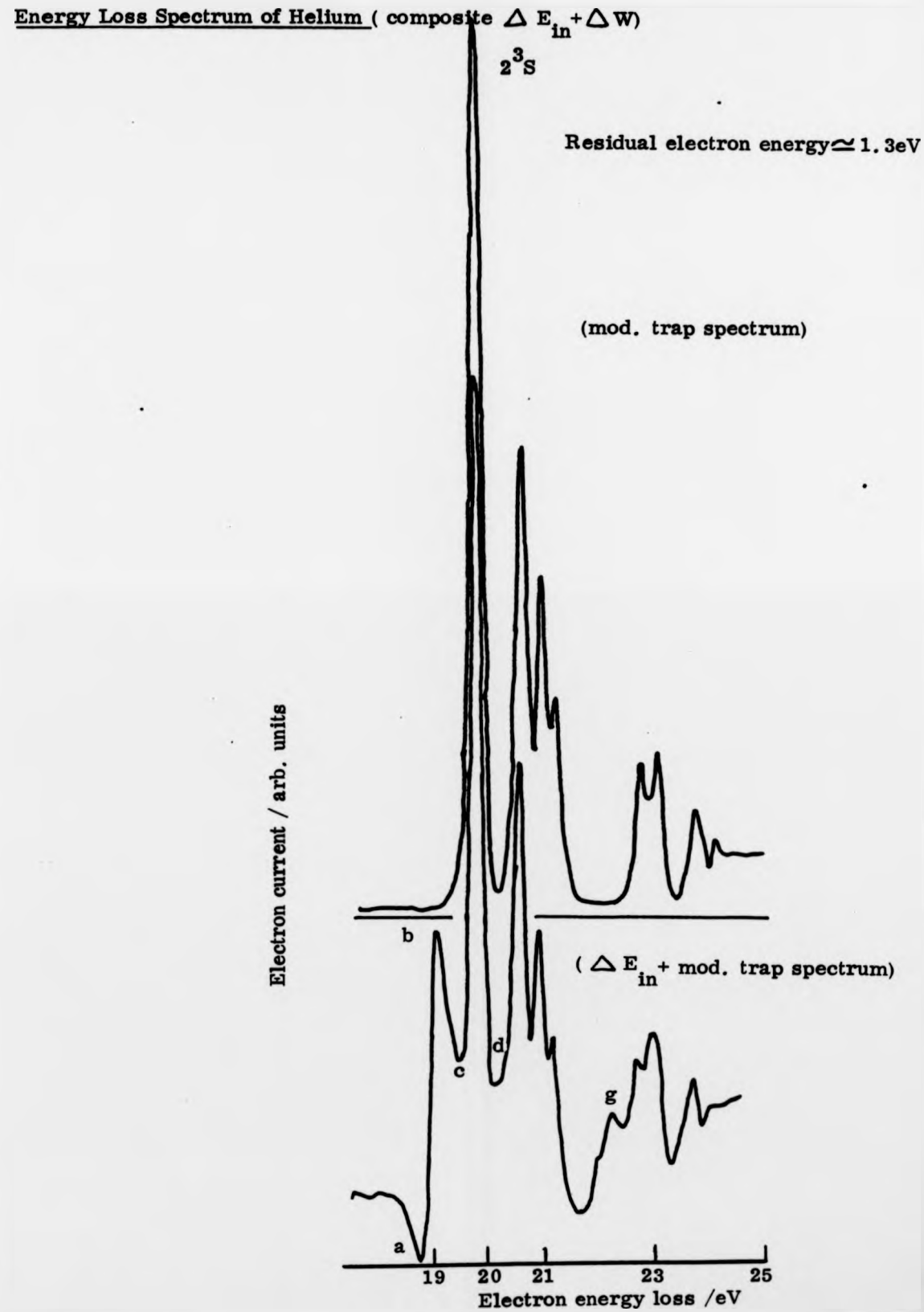
Energy Loss Spectrum of Helium (composite △ E_in + △ W)
2³S
Residual electron energy ≃ 1.3eV
(mod. trap spectrum)
(△ E_in + mod. trap spectrum)
Electron current / arb. units
a
b
c
d
g
19
20
21
23
25
Electron energy loss /eV

FIG. 16c

Energy Loss Spectrum of Helium (composite $\Delta E_{in} + \Delta W$)

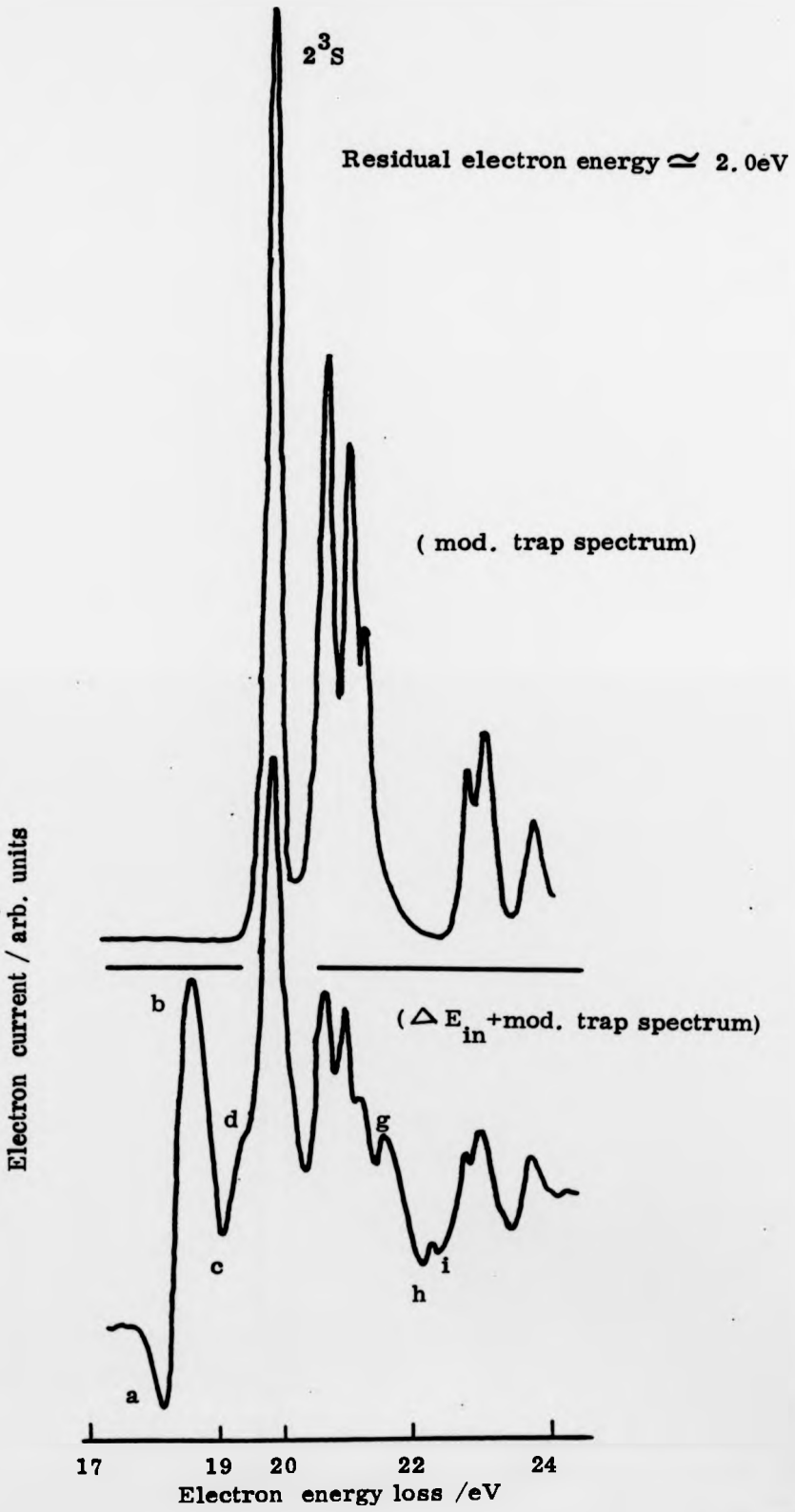

FIG. 16d

Energy Loss Spectrum of Helium (composite $\Delta E_{in} + \Delta W$)

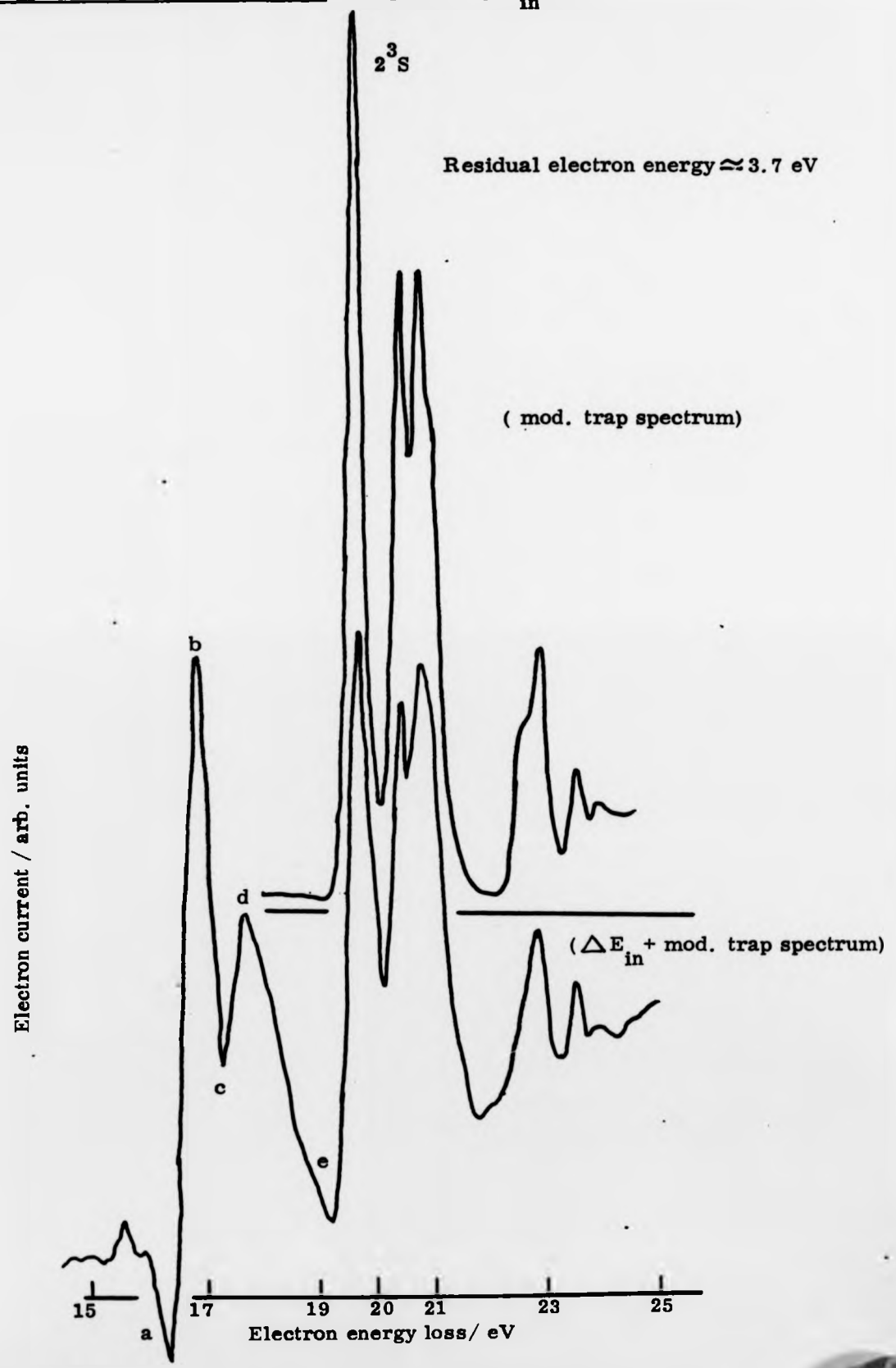

FIG. 16e

Energy Loss Spectrum of Helium (composite $\Delta E_{in} + \Delta W$)

Residual electron energy≃11.3eV

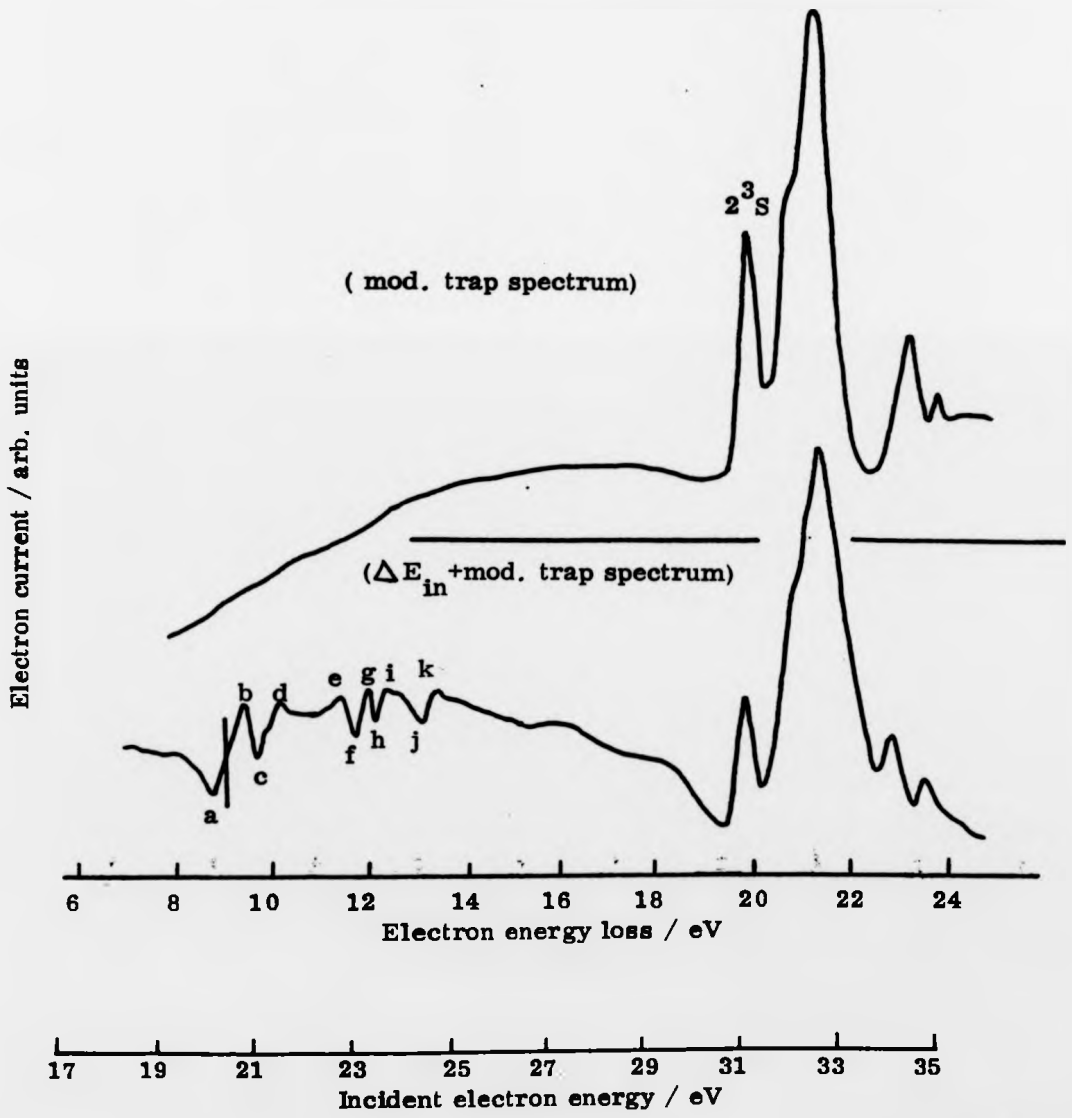

FIG. 17a

Fixed Incident Energy Spectra of Helium

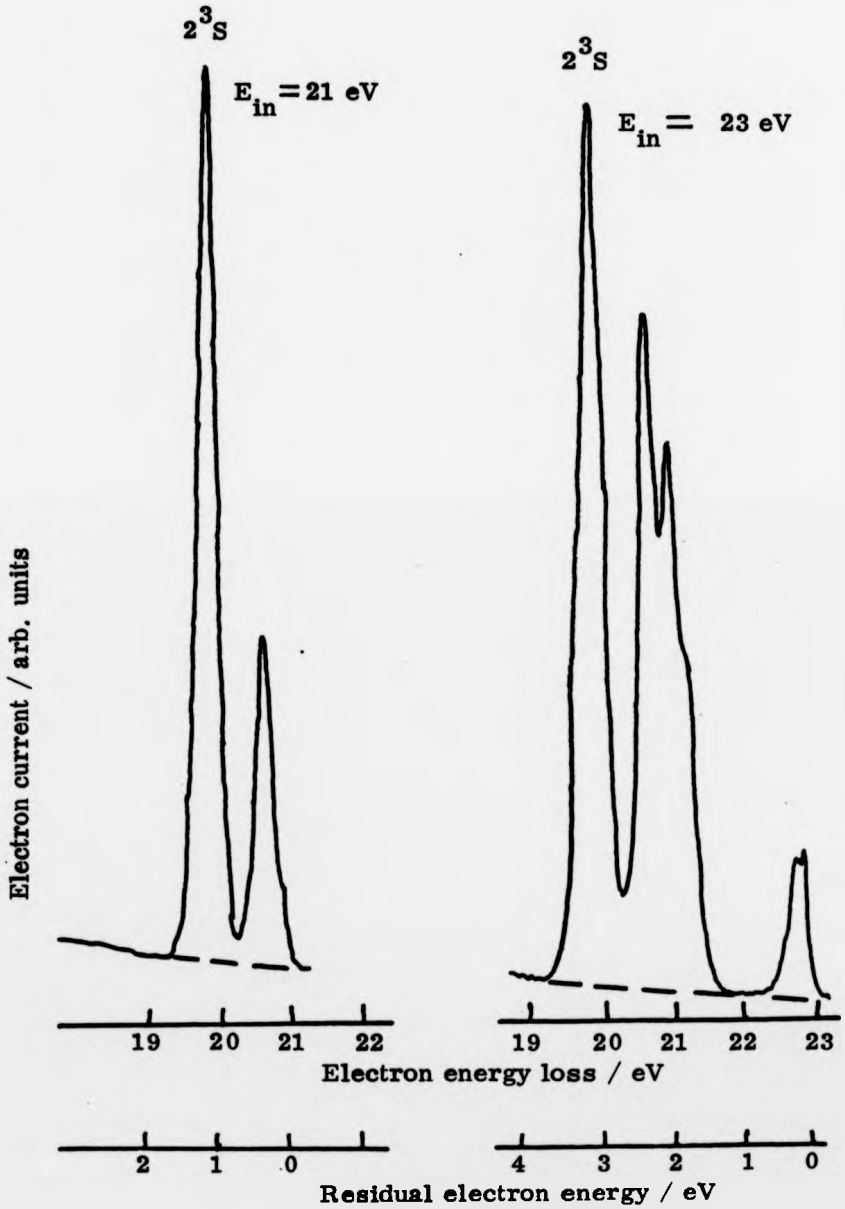

FIG. 17b

Fixed Incident Energy Spectra of Helium

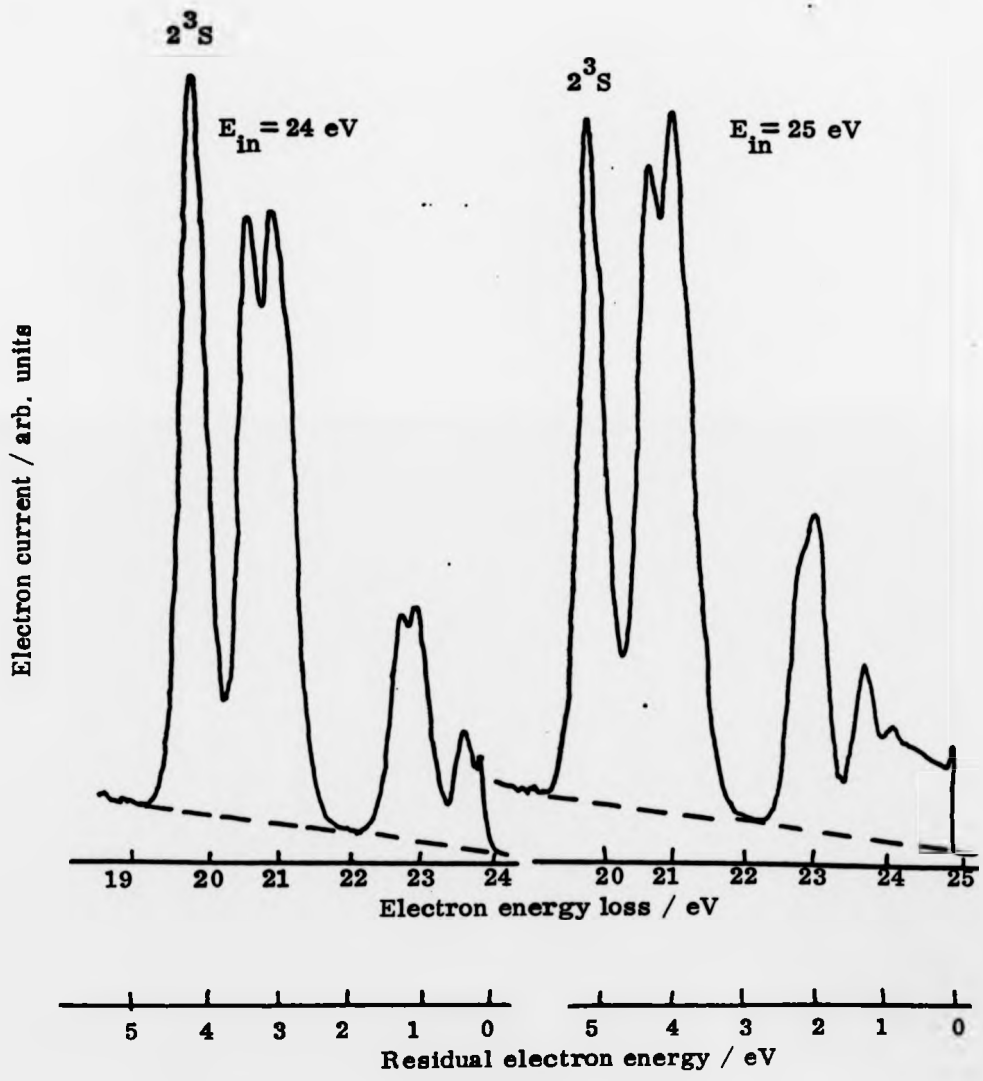

FIG. 17c

Fixed Incident Energy Spectra of Helium

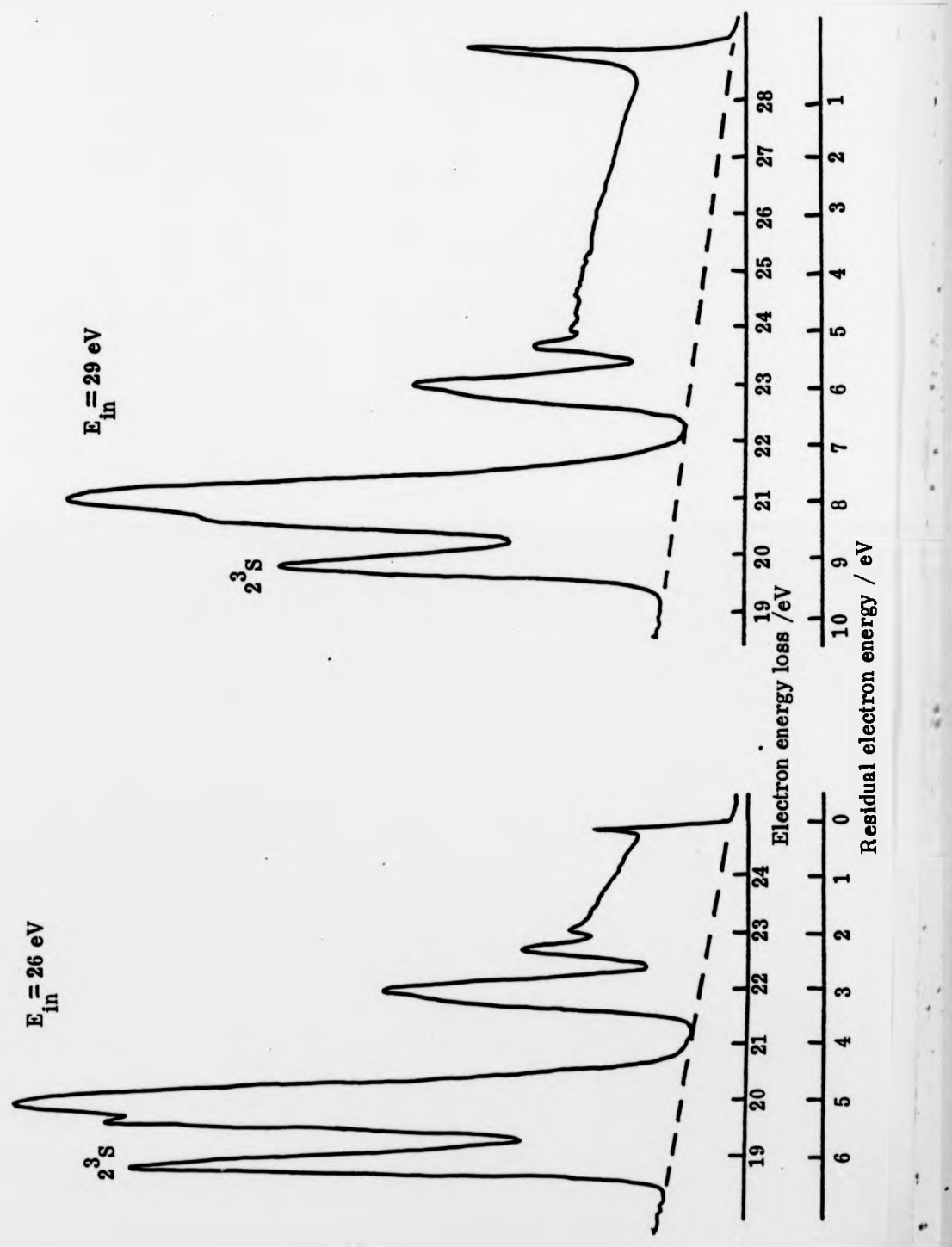

FIG. 17d

Fixed Incident Energy Spectrum of Helium

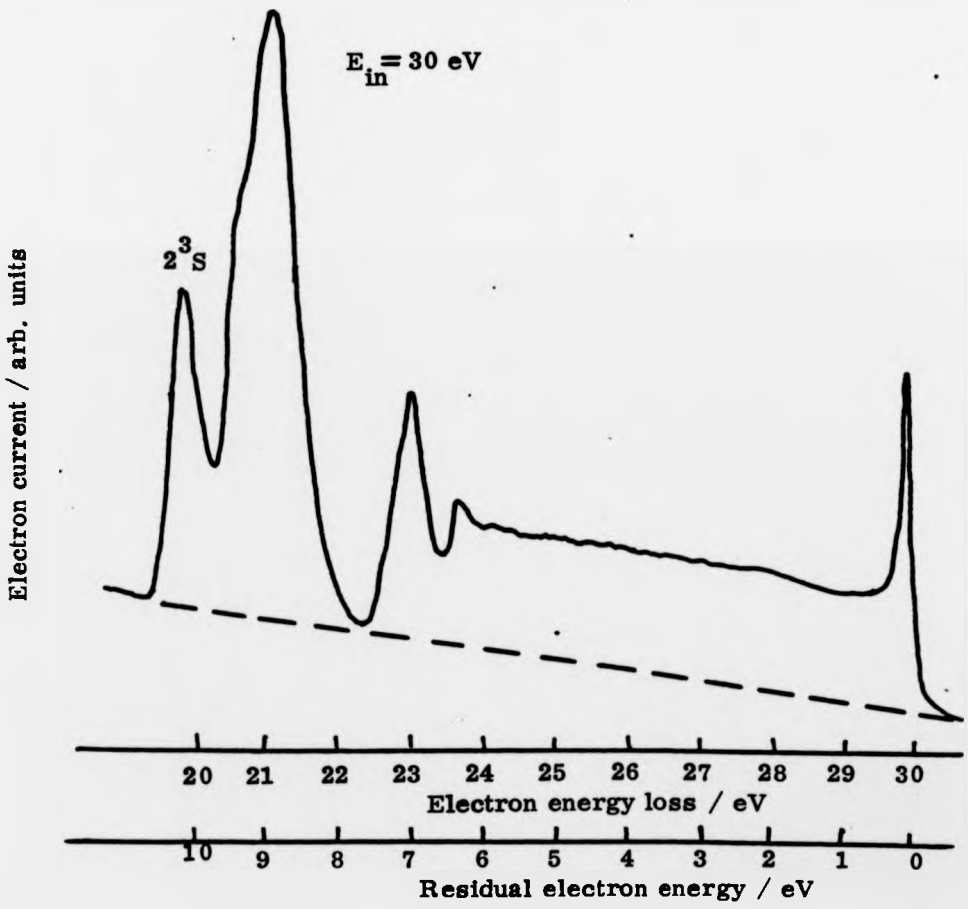

FIG. 17e

Fixed Incident Energy Spectrum of Helium

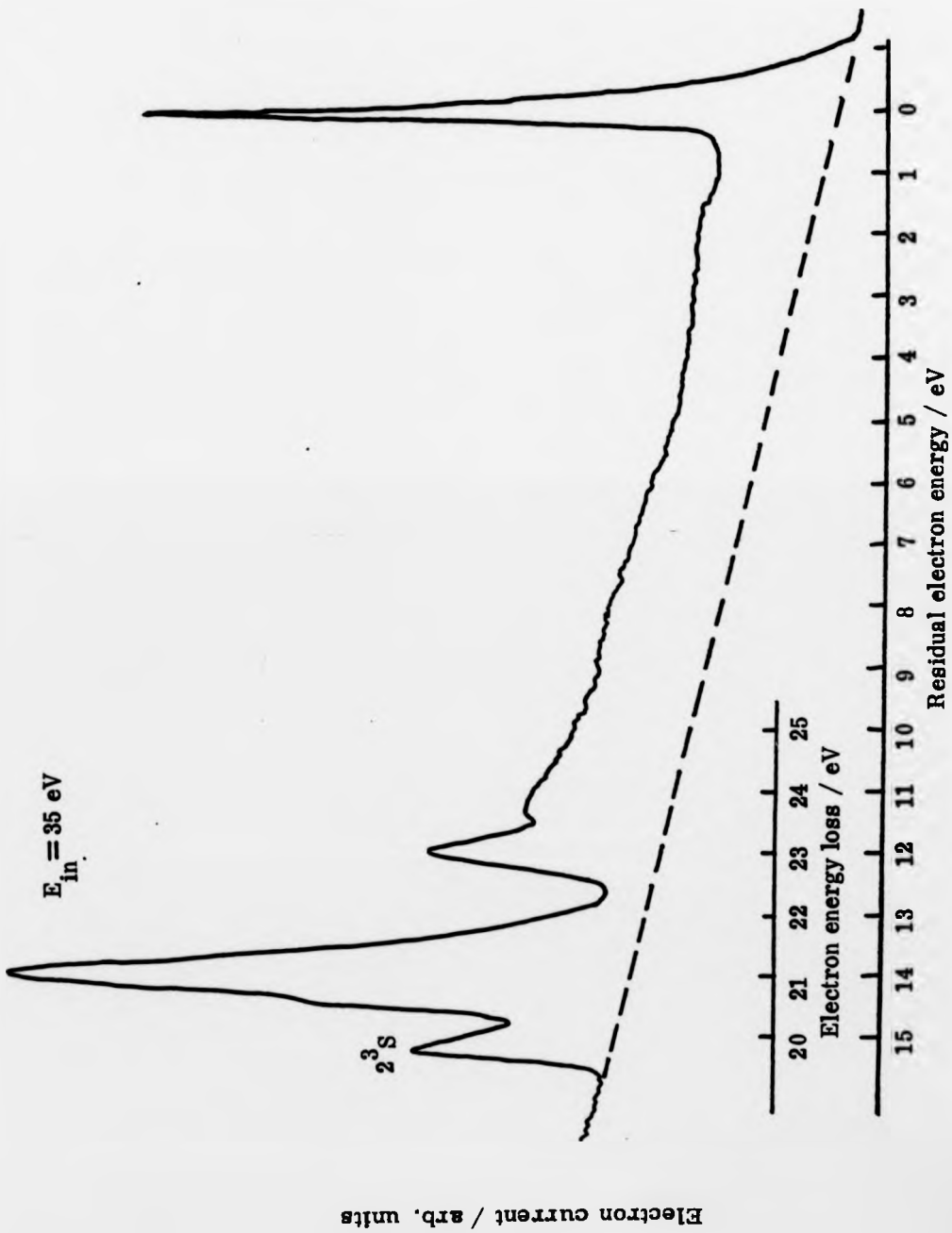

FIG. 18

Electron Transmission Spectrum of Helium

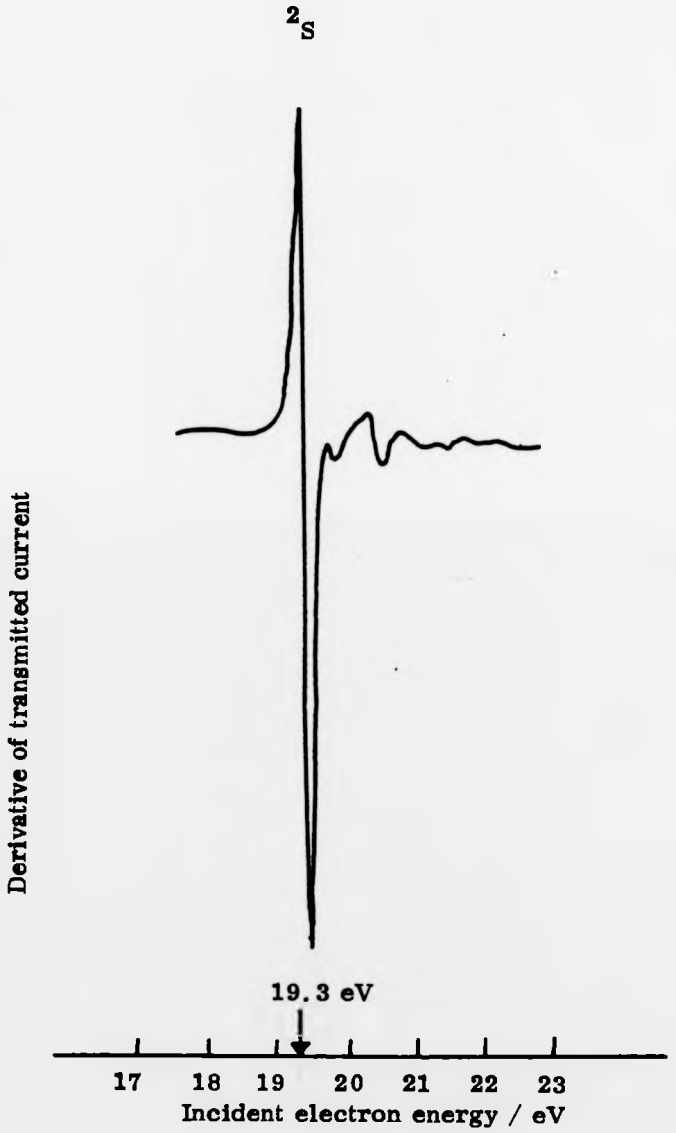

The ionisation threshold energy is indicated. A cusp, previously reported in another trapped electron experiment,[107] appears in the scattered electron intensity at the ionisation threshold. The physical reason for the cusp is the formation of states with two excited and strongly correlated electrons.[128] The functional dependence of the trapped electron signal in this region is of interest. The energy dependence of the cross-section for single ionisation of neutral atoms by electrons at near threshold energies can be expressed in the form

$$\sigma_{tot}^{ion} \propto (E_{in}-IP)^{n}$$

A threshold value of 1.127 for the exponent n has been obtained by several workers[129][130][131]; consistent experimental estimates have also been reported.[132][133] The signal in Fig.19 at any point above the ionisation threshold is proportional to a partial ionisation cross-section, as only electrons having a specific energy (within $e\Delta W$) are detected. Assuming a flat energy distribution function for the post-collision electrons (see Section (c)).

$$\sigma_{par}^{ion} \propto \frac{e\Delta W}{(E_{in}-IP)}\,\sigma_{tot}^{ion}$$

Since $\sigma_{tot}^{ion} \propto (E_{in}-IP)^{n}$

it follows that $\sigma_{par}^{ion} \propto (E_{in}-IP)^{n-1}$

Our results are consistent with an exponent of 1.127 (Fig.19).

(b) Excitation Functions

These curves, of Fig.14, correspond to total (angle-integrated) cross-sections. In them the effects of

FIG. 19

Threshold Energy Loss Spectrum of Helium (mod. trap)

Residual electron energy $\simeq$ 0.05 eV

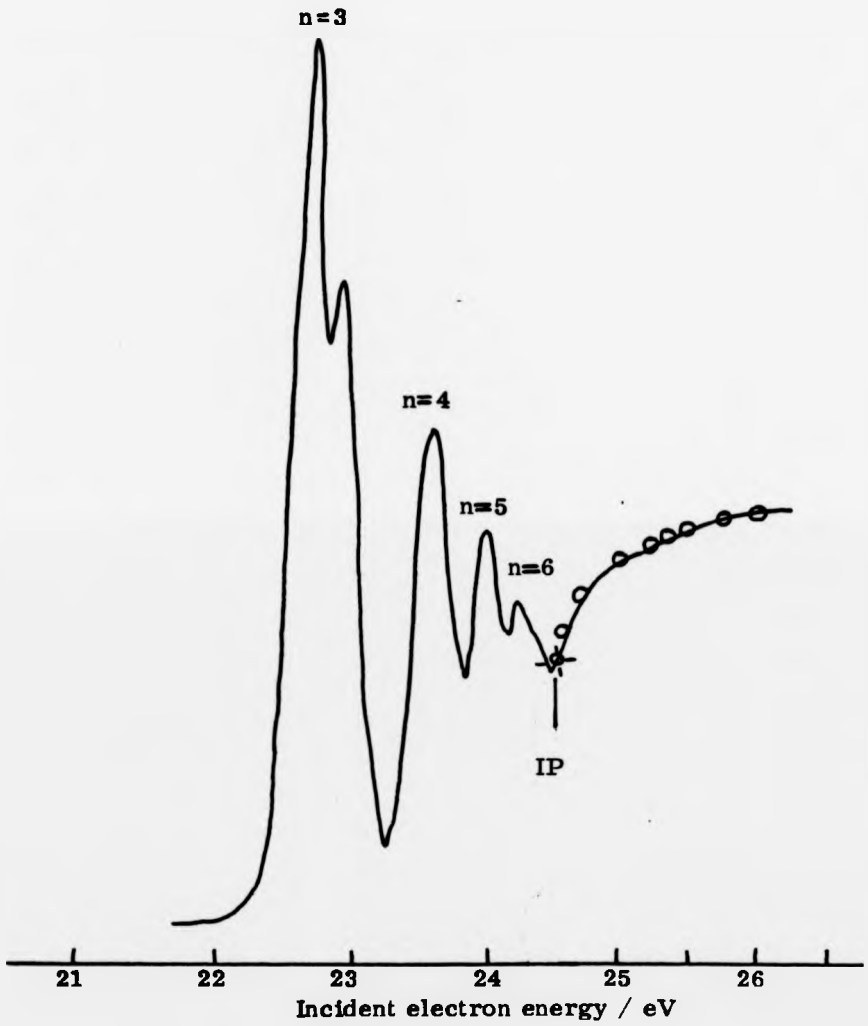

$$\sigma^{ion}_{par} \propto (E_{in} - IP)^{0.127}$$

(matched to experimental curve where indicated -'-')

resonance excitation more usually explored in differential scattering cross-sections are quite visible. In particular, excitation of the 2^3S state is enhanced through broad shape resonances, ^2P at 20.32 eV, ^2D at 20.96 eV and ^2S at around 22.5 eV, (features A, C and F respectively of Fig.14). As indicated in Table 6, these are known features of the 2^3S excitation function. Structures due to a group of resonances (S, P and D) associated with the n = 3 electronic states and lying below the 3^3S threshold are visible in our n = 2 excitation functions. Fig.14 shows nicely how a single resonance can enhance the excitation of a number of different states. Also, resonance structure is marked in the excitation of the 3^3S state between 22.8-23.6 eV. This agrees with the experimental results of Heddle et al.,[125] obtained by monitoring the optical decay of the 3^3S state to the 2^3P state, and also with the differential cross-section measurements of Pichou et al.[126] All of these resonances contribute to the double modulated spectra of Fig.16. There remains, in several of the excitation functions, a weak, broad feature centered about 22 eV energy. With the present instrument we cannot definitively assign this, but point out that Burke et al.[134] have, in a theoretical paper, positioned a ^2F shape resonance, width 1 eV, at around 22 eV.

It is important that these excitation functions be put on an absolute scale, and this we have attempted to do using a procedure which involves normalisation of the 2^3S excitation cross-section against a known ionisation cross-section. This procedure, described in detail in Section 5.2.2(c), was used to calibrate the cross-section axis of Fig.14. In our

instrument, the 2^3S excitation function is well resolved from other processes even at moderately large well depths. This is demonstrated in Fig.20 in which the FWHM of the apparatus function is plotted against increasing well depth and also shown in relation to the spacing between adjacent electronic energy levels. From this figure and from energy loss spectra, estimated errors in the other excitation functions can be derived. These errors are small for the 2^1S, 2^3P and 2^1P states (< 10%). The 3^3S excitation function will contain a substantial contribution from the 3^1S state (> 25%) and the 4^3S excitation function will include contributions from the other n = 4 states.

To demonstrate the internal consistency of our device, cross-sections estimated from energy loss spectra are compared with those obtained in well-depth scans in Fig.21.

(c) Fixed Incident Energy

As far as we are aware no one else has yet operated the electron trap in the fixed incident energy mode to give, directly, total inelastic cross-sections.

Consider the spectra in Fig.17. For energy losses below 24.59 eV, the ionisation threshold of helium, discrete states are excited. At high energies, ionisation takes place leaving the scattered electrons with a continuum of energies between zero and $(E_{in}-IP)$. Thus the collision region contains packets of electrons which can be sampled by varying W while maintaining $(V_a + W)$ constant. This is indicated schematically in Fig.22.

All of our spectra where E_{in} > IP show a sharp spike corresponding to a residual energy of ≈ 0eV (i.e. at W ≈ 0V).

FIG. 20

FWHM of Apparatus Function

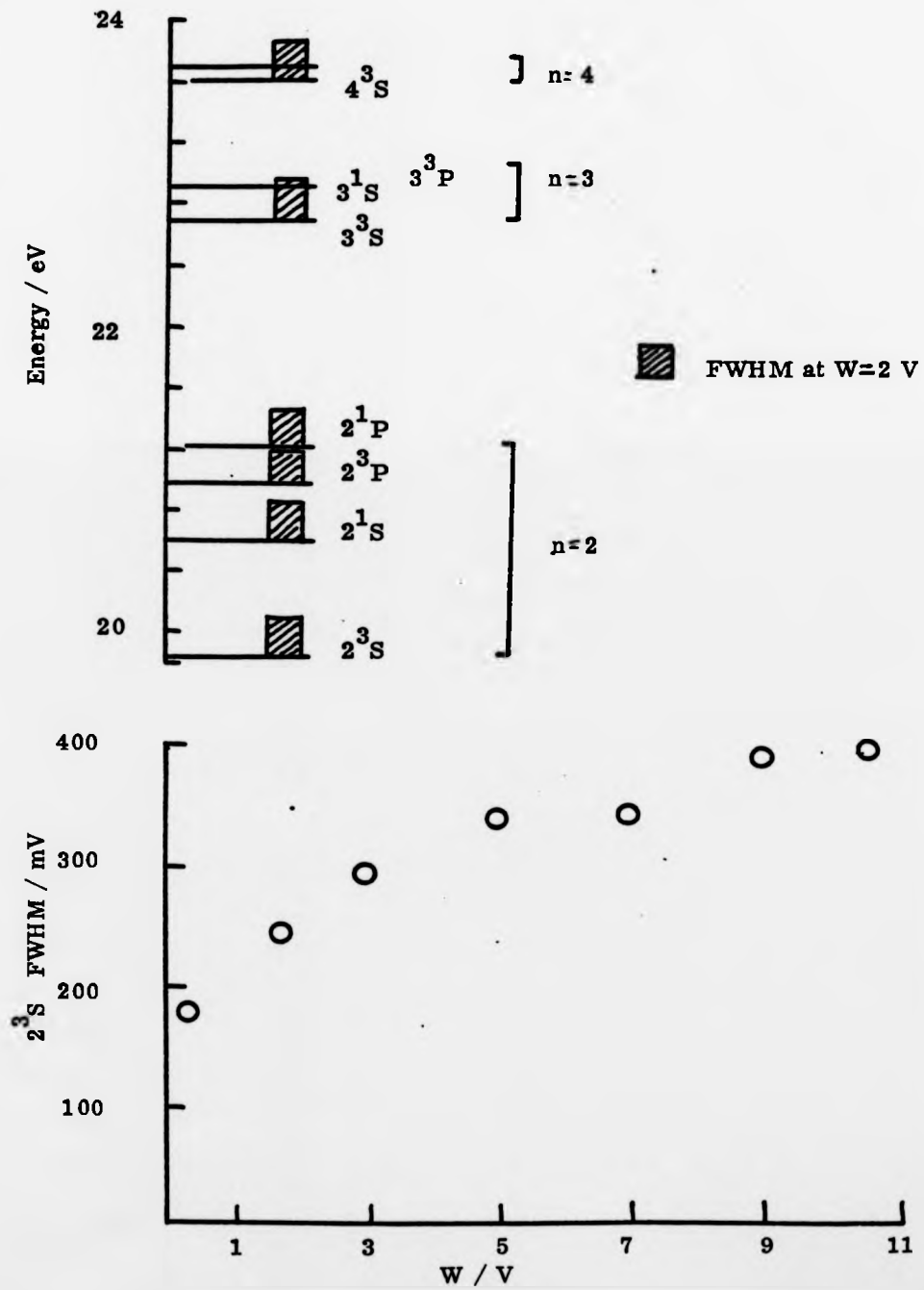

FIG. 21

Electron Impact Excitation Functions of Helium
Cross Sections Derived from Energy Loss Spectra ○ ● □

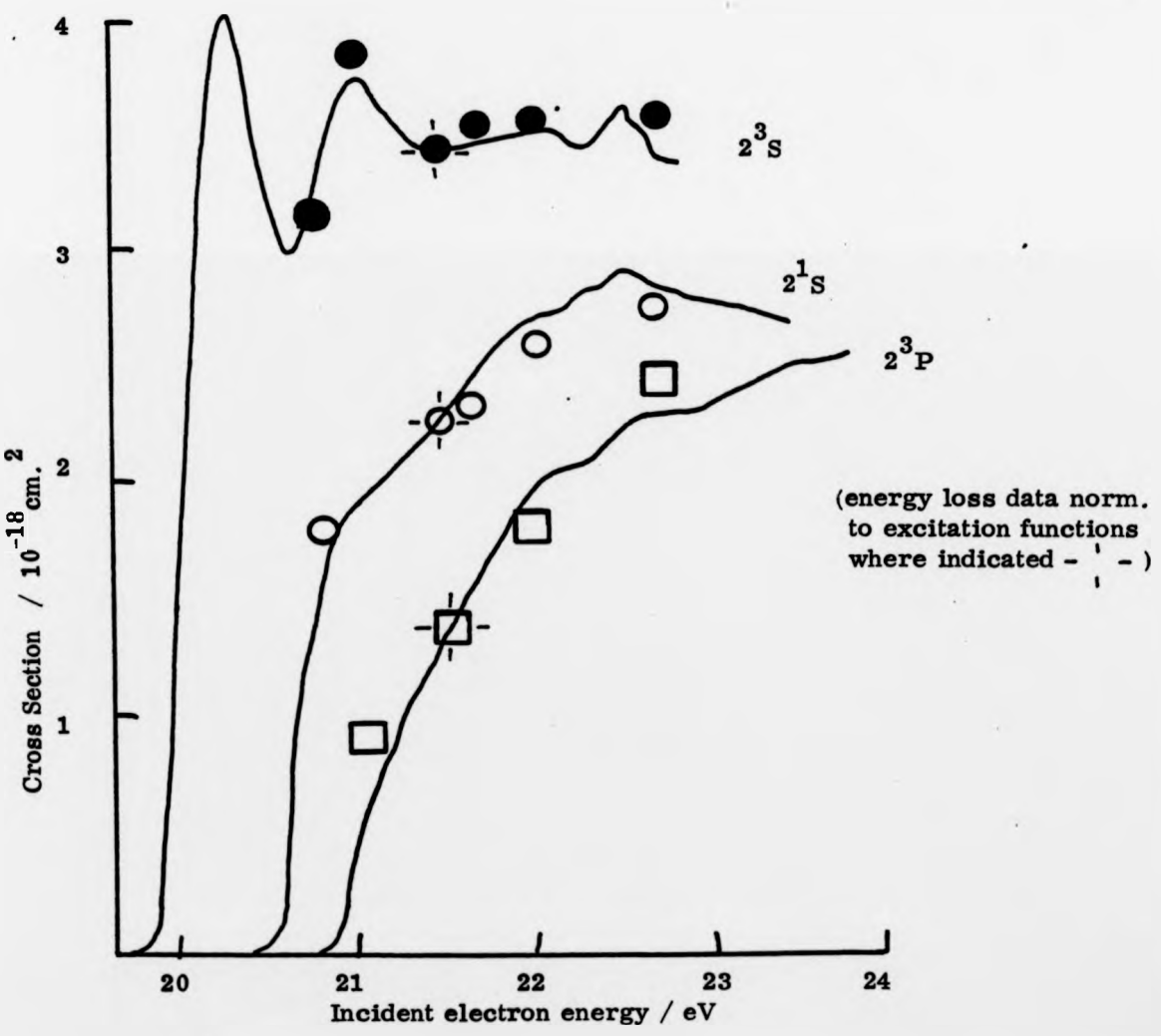

FIG. 22

Schematic Representation of Residual Electron Energy Strata Within the Electron Trap

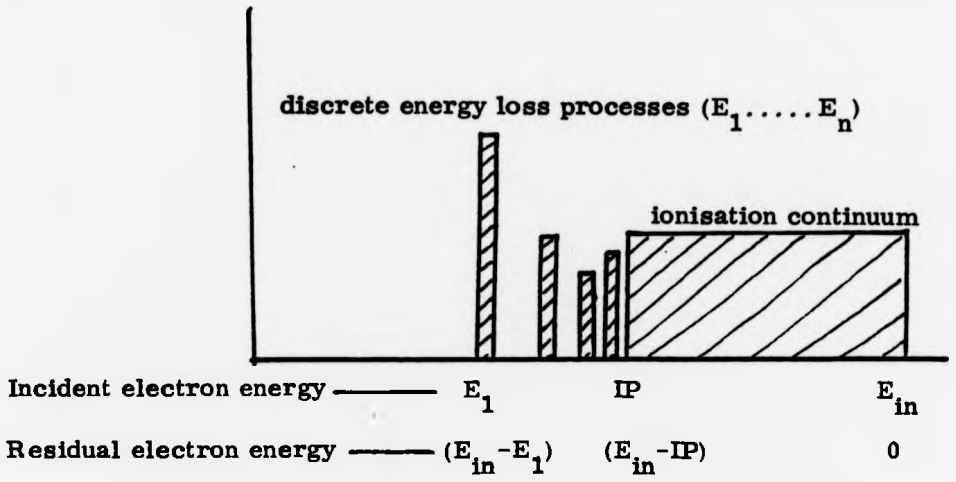

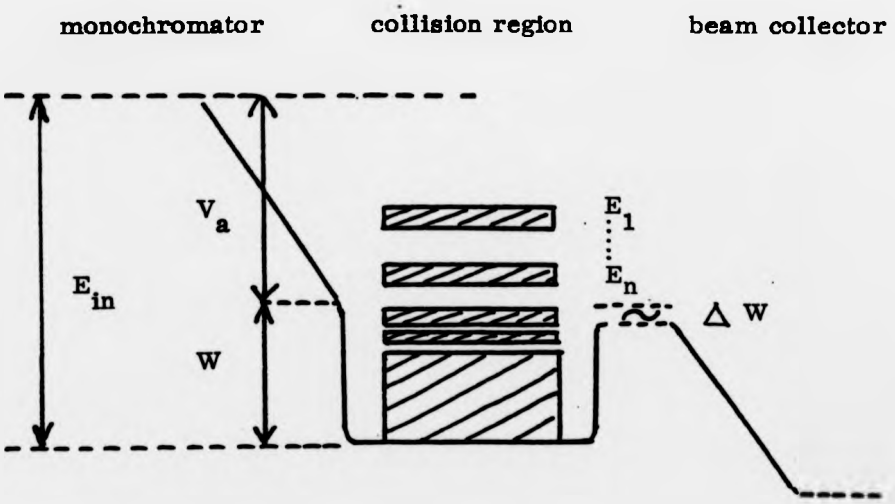

The magnitude of this feature is roughly proportional to the total ionisation cross-section. We believe this spike to arise from electrons in the ionisation continuum, for the following reasons. In the trap, electrons with $E_R > eW$ may be trapped if their axial velocity is insufficient to escape the potential well (Chapter 3). They will only be detected in the modulated trap, however, if they contribute to the in-phase signal which requires that they be scattered through some critical angle between θ_c and θ_c' ($\theta_c < \theta_c'$) such that

$$\cos\theta_c = \left[\frac{W}{E_R}\right]^{\frac{1}{2}} \text{ and } \cos\theta_c' = \left[\frac{W-\Delta W}{E_R}\right]^{\frac{1}{2}}$$

Assuming isotropic scattering, this yields a critical solid angle Ω where

$$\Omega = 2\pi \int_{\theta_c}^{\theta_c'} \sin\theta_c d\theta_c$$

There will be a contribution (S) to the signal from "high energy" trapped electrons which will be proportional to both this Ω and σ_{tot}^{ion}.

i.e.
$$S \propto \sigma_{tot}^{ion} \int_{\theta_c}^{\theta_c'} \sin\theta_c d\theta_c$$

$$\propto \sigma_{tot}^{ion} [\cos\theta_c - \cos\theta_c']$$

$$\propto \frac{\sigma_{tot}^{ion}}{E_R^{\frac{1}{2}}} [W^{\frac{1}{2}} - (W-\Delta W)^{\frac{1}{2}}]$$

S is inversely proportional to $E_R^{\frac{1}{2}}$ and directly proportional to $[W^{\frac{1}{2}} - (W-\Delta W)^{\frac{1}{2}}]$, a term which increases as W decreases. The S

function is plotted in Fig.23 for two incident energies, showing shapes which match those of our experimental curves. In brief, at low E_R (< 0.4 eV) and as W tends to zero, the collected signal rises due to the detection of electrons in the continuum which have been scattered through a 'critical' angle. The shallow minimum preceding the spike in some spectra is instrumental and can be removed by careful tuning.

We can allow for these artefacts by utilising the symmetry properties of the energy distribution of the post-collision electrons in the ionising region.

$$e + H_e \rightarrow H_e^+ + 2e$$

For every scattered electron of energy E_R there is another of energy $(E_{in}\text{-IP}-E_R)$, so that the electron energy distribution is symmetrical about a residual energy $(E_{in}\text{-IP})/2$. Further, at any E_R the height of the signal is proportional to the partial ionisation cross-section σ_{par}^{ion} while the signal integrated over the residual energy range $0\text{-}(E_{in}\text{-IP})$ is proportional to the total ionisation cross-section. We can extract from the data of Fig.17 the scattered electron signal in the ionisation region, at a number of different incident energies. To do this we measure the height of the signal above the baseline and assume symmetry about $E_R = (E_{in}\text{-IP})/2$; this copes with the threshold spike. The resultant curves are displayed in Fig.24. The errors involved in estimating these signals are <15% for E_{in} < 30 eV but are >30% for E_{in} = 35 eV, due mainly to uncertainties in locating the baseline.

The plots of Fig.24 show that for incident electron energies up to 30 eV, the scattered electrons have an energy

FIG. 23

Comparison of Computed and Experimental Curves at Low Residual Electron Energies in Fixed E_{in} Spectra

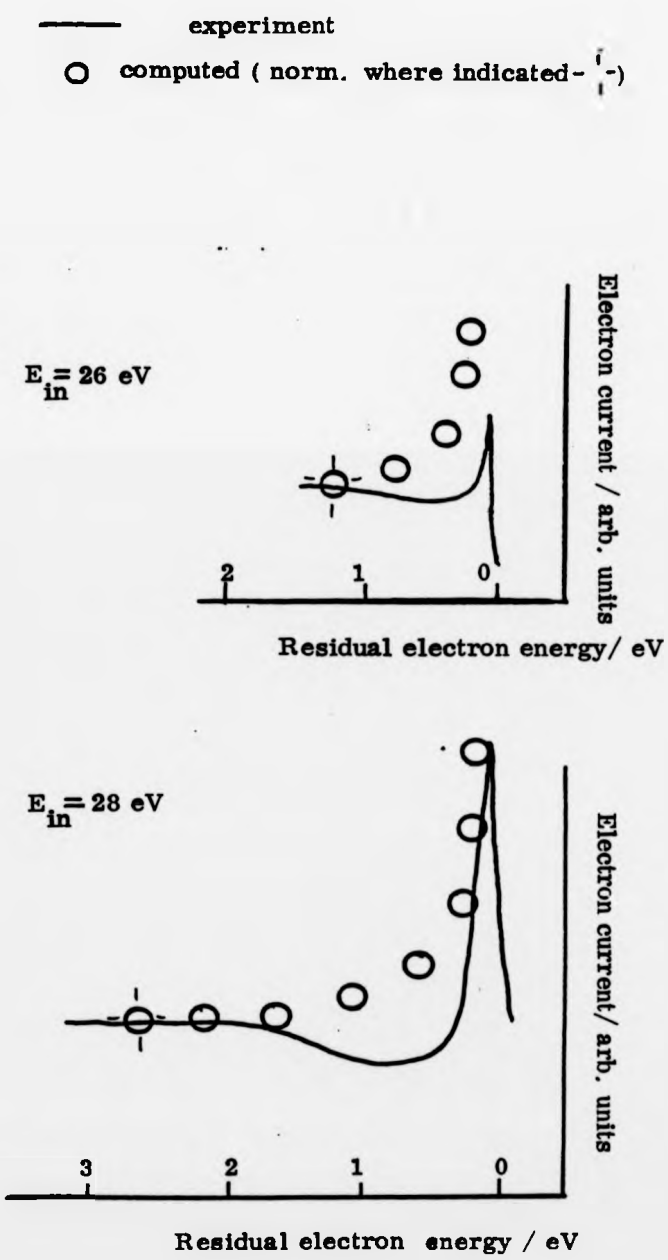

FIG. 24a

Signal Above IP from Fixed E_{in} Spectra

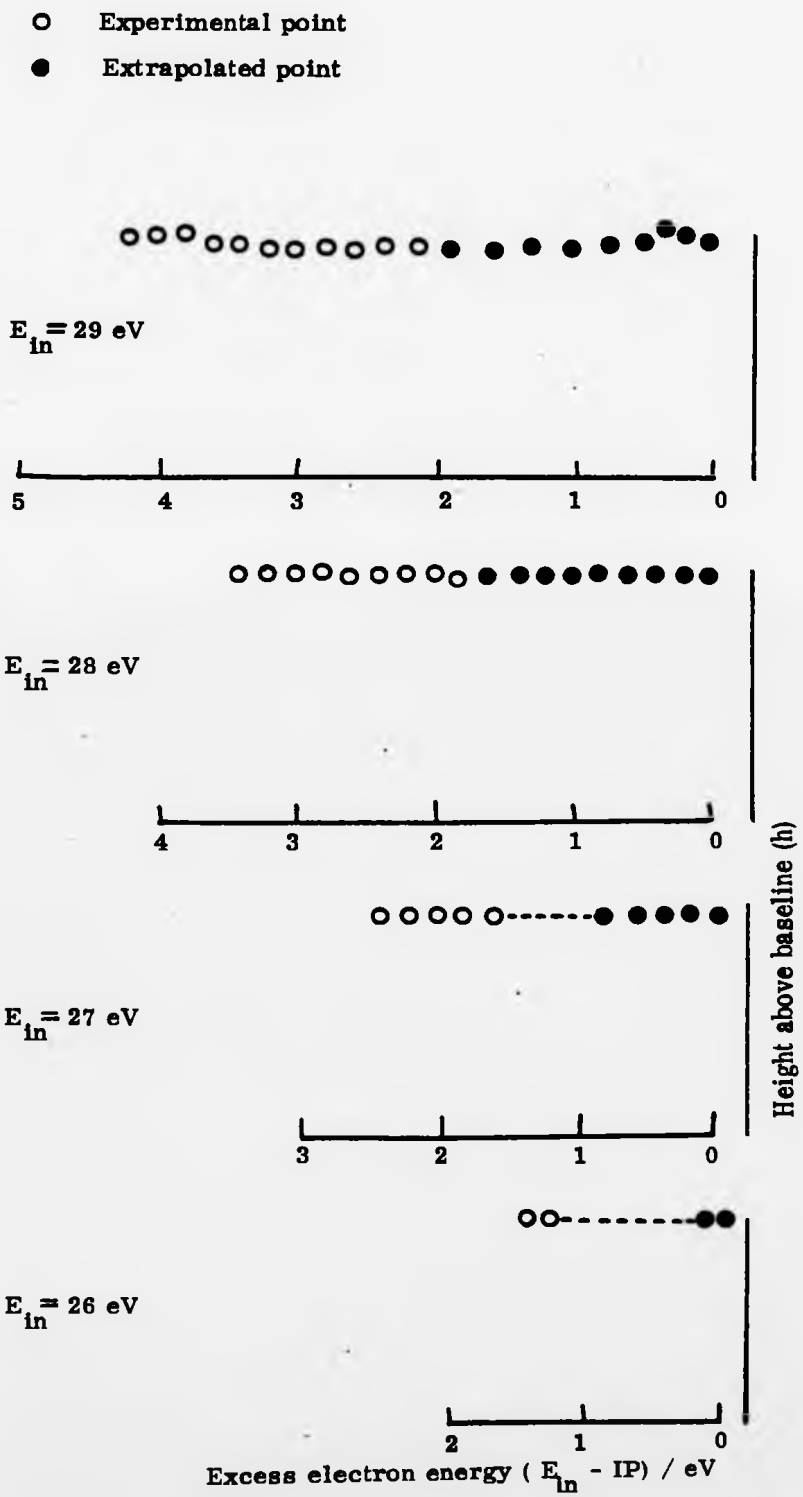

FIG. 24b

Signal Above IP from Fixed E_{in} Spectra

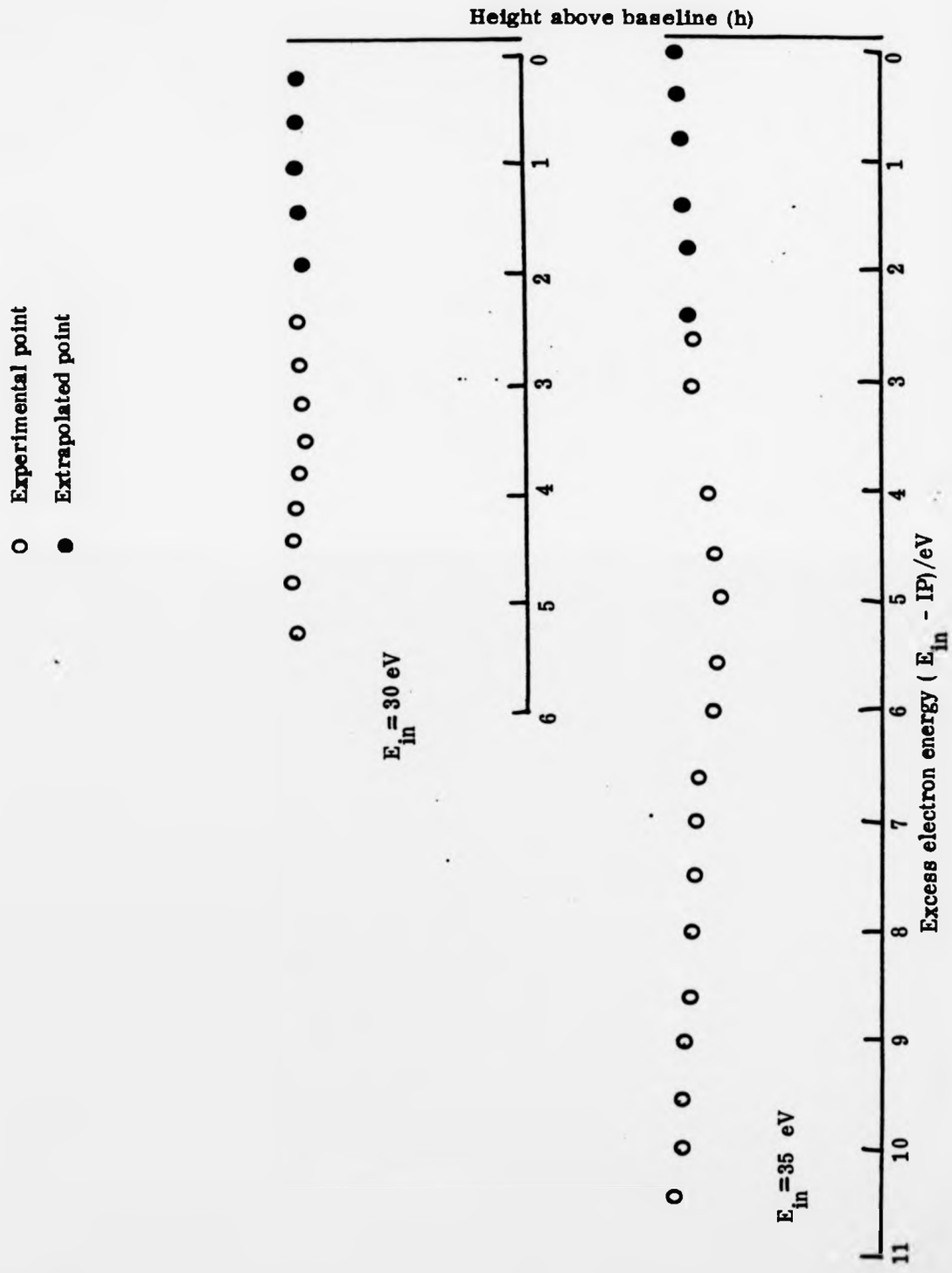

distribution $P_E(E_R)$, which is uniform to within about 10%. Even at incident energies as high as 30 eV (i.e. 5.4 eV above ionisation threshold) the distribution shows only a slight curvature. This is in marked disagreement with data of Pichou et al.[135] which show a uniform distribution only to about 3.6 eV above threshold. At 30.6 eV incident energy their energy distribution function exhibits a pronounced increase, almost 100%, in P (0 eV) and P (6 eV) over P (3 eV). On the other hand, Ehrhardt,[136] in a coincidence experiment at incident energies between 30 eV and 80 eV commented that for incident electron energies around 30 eV and lower, $P_E(E_R)$ is uniform. Theoretically it is expected that $P_E(E_R)$ will be uniform near threshold.[129][130][131]

Recently, Klar[137] has predicted that the effect of screening may lead to an unexpectedly large energy range, over which the threshold ionisation cross-section formula

$$\sigma_{tot}^{ion} \propto (E_{in}\text{-IP})^{1.127}$$

holds. He also predicts a uniform energy distribution $P_E(E_R)$ over the energy range for which the 1.127 power law is valid.

For a uniform $P_E(E_R)$

$$\sigma_{par}^{ion} \propto \frac{\sigma_{tot}^{ion}}{(E_{in}\text{-IP})}$$

h, the height of our signal is proportional to σ_{par}^{ion}, so that

$$h \propto \frac{\sigma_{tot}^{ion}}{(E_{in}\text{-IP})}$$

If we take the total ionisation cross-sections of Rapp and Englander-Golden,[138] we find that this linear relationship does in fact hold (Fig.25). Also, in the present case the total

FIG. 2 5

Plot of h vs. $\sigma_{tot}^{ion}/(E_{in} - IP)$

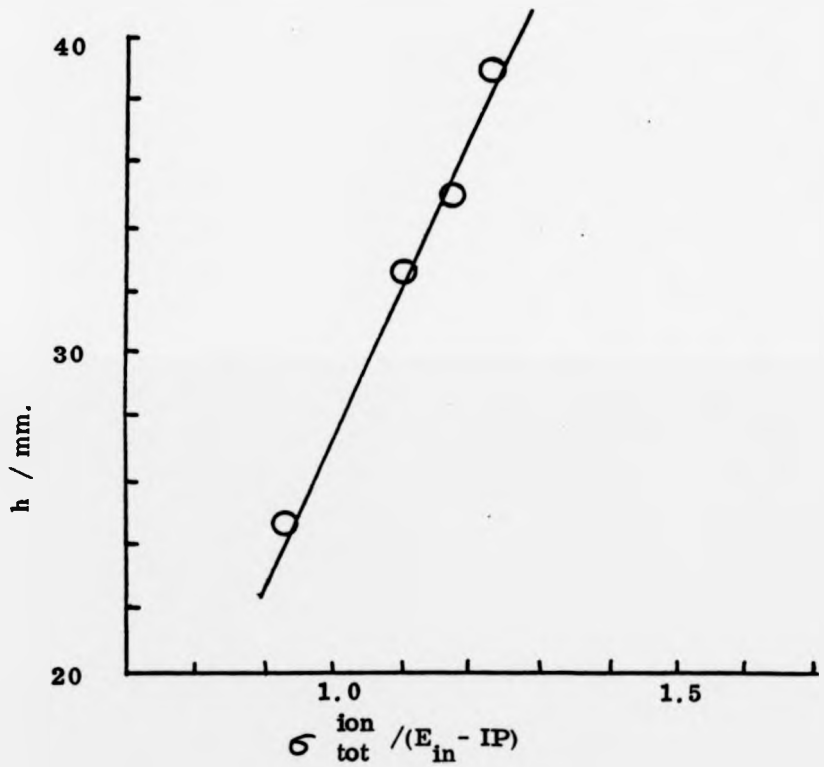

ionisation cross-section at any incident energy is proportional to the area under the appropriate curve of Fig.17. We have normalised our data to the total ionisation cross-section of Rapp and Englander-Golden at 28 eV to get absolute ionisation cross-sections. The results are shown in Fig.26. Again our total ionisation cross-sections disagree markedly with those of Pichou et al.[135] The 1.127 power law appears to hold for a large energy range.

We can use these ionisation data to place electronic excitation cross-sections on an absolute basis. This has been done for excitation to the 2^3S state at a number of E_{in} (chosen where the 2^3S peak is well resolved). We equate the measured area of the 2^3S peak to a calibration value derived from our ionisation data thus yielding absolute values for the 2^3S excitation cross-sections at a series of energies. It is these 2^3S data which we employed to calibrate the cross-section axis of Fig.14. We estimate that the maximum in the 2^3S cross-section at about 20.32 eV has a magnitude $(4.0 \pm 0.8) \times 10^{-18}$ cm^2. This is compared with other measured and theoretically derived values in Table 7. The theoretical values are sensitive to the width of the He^- ^2S resonance at 19.34 eV. There is some evidence[147] that this width may be narrower than assumed in these calculations and if this is the case, then the magnitude of the calculated values could be reduced to around 4×10^{-18} cm^2.[146]

It is, of course, important in presenting absolute cross-sections to be sure that the signals recorded arise from the processes to which they have been ascribed. As discussed in Chapter 3, electrons which are scattered elastically through

FIG. 2 6

Ionisation Cross Section of Helium

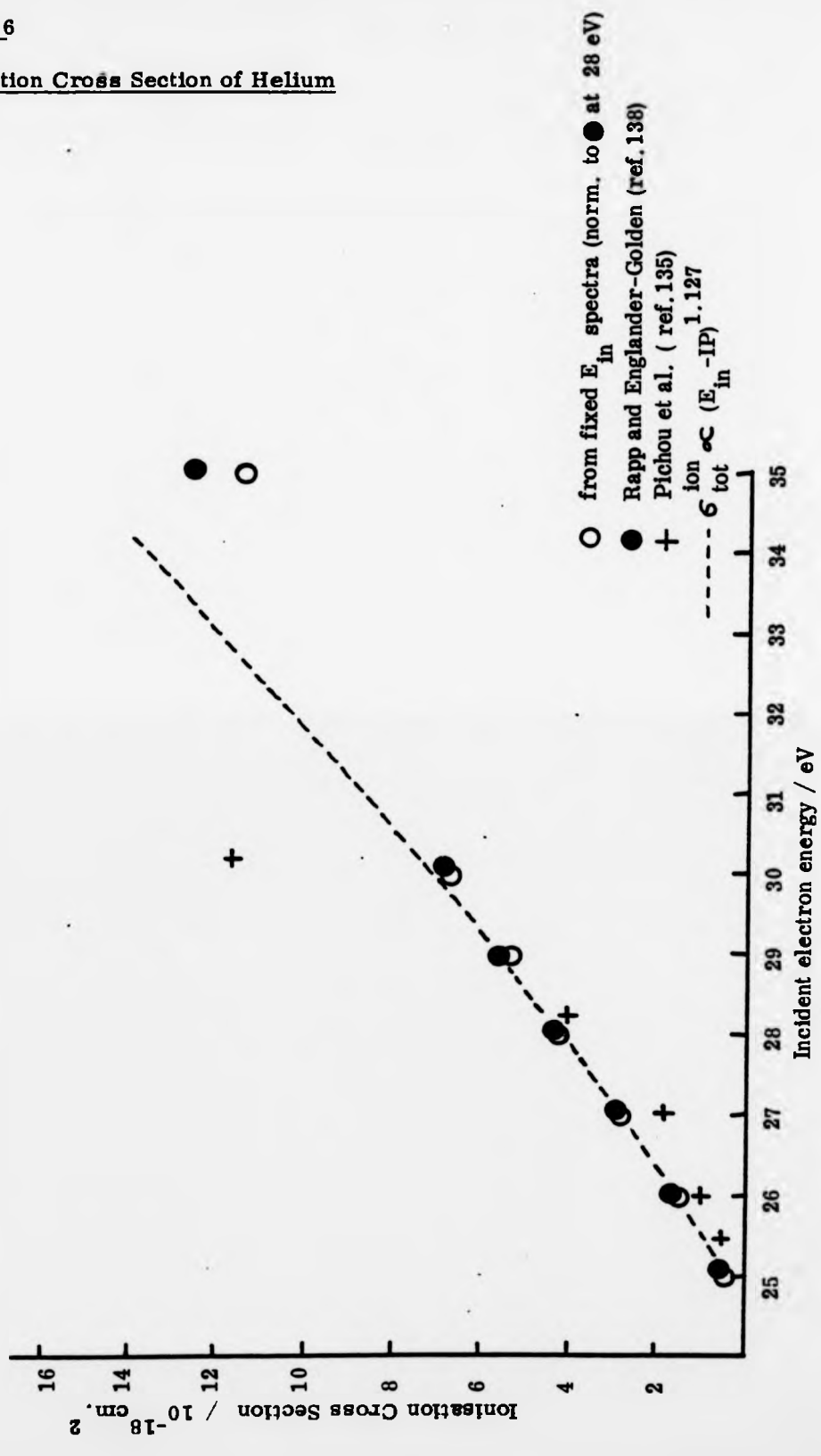

TABLE 7

Magnitude of the He 2^3S Cross-Section (0.5 eV above threshold)

Experiment	σ / 10^{-18} cm^2
Johnston and Burrow[139]	6 ± .6
Brongersma et al.[61]	4 ± 1.2
Fleming and Higginson[140]	2.6 ± .4
Holt and Krotkov[141]	3.0 ± .7
Borst[142]	4 ± 1.3
Schulz and Fox[143]	4 ± 1.2
Maier-Leibnitz[144]	5
Present Results	4.0 ± .8
Theory	
Oberoi and Nesbet[123]	5.6 (4)*
Berrington et al.[145]	5.6 (4)*

* ^2S width assumed to be 8 meV[145]

a large angle may find themselves with insufficient axial velocity to escape from the collision region and so will be trapped perhaps sufficiently long to make a subsequent inelastic collision, i.e. there is a mechanism for increasing the electron path length. We believe this to be negligible in the present system over the ranges of V_a and W encountered in the helium work. Firstly, this effect should be more important at large W. In fact, we observe no anomalous increases in signal at large W (> 4V); witness the good agreement of our 2^3S and total excitation functions with theory and experiment (Figs.28, 32). Also we have simulated the performance of the trap in a Monte-Carlo type computer calculation. A program listing and flow chart are contained in Appendix III. Typical results are shown in Table 8. These demonstrate that under the conditions of the present work, in helium, elastically trapped electrons in general are reoriented so as to escape the trap before making a second inelastic collision and also before diffusing to the scattered collector. This latter observation means that elastically scattered electrons cannot contribute to the scattered electron signal. Experimentally, this is confirmed by the lack of signal at deep W for incident energies below the inelastic threshold, as shown in Fig.27.

All these considerations suggest that our 2^3S excitation functions are reliable and uncontaminated by other effects. They are presented along with others in Fig.28. In general shape, the agreement with other trap measurements and theory is good. As has been pointed out, the magnitude of the first maximum (4.0×10^{-18} cm^2) agrees with a number of other estimates, although not with a very recent one.[139] At 1.6 eV

TABLE 8

Computer Analysis of Electron Trap

RUN GKTRAP

Accelerating Voltage	19.5
Excitation Energy	19.8
Well-depth	2
Number of Electrons	.8E + 07
Pressure	.01
Incident Energy	21.5
Residual Energy	1.700001
Elastic X-Section	.299999E-19
Inelastic X-Section	.299999E-21
Inelastically scattered I1	20215
Inelastically scattered I2	2963
Straight thro Electrons	.711262E + 07
Elastically scattered	867169
BC after Collision	428434
Electrons stopped at Exit	7188
Elastically trapped	0
Total Beam Current	.754105E + 07
Backscattered Electrons	213930
Derived Elastic X-Section	.1114815E-19
Derived Inelastic X-Section I1	.2598810E-21
Derived Inelastic X-Section I1 + I2	.2979705E-21
SQR(W/E)	.304997

The derived inelastic cross-sections (I_1 and $I_1 + I_2$) reflect the increased path length effect. No electrons reach the collector via elastic scattering alone.

FIG. 27

Plot of Electron Current vs. W for Various V_a in Helium

above threshold our value of 3.4×10^{-18} cm^2 may be compared with the integral cross-section of Pichou et al.,[126] 3.22×10^{-18} cm^2 and the theoretical value of Berrington et al.,[145] 3.81×10^{-18} cm^2. Fig.29 summarises data for excitation of the 2^1S state. Here, there is little agreement about the shape of the function but the magnitude at 1.6 eV above threshold, 2.8×10^{-18} cm^2 can be compared to 2.54×10^{-18} cm^2 (Pichou et al.) and 3.45×10^{-18} cm^2 (Berrington et al.). The general shapes of the 2^3P and 2^1P excitation functions are in fair agreement with theory and the magnitudes also agree quite well with other estimates (Fig.30). There are fewer data with which to compare the 3^3S and 4^3S excitation functions in Fig.31. Chutjian and Thomas[148] estimate the 3^3S cross-section at 29.2 eV to be 3.8×10^{-19} cm^2. We are not aware of any near threshold measurements of the total 4^3S cross-section. Showalter et al.[149] estimate the cross-section at 60 eV to be 1.24×10^{-19} cm^2.

Finally, we present in Fig.32, total excitation cross-sections between 19.8-24 eV. These absolute data were obtained both from the total area under the subionisation energy region of the fixed incident energy spectra in Fig.17, and by summing the individual scanned well depth traces of Fig.14 (up to the 3^3S threshold). The total excitation cross-section of Hall,[150] normalised to ours at 20.32 eV, is shown along with estimated values from other sources.[151a][151b] Fig.33 compares the sum of our 2^3S and 2^1S excitation functions with the total metastable production measurements of Dowell[152] and Pichanick and Simpson.[153] The trapped electron curve obtained by summing the 2^3S and 2^1S cross-sections becomes bigger than the metastable curve as soon as the 2^1S state is excited. This is due to an

FIG. 28

2^3S Excitation Function of Helium

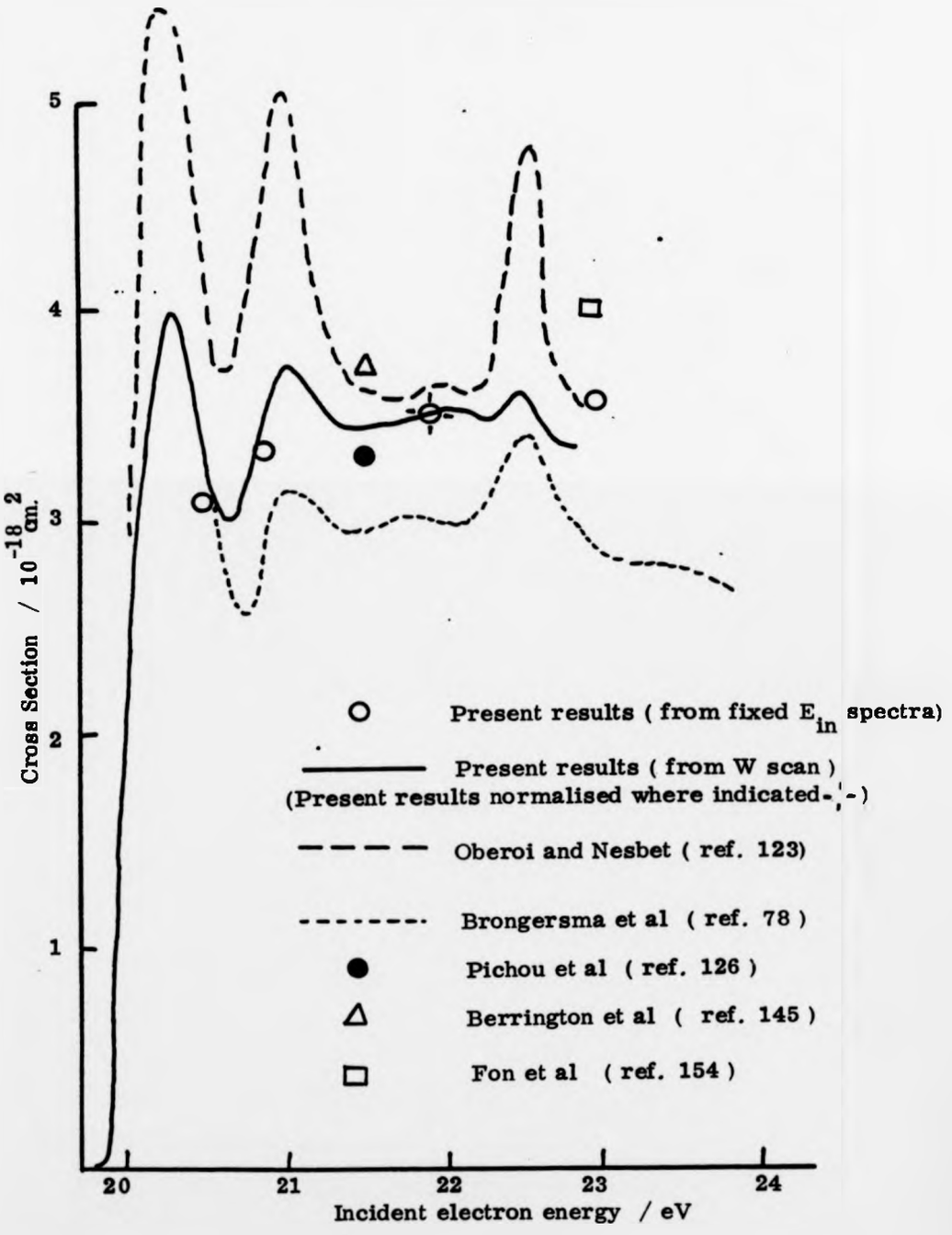

FIG. 29

2^1S Excitation Function of Helium

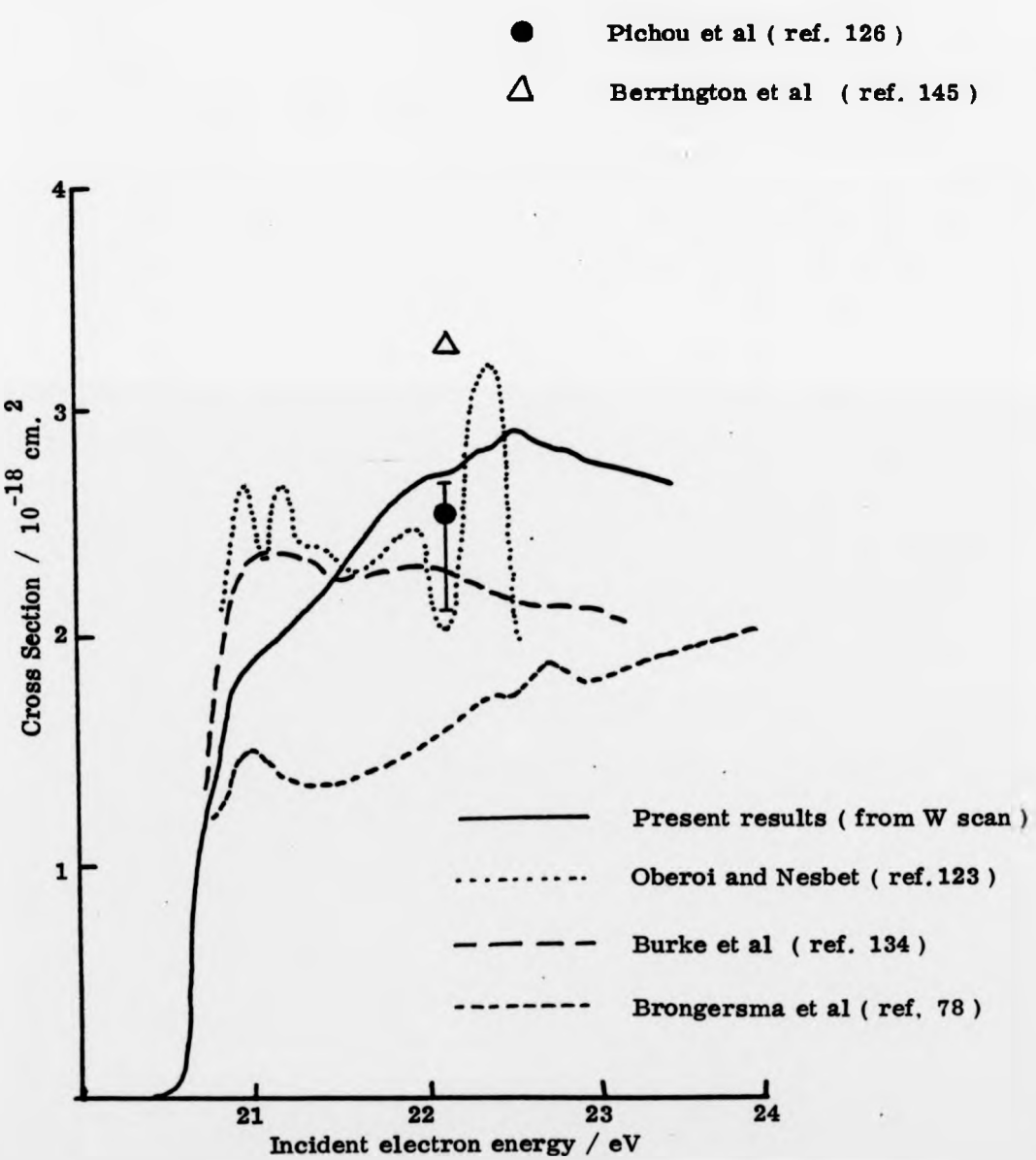

FIG. 30

2^3P and 2^1P Excitation Functions of Helium

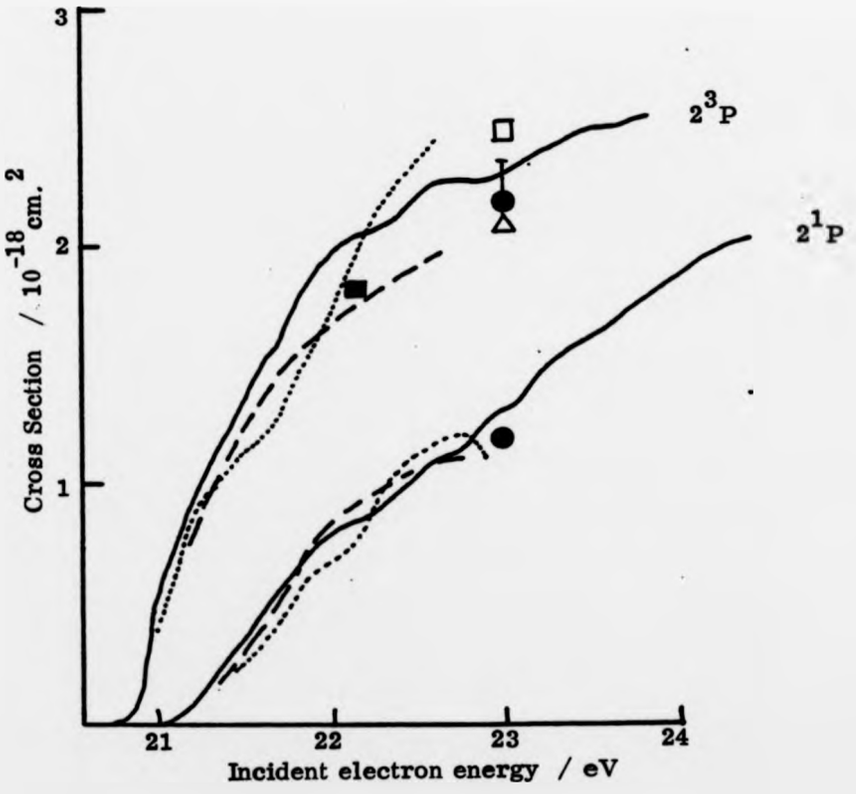

FIG. 31

3^3S and 4^3S Excitation Functions of Helium

3^3S — 3.8 10^{-19} cm.^{2} (29.2 eV) Chutjian and Thomas (ref. 148)

4^3S — 1.24 10^{-19} cm.^{2} (60 eV) Showalter et al (ref. 149)

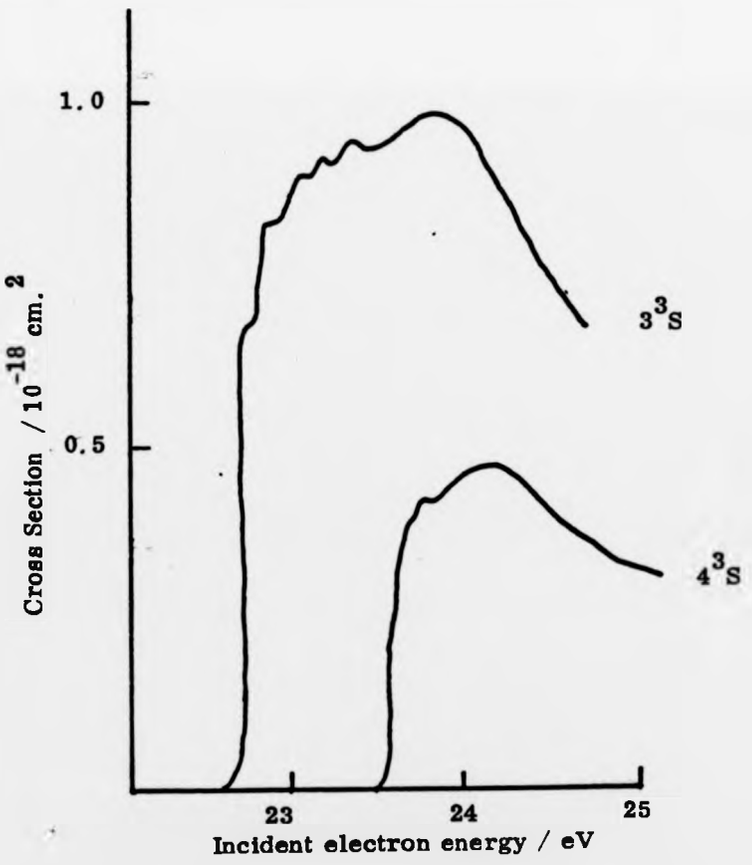

FIG. 32

Total Excitation Cross Section of Helium

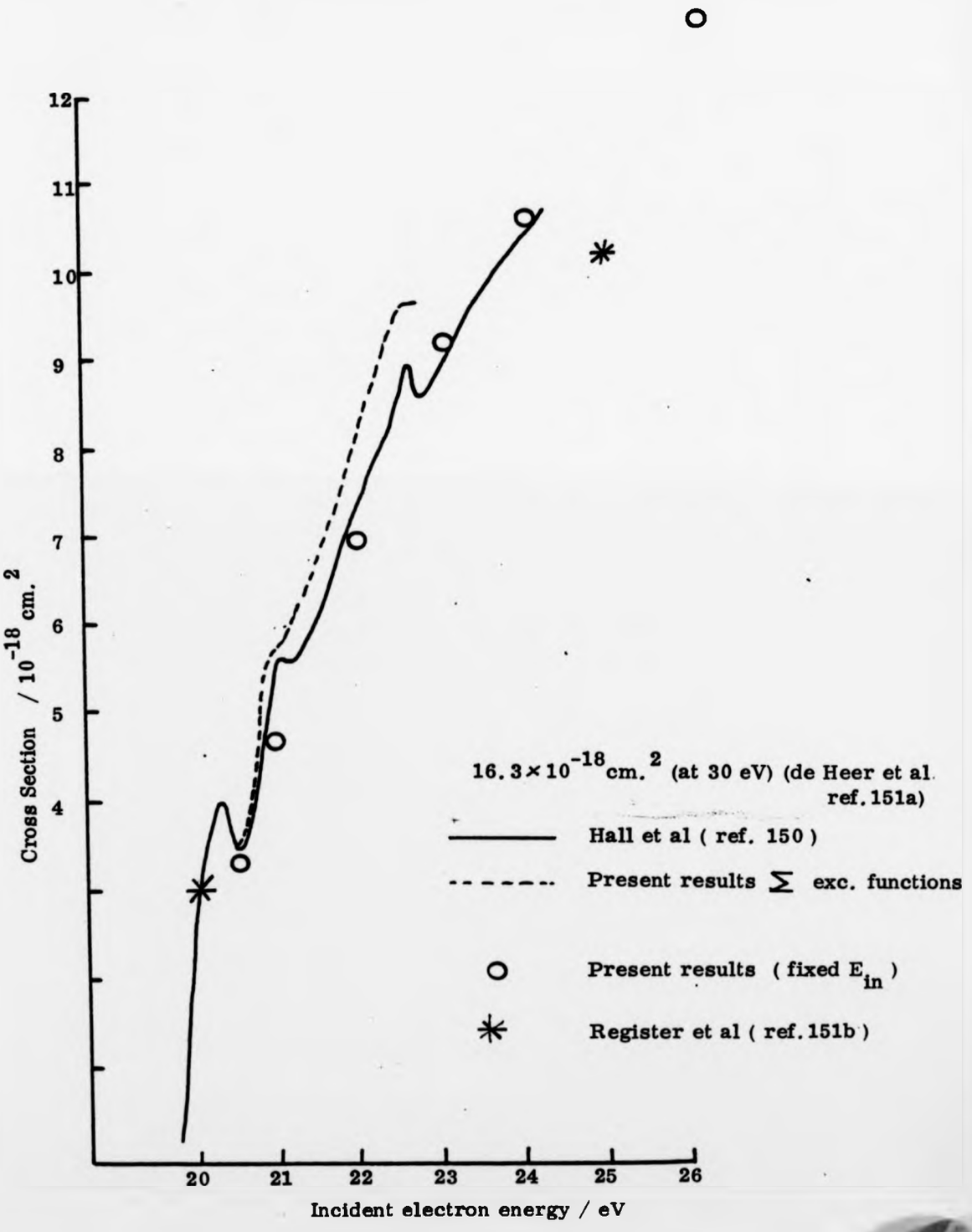

FIG. 33

Metastable Production Cross Sections of Helium

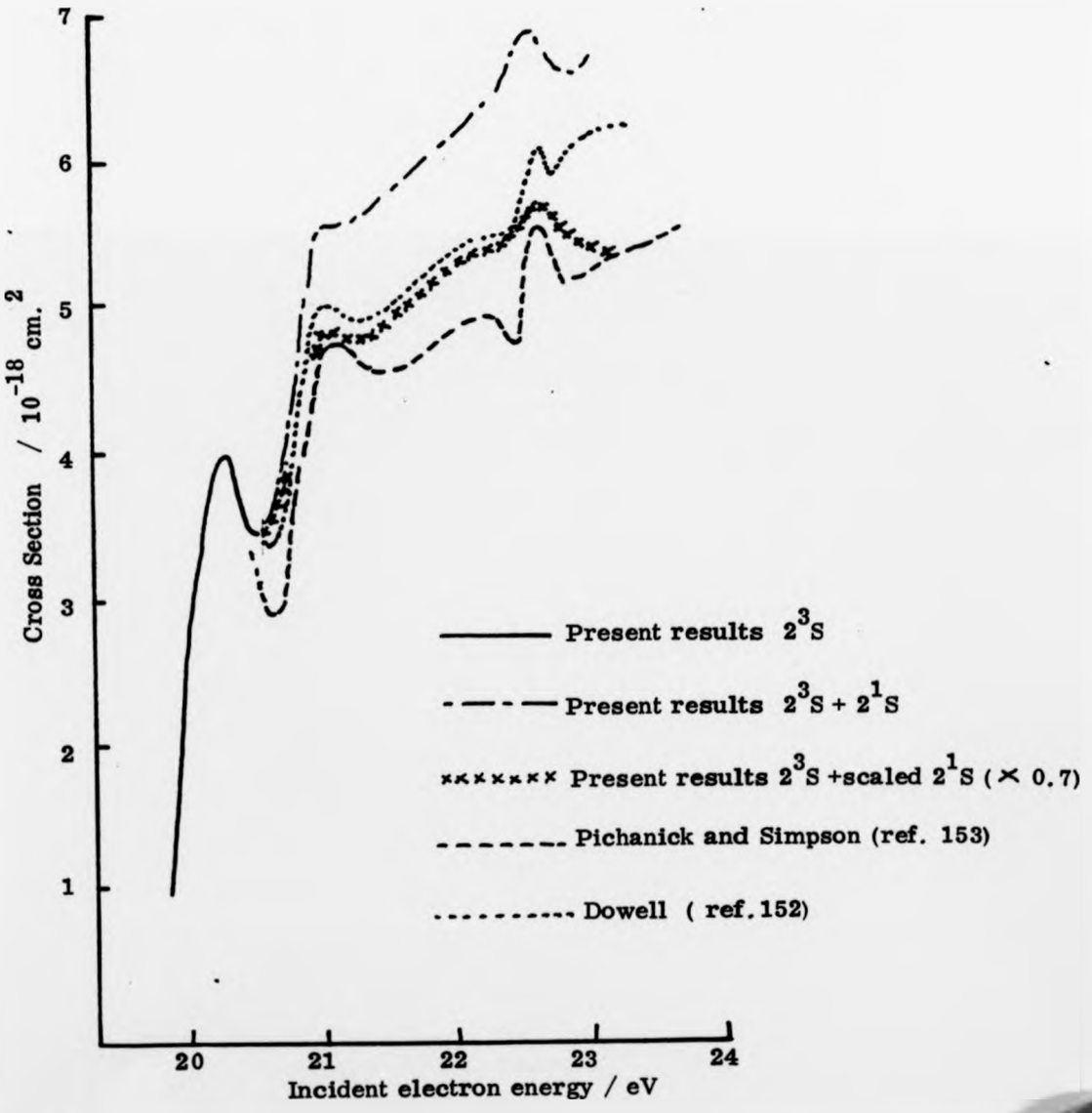

electron ejection efficiency difference between 2^3S and 2^1S metastable atoms. We can scale our 2^1S contribution appropriately to allow for this collection efficiency, yielding a curve which is in good agreement with the metastable experiment, the intensities being matched at 22.32 eV.

5.3.1 Nitrogen

Results

Energy loss spectra for N_2 are presented in Figs. 34 (d.c. trap) and 35 (a.c. (modulated) trap). The energy scale is calibrated using the spectroscopic values of the vibrational levels of the $\tilde{B}^3\pi_g$ excited state. Table 9 lists the energies of peaks from Figs. 34 and 35 for comparison with optical values.[155a,b]

The curves presented in Fig. 36 are scanned well depth traces of some excitation functions of N_2. Fig. 37 shows fixed incident energy spectra for E_{in} = 8.5 eV and 17 eV.

5.3.2 Discussion

(a) Energy Loss Spectra

The electron configuration of the ground electronic state of N_2 ($X^1\Sigma_u^+$) is

$$(\sigma_g 1s)^2(\sigma_u 1s)^2(\sigma_g 2s)^2(\sigma_u 2s)^2(\pi_u 2p)^4(\sigma_g 2p)^2$$

Spectra in Figs. 34 and 35 present an overview of threshold energy loss processes and consist of families of peaks corresponding to the vibrational levels of numerous electronically excited states. Below 11.87 eV most of the observed peaks are well separated and can be unambiguously assigned although the resolution compares unfavourably with that of other electron

TABLE 9

ENERGIES OF PEAKS IN THE TRAPPED ELECTRON SPECTRA OF NITROGEN/(eV)

State		Present Results (Figs.34 and 35)	Spectroscopic Values (refs. 151a, b)
$\tilde{B}^3\pi_g$	$\nu' = 0$	7.34	7.35
	1	7.56	7.56
	2	7.77	7.77
	3	7.96	7.97
	4	8.15	8.17
	5	8.37	8.37
	6	8.56	8.56
	7	8.75	8.75
	8	8.92	9.06
	9	9.05	9.12
$\tilde{C}^3\pi_u$	$\nu' = 0$	11.01	11.03
	1	11.26	11.28
$\tilde{E}^3\Sigma_g^+$	$\nu' = 0$	11.87	11.87
	1	12.14	12.14
$a''\ ^1\Sigma_g^+$		12.25	12.26

FIG. 34 a

Energy Loss Spectrum of Nitrogen (d.c. trap)

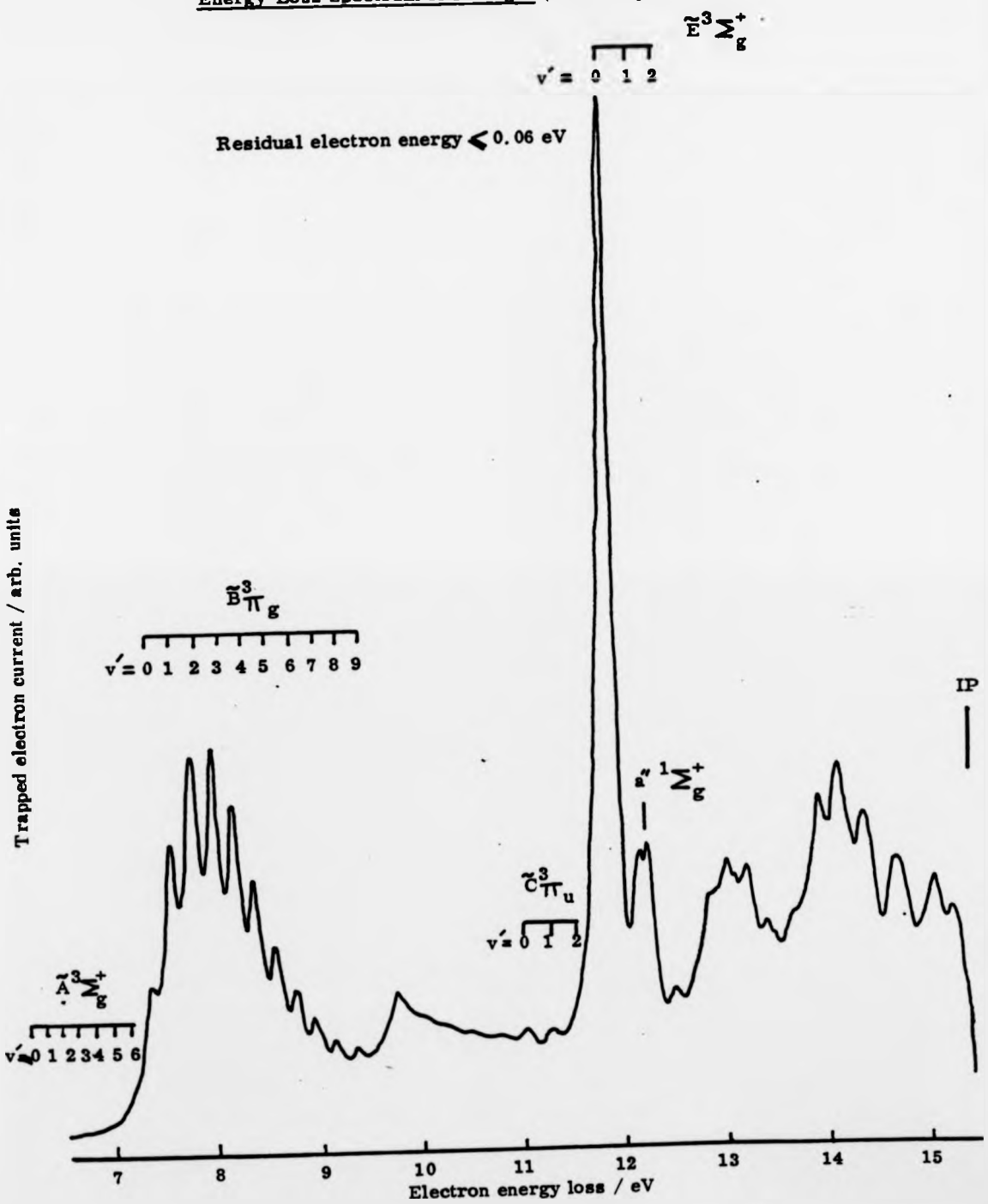

FIG. 34b

Energy Loss Spectrum of Nitrogen (d.c. trap)

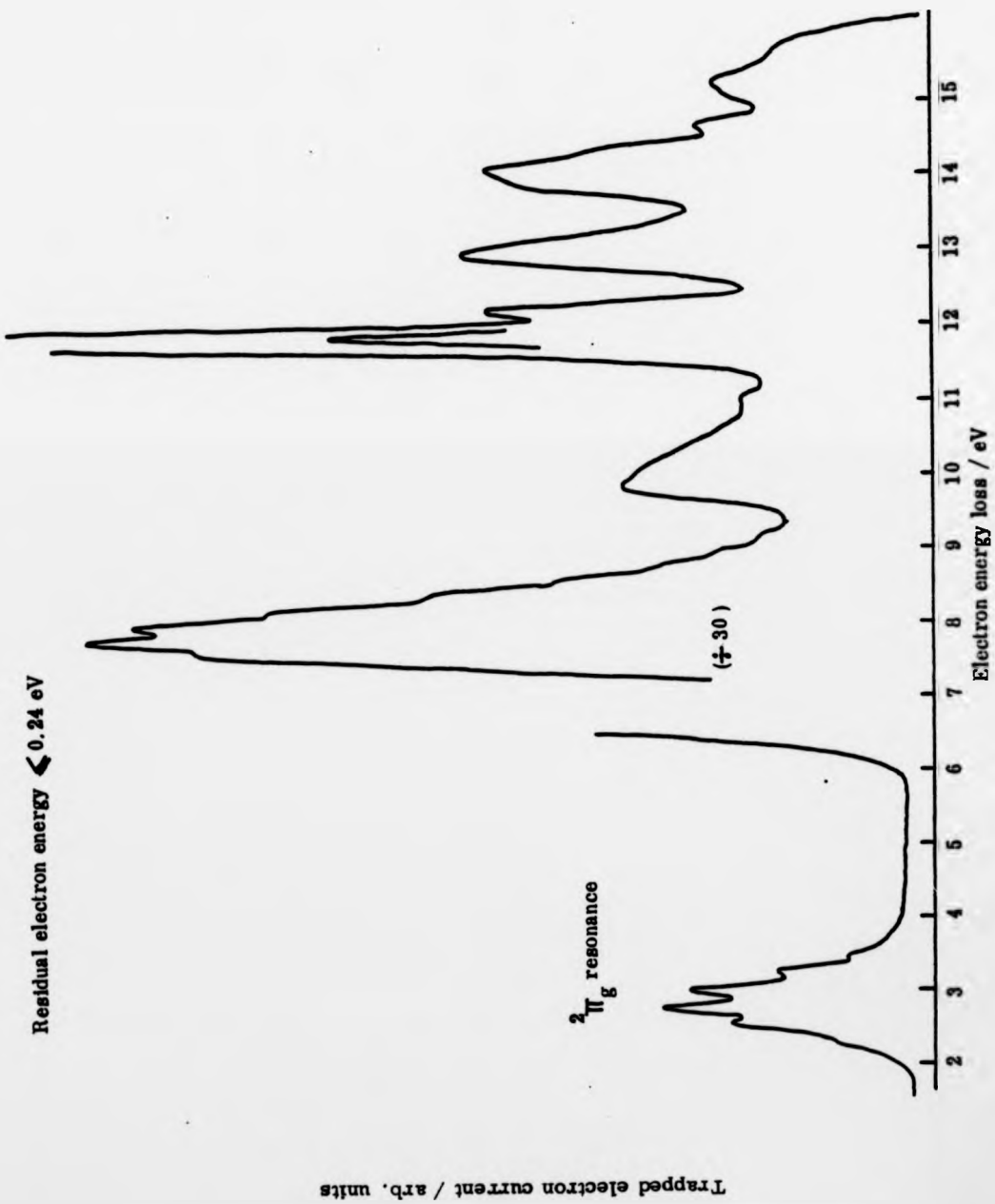

FIG. 35a

Energy Loss Spectrum of Nitrogen (a.c. trap)

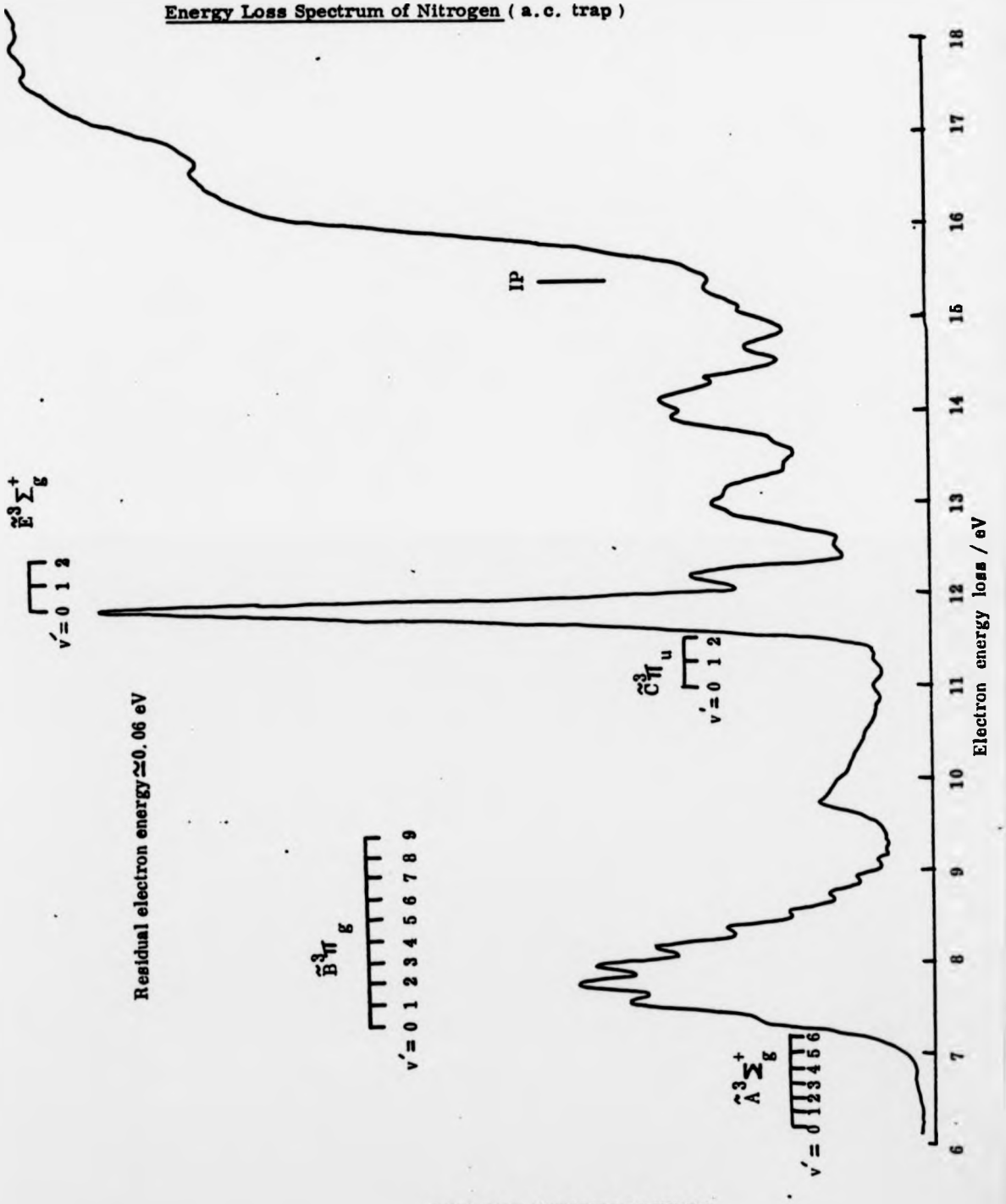

FIG. 35b

Energy Loss Spectrum of Nitrogen (a.c. trap)

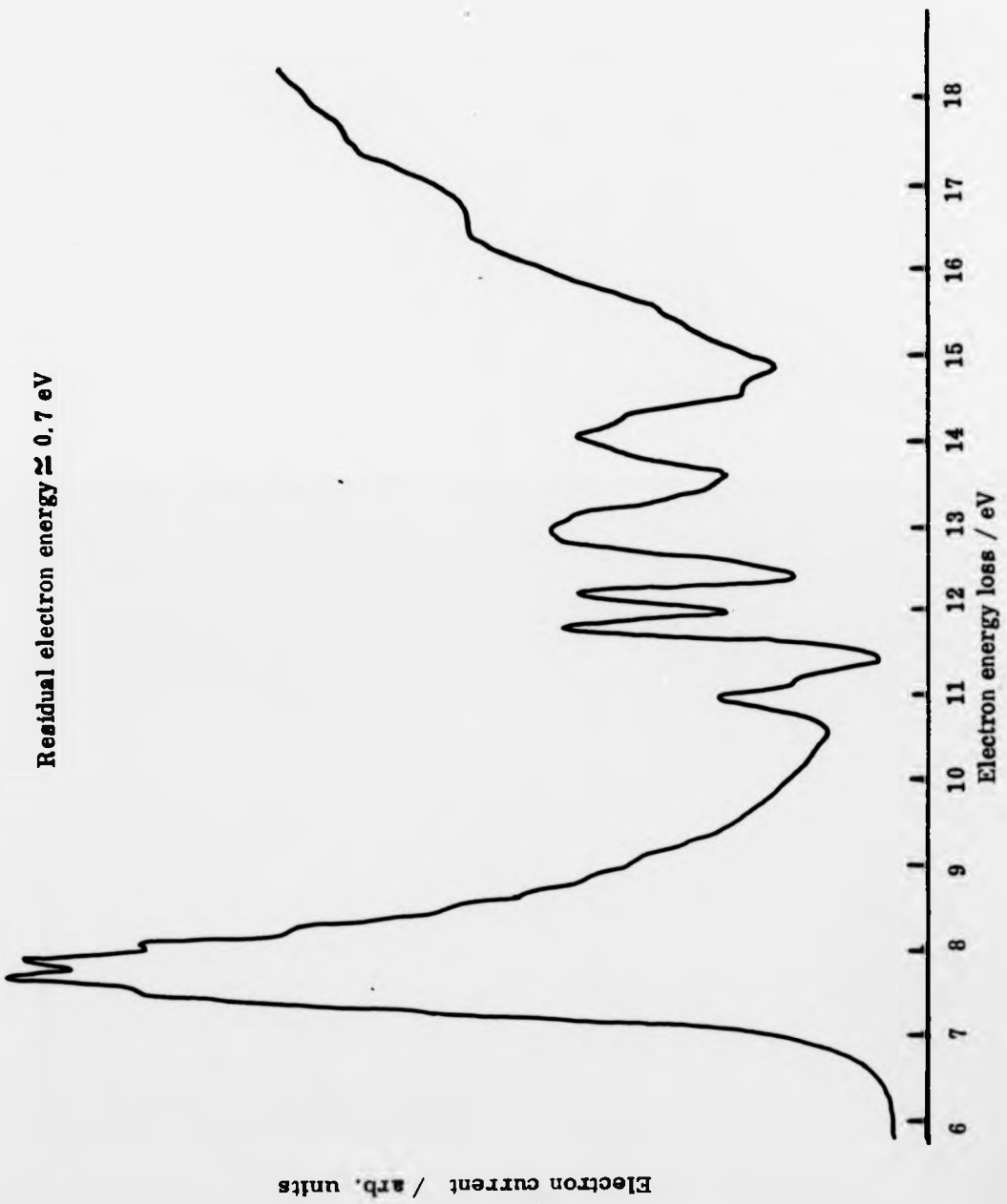

FIG35c

Energy Loss Spectrum of Nitrogen (a.c. trap)

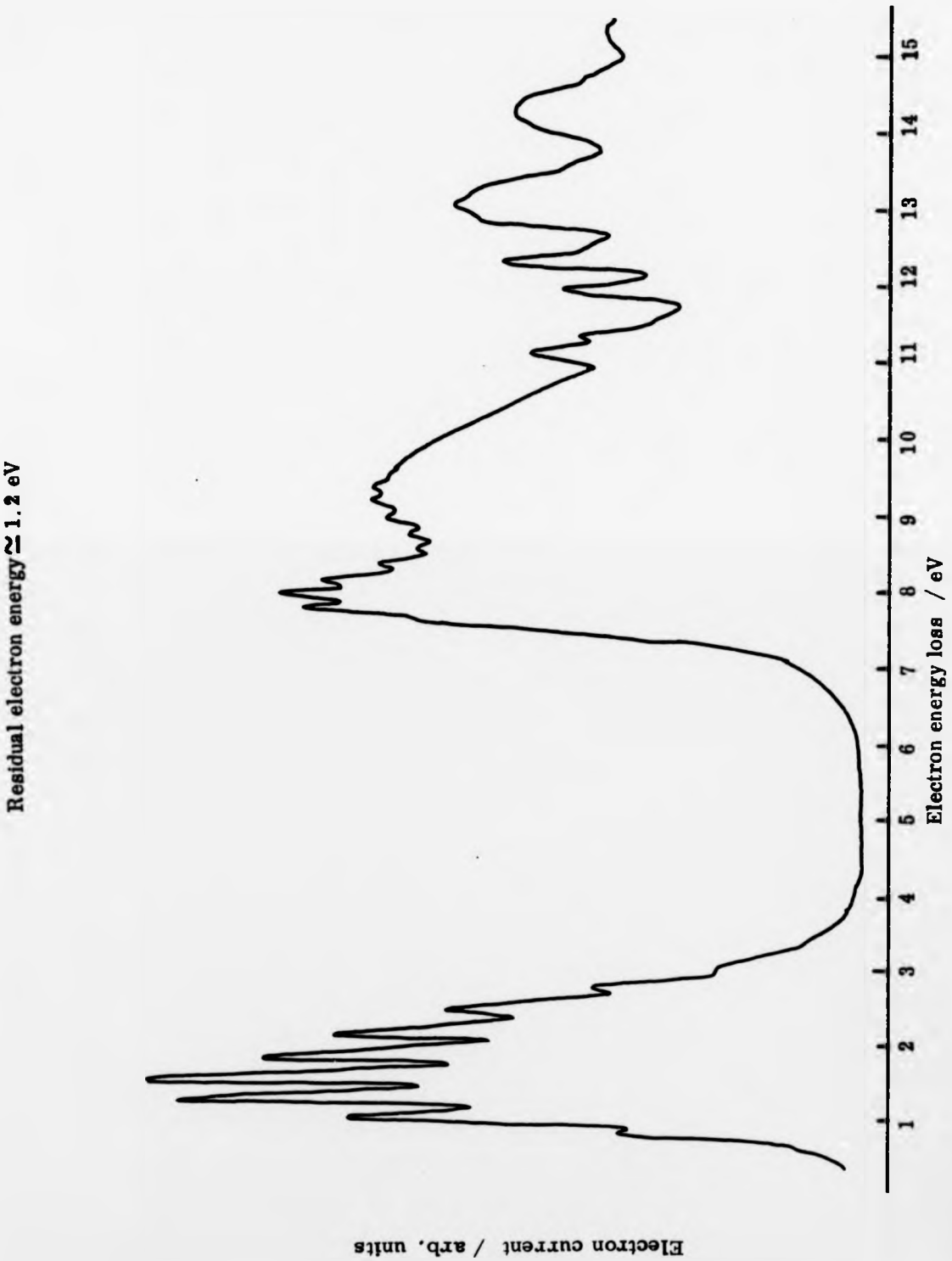

FIG. 35d

Energy Loss Spectrum of Nitrogen (a.c. trap)

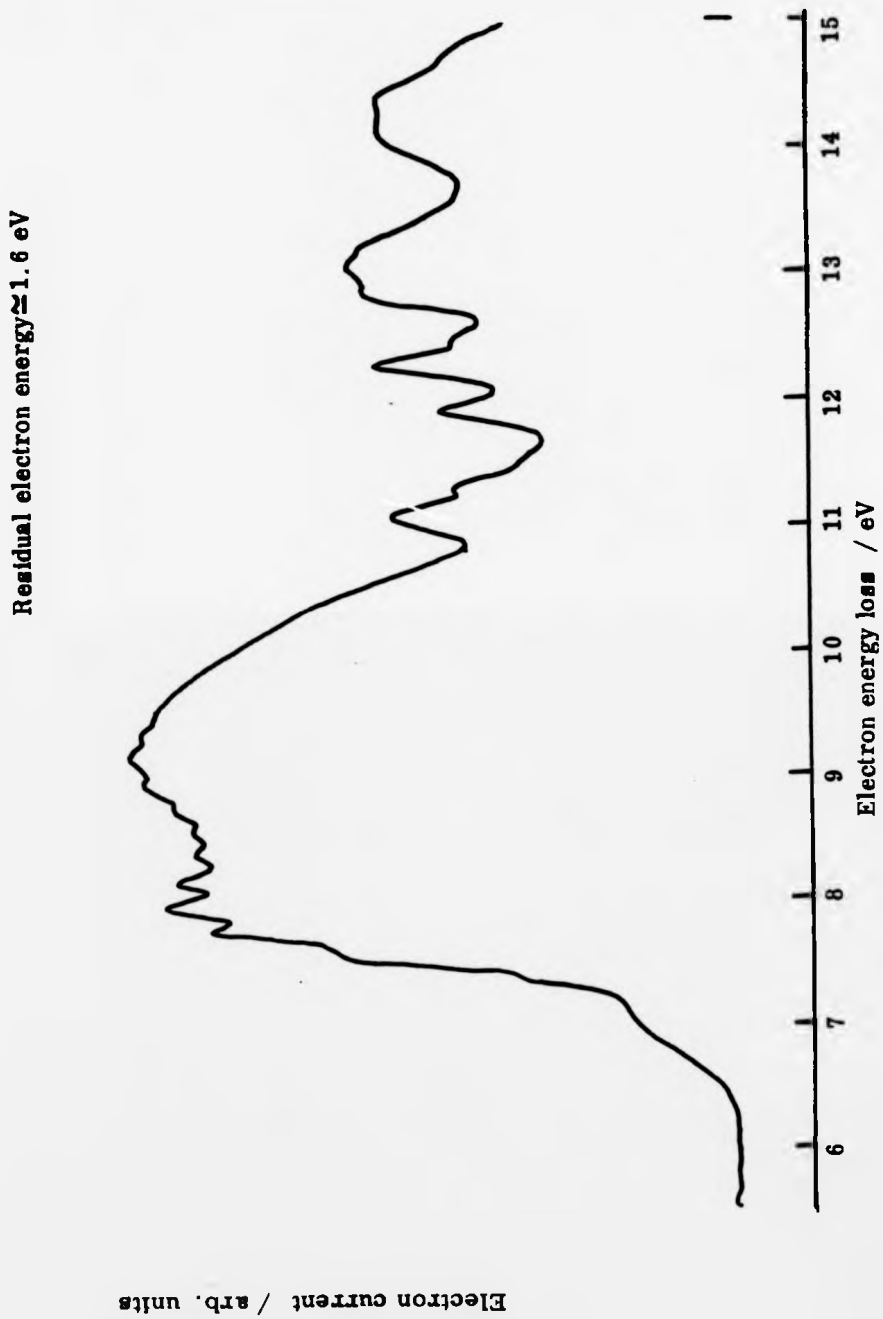

FIG. 35e

Energy Loss Spectra of Nitrogen (a.c. trap)

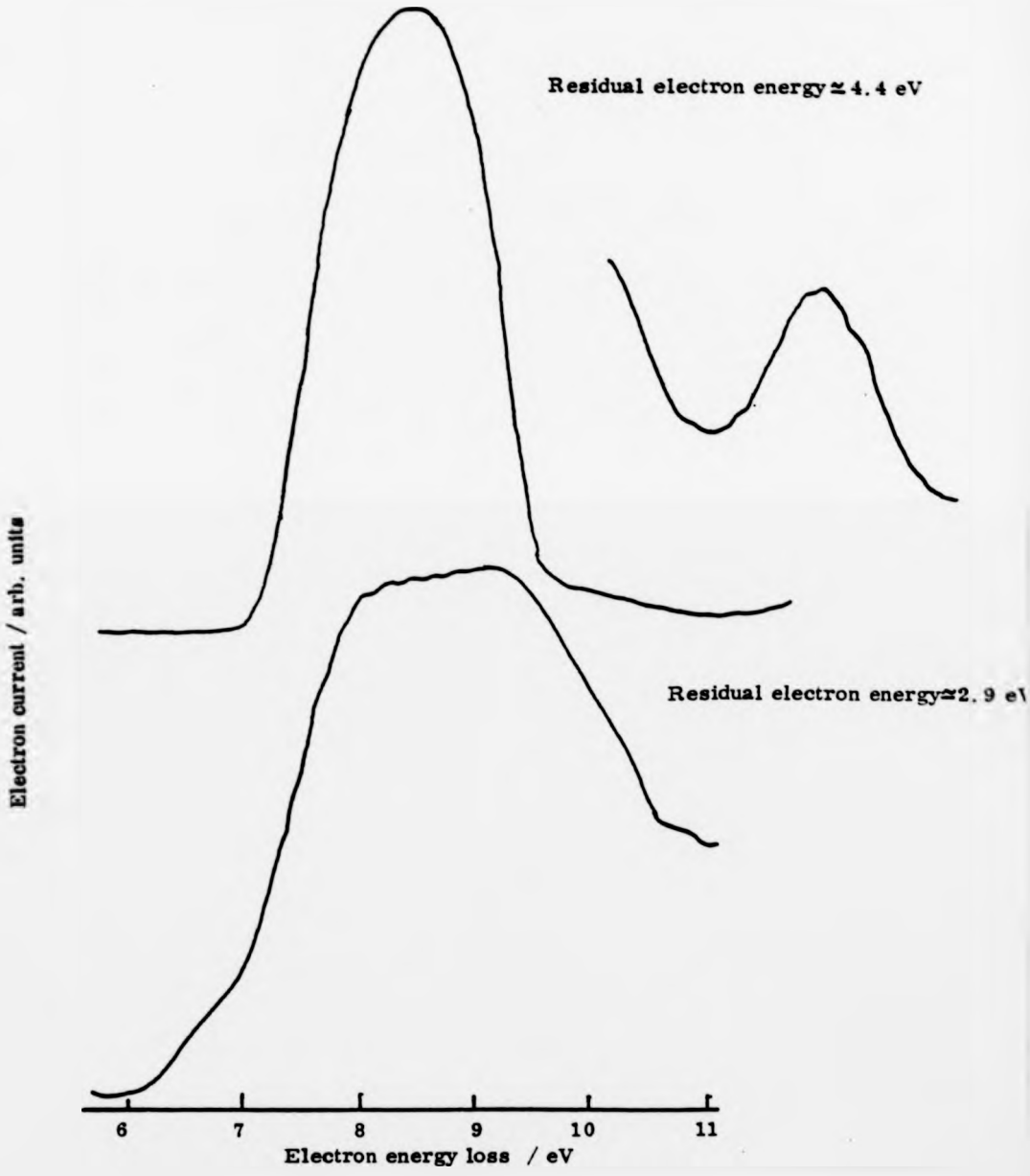

FIG. 36a

Electron Impact Excitation Function of Nitrogen ($\tilde{B}^3\pi_g(v'=3)$)

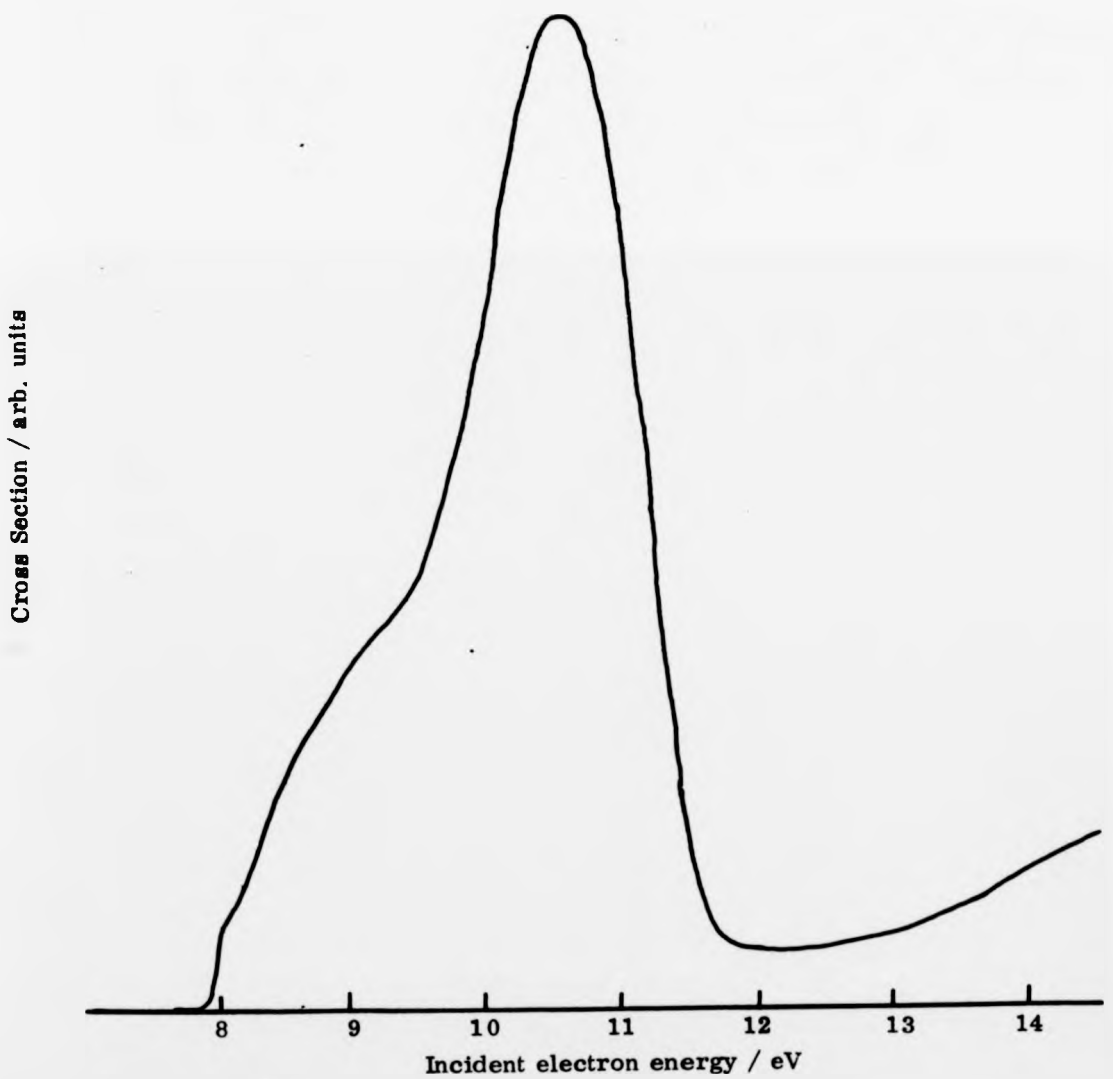

FIG. 36b

Electron Impact Excitation Function of Nitrogen ($\tilde{A}^3\Sigma_u^+$ ($v'=0$))

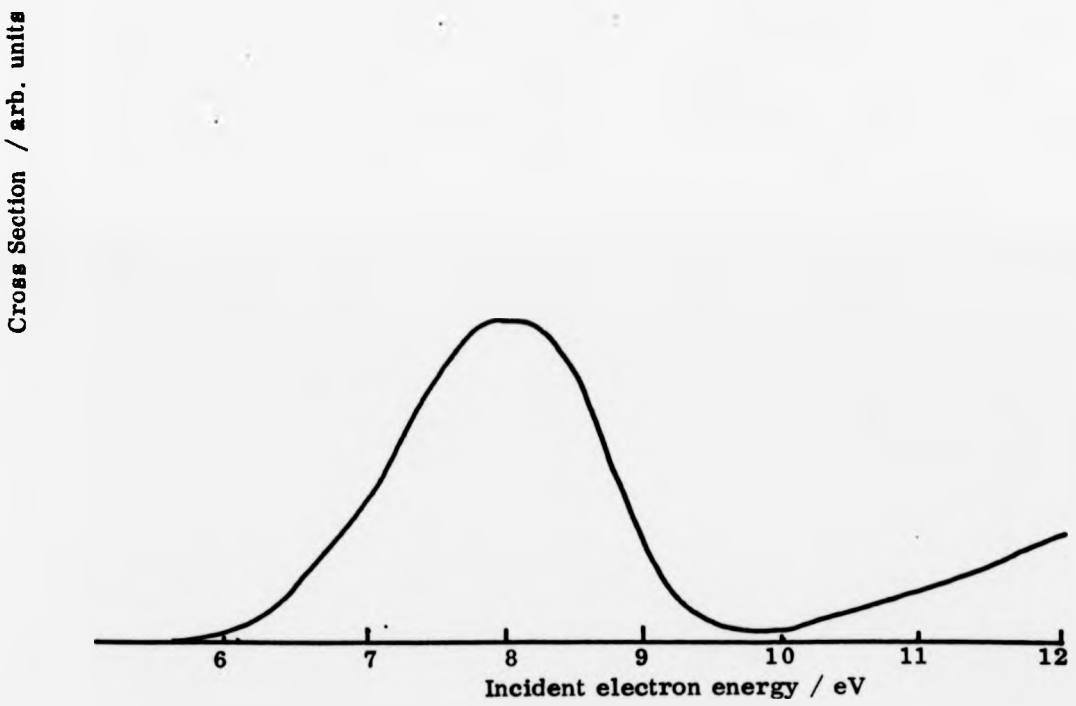

FIG. 36c

Electron Impact Excitation Function of Nitrogen ($\tilde{E}^3\Sigma_g^+$ (v'=0))

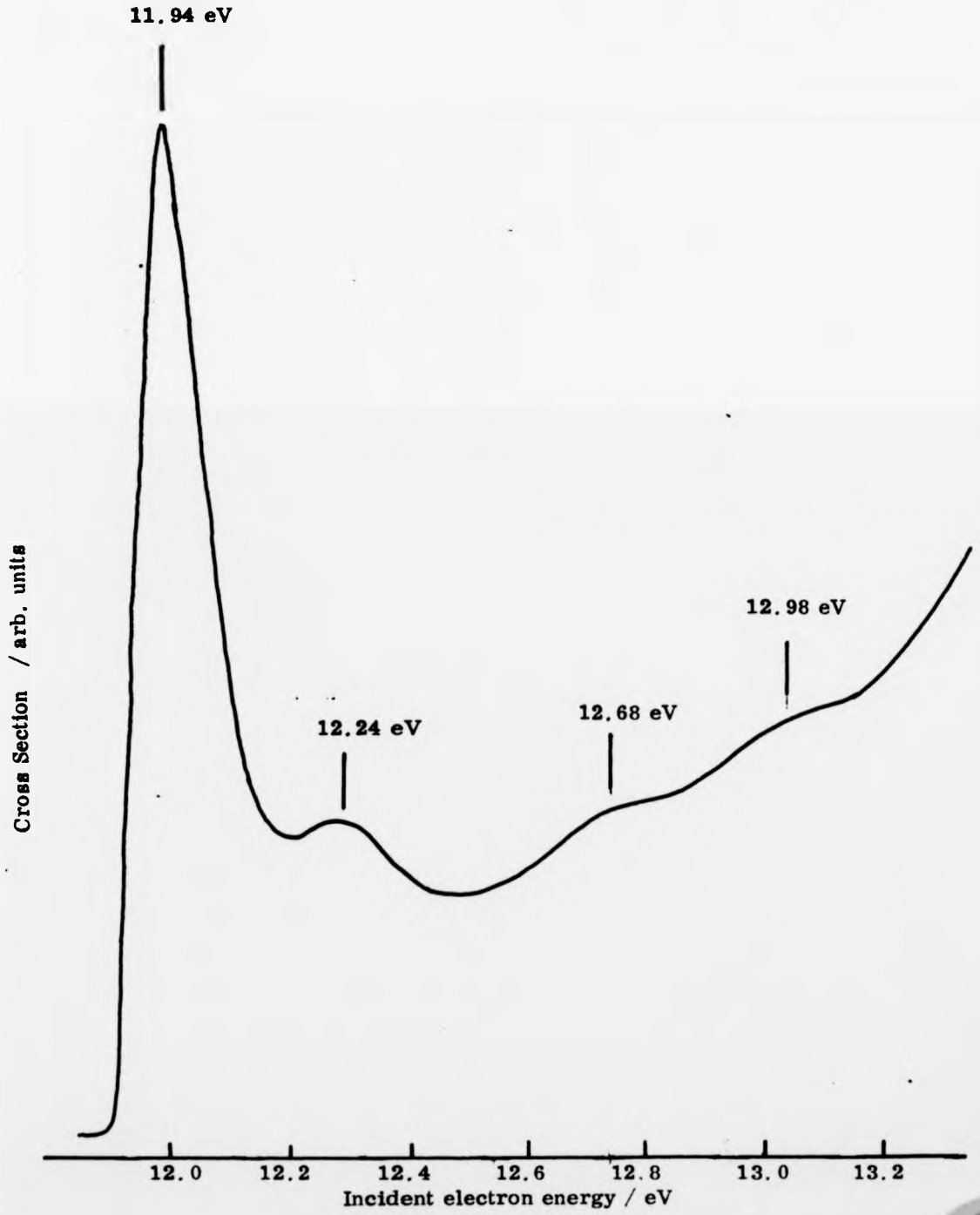

FIG. 36d

Various Electron Impact Excitation Functions of Nitrogen

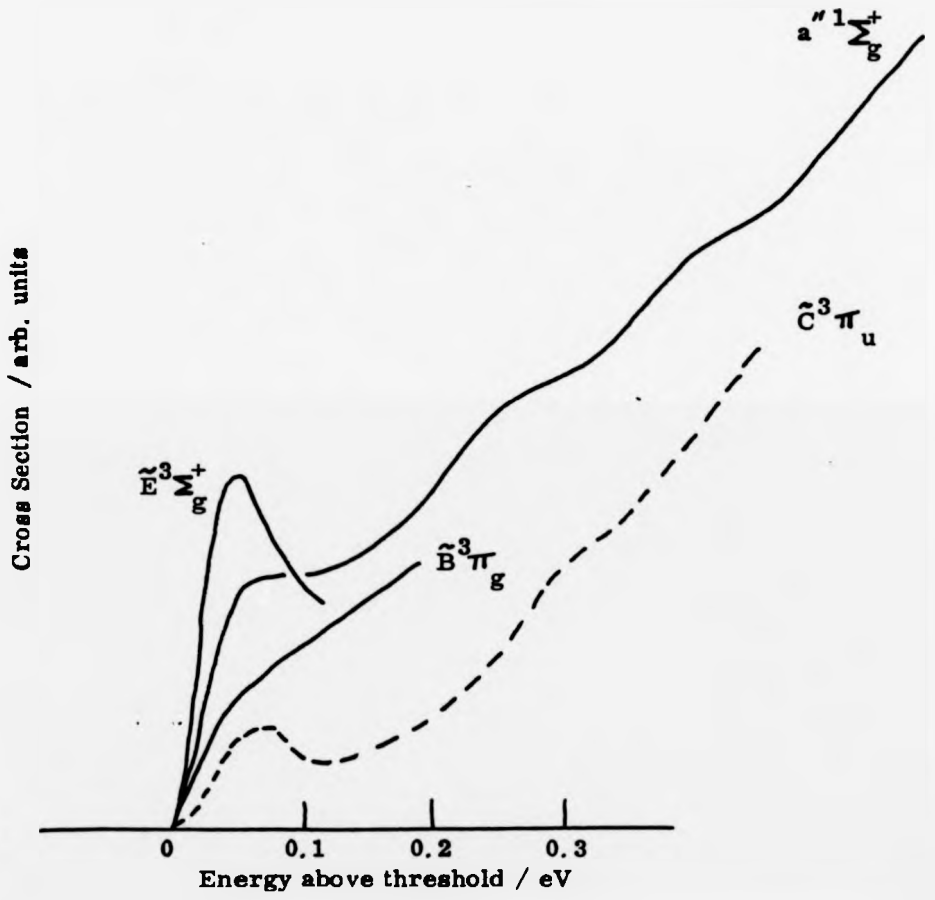

FIG. 37a

Fixed Incident Energy Spectrum of Nitrogen

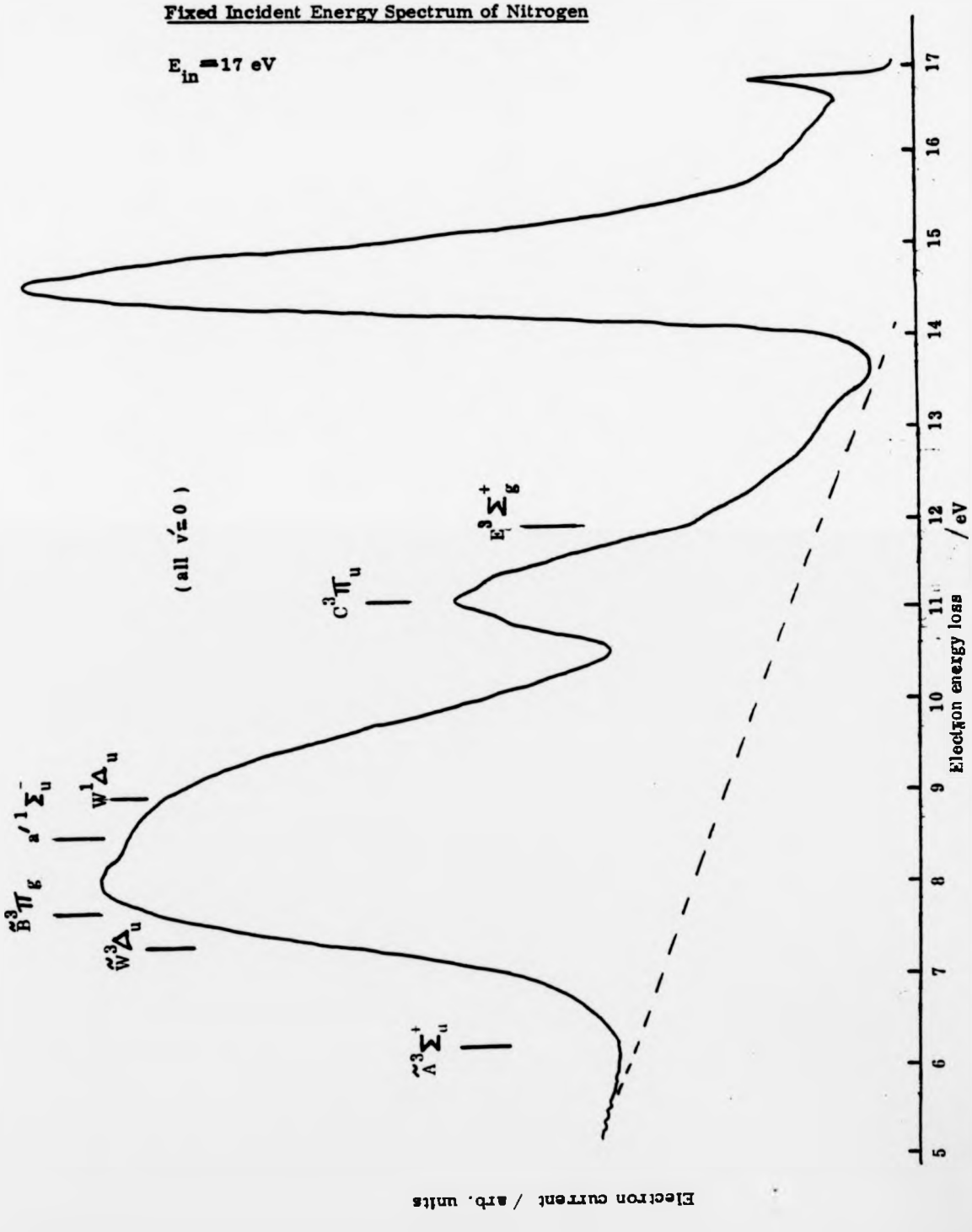

FIG. 37b

Fixed Incident Energy Spectrum of Nitrogen

$E_{in} = 8.5$ eV

scattering spectrometers.[156] Above 11.87 eV a high density of overlapping valence and Rydberg states complicates the picture.

As expected, the most pronounced features in our threshold spectra arise from excitation from the $\tilde{X}^1\Sigma_u^+$ ground state to the $\tilde{B}^3\pi_g$ and $\tilde{E}^3\Sigma_g^+$ excited states, excitation of the latter being strongly resonance enhanced.

The behaviour of structure with varying well depth in the region 9.6-11.6 eV is consistent with the formation of a resonant state of N_2 which dissociates to a nitrogen atom and an unstable negative ion which autoionises giving a near zero energy electron. The following scheme has been proposed by Spence and Burrow[106] and by Huetz et al.[157]

$$e + N_2 \rightarrow N_2^-(\tilde{A}^2\pi_u) \rightarrow N(^4S) + N^-(^3P)$$

$$\downarrow$$

$$N(^4S) + e \ (E_R \approx 70 \text{ meV}).$$

We have used this to calibrate W and derive a value of f in the relationship W = (WDA + f) of + .39 $\pm$ .04V, thus allowing us to assign a true W to each spectrum.

The threshold energy loss spectra show no structure below about 6 eV. As the well depth is increased, however, a feature emerges centered around 2-3 eV. This is due to the well-known $^2\pi_g$ shape resonance which dominates the low energy electron impact cross-section of nitrogen.[15] This $^2\pi_g$ resonance has a remarkable influence on the flow of energy between electrons and molecules, serving by way of inelastic collisions, to remove electrons from the 2-4 eV energy band into the energy regime below 2 eV. We can illustrate this rather well in our

spectrometer. See Fig. 38 . This records the He2^3S excitation function in the presence of a small percentage of N_2. For residual electron energies exceeding about 1.8 eV there is a marked fall-off in signal which we ascribe to secondary inelastic collisions of these post-collision electrons with N_2.

See also, Fig. 35 . This shows some energy-loss spectra at moderately large W. For well depths > 0.7V a broad hump appears in the region 9-11.5 eV. This is structureless except where vibrational structure of the $\tilde{B}^3\pi_g$ state is superimposed on it. At incident energies, where this feature is apparent, we can identify a number of states which, on excitation leave secondary electrons of energy 2-4 eV (Fig. 39). These should not be detected. However, should they undergo secondary inelastic (resonant) collisions, they can be transferred into the residual energy range (say 1 eV for W = 1V) to which the instrument is tuned, enhancing the signal in this range.

If this interpretation is correct then the a.c. trap will not give good results if operated in N_2 at W between about .7 to 4V at pressures such that secondary collisions are important, if there are electrons of energy 2-4 eV in the collision region. For then, resonant scattering will remove signal from the 2-4 eV region and enhance it at below 2 eV. Fig. 35 shows that at W > 4V, this effect has disappeared.

In the deep well-depth spectrum of Fig. 35 , a peak is apparent at $V_a \approx 6.15$V. Under these conditions ($E_{in} = e(V_a+W) = 7.55$ eV) there are no ongoing inelastic processes which leave electrons with the "critical" residual energy (2-4 eV). So, despite the fact that single collision conditions do not exist, we believe this peak to indicate resonance enhancement of

FIG. 38

2^3S Excitation Function of Helium in the Presence of Nitrogen

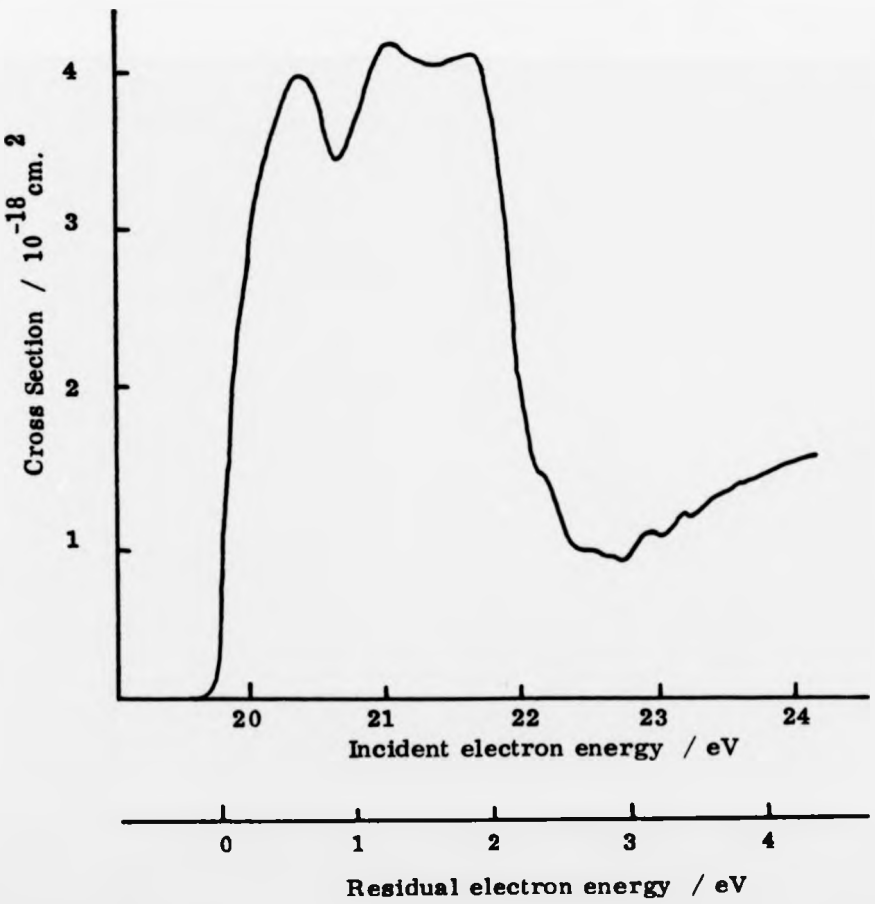

FIG. 39

Some Energy Levels of Nitrogen

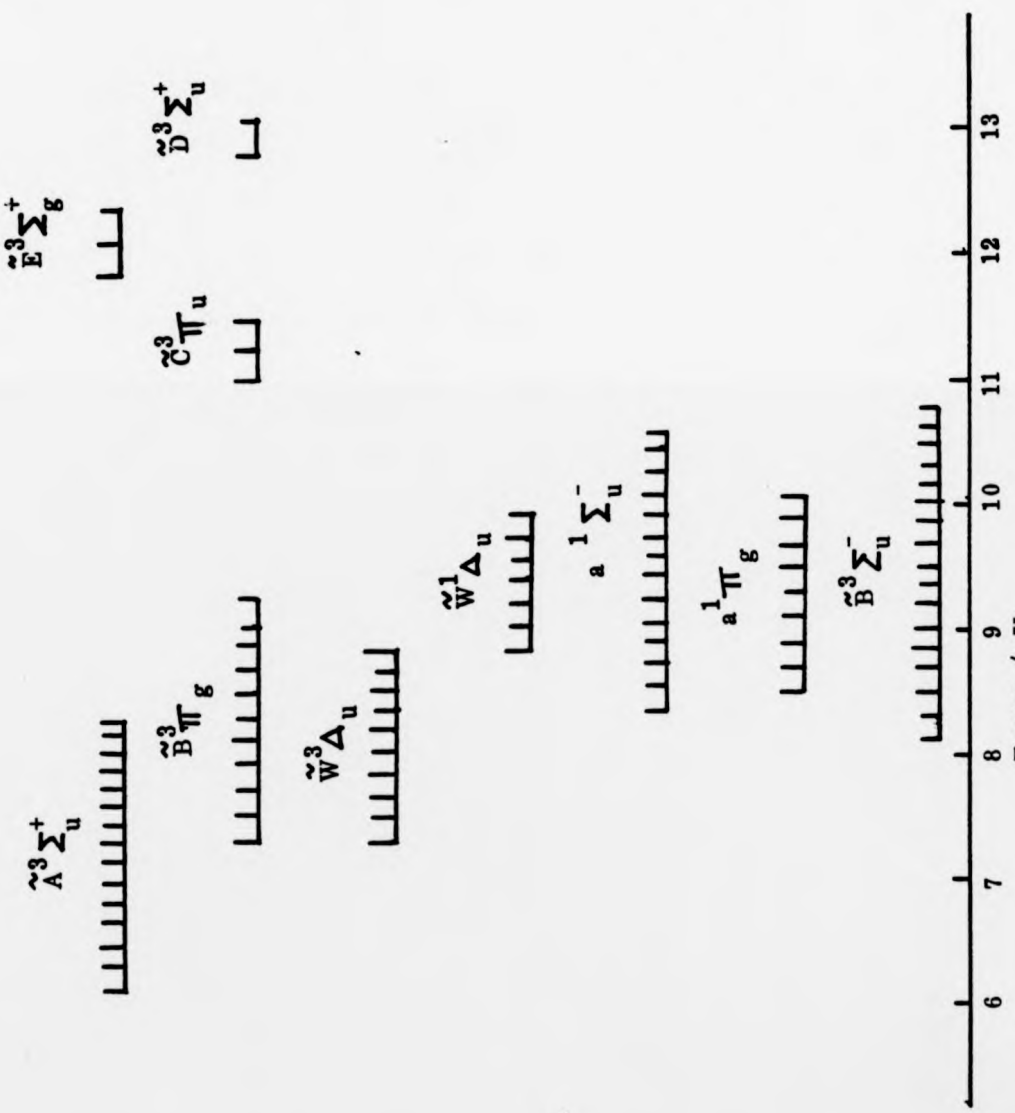

excitation of the lower vibrational levels of the $\tilde{A}^3\Sigma_u^+$ state. Mazeau et al.[158] attribute broad structure in the differential excitation function of the $\tilde{A}^3\Sigma_u^+$ ($v' = 6$) level between 8.2-11 eV to two core excited shape resonances associated with the $\tilde{A}$ state itself. They also identify similar broad overlapping peaks in the $\tilde{B}^3\pi_g$ excitation function which they assign to shape resonances associated with the $\tilde{B}$ state. We do not expect to observe resonance enhancement of the $\tilde{B}$ state due to the masking effect of secondary collisions.

Fig. 40 shows modulated trap, constant residual energy spectra between 0-5 eV for a variety of well depths. The shift in position of the structure to higher energies as W is decreased (energy loss increased) along with the large decrease in intensity are consistent with the behaviour associated with the $^2\pi_g$ shape resonance.[15],[25]

(b) Excitation Functions

The effects of secondary inelastic collisions in N_2 as discussed in 5.3.2(a), are also manifest in excitation functions.[103] See Fig. 36a . This shows an apparent excitation function for the $\tilde{B}^3\pi_g$ state, over an extended W range. The large maximum at W ≈ 2V followed by a minimum, we ascribe to signal enhancement and diminution as described. This effect appears in all excitation functions where post-collision electrons of 2-4 eV can be present. To ensure that we get good excitation functions, unpolluted by such secondary processes, we can impose certain limitations on our range of measurements. We should work in N_2, only at low W except where states are well separated in energy or for the lowest lying excited state.

FIG. 40

Energy Loss Spectra of Nitrogen ($^2\pi_g$ resonance)

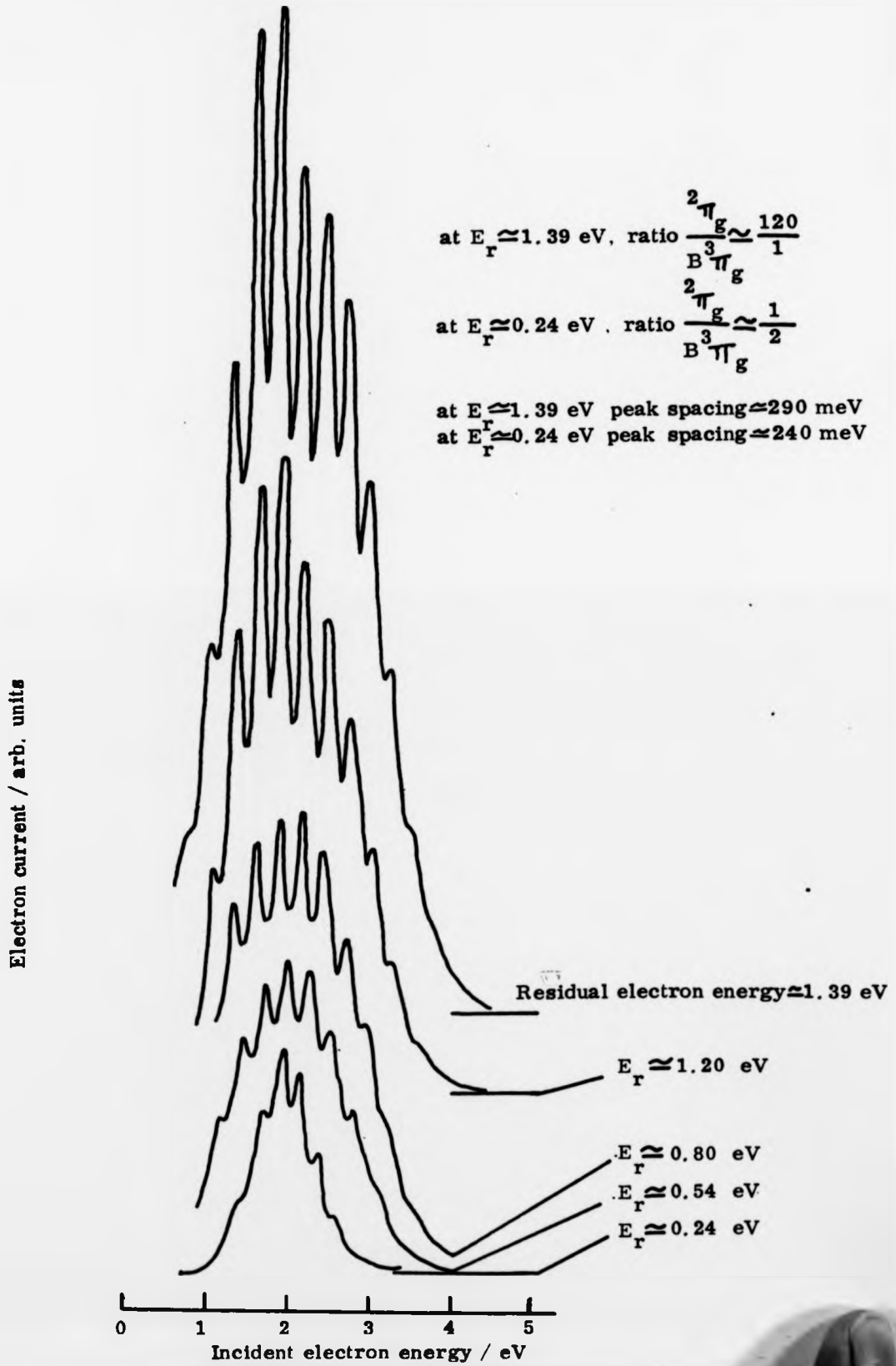

This leaves us with two states, the $A^3\Sigma_u^+$ (lowest excited state) and the $E^3\Sigma_g^+$ (for W < 1V) for which we are not restricted to W < .7V.

Fig. 36b $\tilde{A}^3\Sigma_u^+$ ($v' = 0$, $eV_A = 6.15$ eV).

We see a broad maximum at ≈ 2.5 eV above threshold i.e. $E_{in} = 8.6$ eV. Differential excitation functions of Mazeau et al.[158] exhibit broad features in this region which is consistent with earlier observations on our energy loss spectra.

Fig. 36c $\tilde{E}^3\Sigma_g^+$ ($v' = 0$, $eV_A = 11.87$ eV).

Table 10 compares the positions of structures in our $\tilde{E}^3\Sigma_g^+$ ($v' = 0$) excitation functions, up to about 1 eV above threshold, with the observations of other workers. This close agreement confirms the operation of the trap under the restrictions discussed previously. Note that the relative magnitude of this transition with respect to, for example, the $\tilde{C}$ state, is high compared with the absolute magnitudes of Trajmar et al.[163]

Present Results	Trajmar et al.
(W = 1.2V) $\tilde{E}/\tilde{C}$ ≈ 1:1	$\tilde{E}/\tilde{C}$ ≈ 1:80

Fig. 36d , presents excitation functions for some processes over a small range of W (0-0.7V).

(c) Fixed Incident Energy Spectra

At moderate pressures, fixed incident energy spectra show the secondary inelastic effect where expected. Thus in the 17 eV spectrum of Fig. 37a , the very large peak at 2 eV

TABLE 10

POSITION OF STRUCTURE IN $\tilde{E}^3\Sigma_g^+$ ($v' = 0$) EXCITATION FUNCTION (eV)

Present results (Fig.36c)	Brunt et al. (ref. 159)	Sanche and Schulz (ref. 41)	Mazeau et al. (ref. 160)	Lawton and Pichanick (ref. 161)	Golden et al. (ref. 162)
11.94	11.93	11.92	11.9		11.92
					12.03
12.24	12.18	12.18-12.27	12.14		12.12
					12.33
	12.54	12.64	12.54	12.59	12.54
12.68					12.70
	12.78	12.87	12.78	12.80	12.80
12.98	12.99		12.98	13.03	12.98
			13.21		13.21

Present results: structure in $\tilde{E}^3\Sigma_g$ ($v' = 0$) excitation function

Brunt et al.: structure in total metastable cross-section

Sanche and Schulz: electron transmission

Mazeau et al.: excitation of $\tilde{E}^3\Sigma_g$ ($v' = 0$) state

Lawton and Pichanick: structure in total metastable cross-section

Golden et al.: $\tilde{E}^3\Sigma_g$ state, from an investigation of the $\tilde{C}^3\pi_u$-$\tilde{B}^3\pi_g$ transition following population of the $\tilde{C}$ state from the $\tilde{E}$ state.

arises from secondary collisions of electrons in the 2-4 eV energy range. The remainder of the spectrum, whose resolution is poor, arises from excitation of a number of states. The magnitudes of the energy loss peaks are consistent with the total cross-sections measured by Trajmar et al.[163] At 8.5 eV incident energy, excitation of the $\tilde{A}^3\Sigma_u^+$ and $\tilde{B}^3\pi_g$ states is apparent with the $\tilde{A}$ state peak magnitude approaching that of the $\tilde{B}$ state. (Fig.37b).

CONCLUSION

Nitrogen has been extensively studied in electron scattering. Our results are of too poor resolution to afford any new information on direct excitation processes. However, we have used the electron trap to demonstrate the dramatic effect of secondary collision processes in nominally single-collision experiments in this gas and it may be that previous results should be reinterpreted with this in mind. For our instrument to work at acceptably low pressures, the data handling system must be improved to increase sensitivity.

It seems likely that the electron trap is sensitive to shape resonances associated with excited states as well as ground state shape resonances and this should be explored further. A detailed knowledge of the various collision cross-sections in electron-N_2 processes is important for an understanding of a variety of discharge phenomena.[164] Trajmar et al. have produced differential and associated integral cross-sections for excitation of several electronic states

in nitrogen but these data are probably not good at near threshold energies. The electron trap is capable of yielding information on these cross-sections at very low energies.

5.4.1 Electron Energy Loss Spectra for CO_2, CS_2 and COS

We have measured simple trapped electron spectra for carbon dioxide, carbon disulphide and carbonyl sulphide. Of these, the low-lying electronic states of CO_2 have been fairly well characterised, but until recently few state assignments for the sulphur containing analogues were firm. Our electron scattering data[12] suggested processes which have since been supported by higher resolution work.

5.4.2 Results

Simple d.c. trapped electron spectra at different well depths are illustrated in Figs. 41 (CO_2), 42 (CS_2) and 43 (COS). These spectra were recorded on a machine described in detail elsewhere.[11] In addition, a modulated trap spectrum of COS is shown. Electron energies were calibrated with reference to a 10.04 eV transition in krypton.[165]

5.4.3 Discussion

The valence shell electron configuration of each of these molecules may be written $(\sigma_g)^2(\sigma_u)^2(\sigma_g)^2(\sigma_u)^2(\pi_u)^4(\pi_g)^4$ the lowest available unoccupied orbital being π_u (or π^*). So we expect the important low-lying electronic states to be $^{1,3}\Sigma^+$, $^{1,3}\Sigma^-$ and $^{1,3}\Delta$ resulting from $\pi_u \leftarrow \pi_g$ transitions. (These assignments assume linear geometry).

FIG. 41

Energy Loss Spectra of CO_2

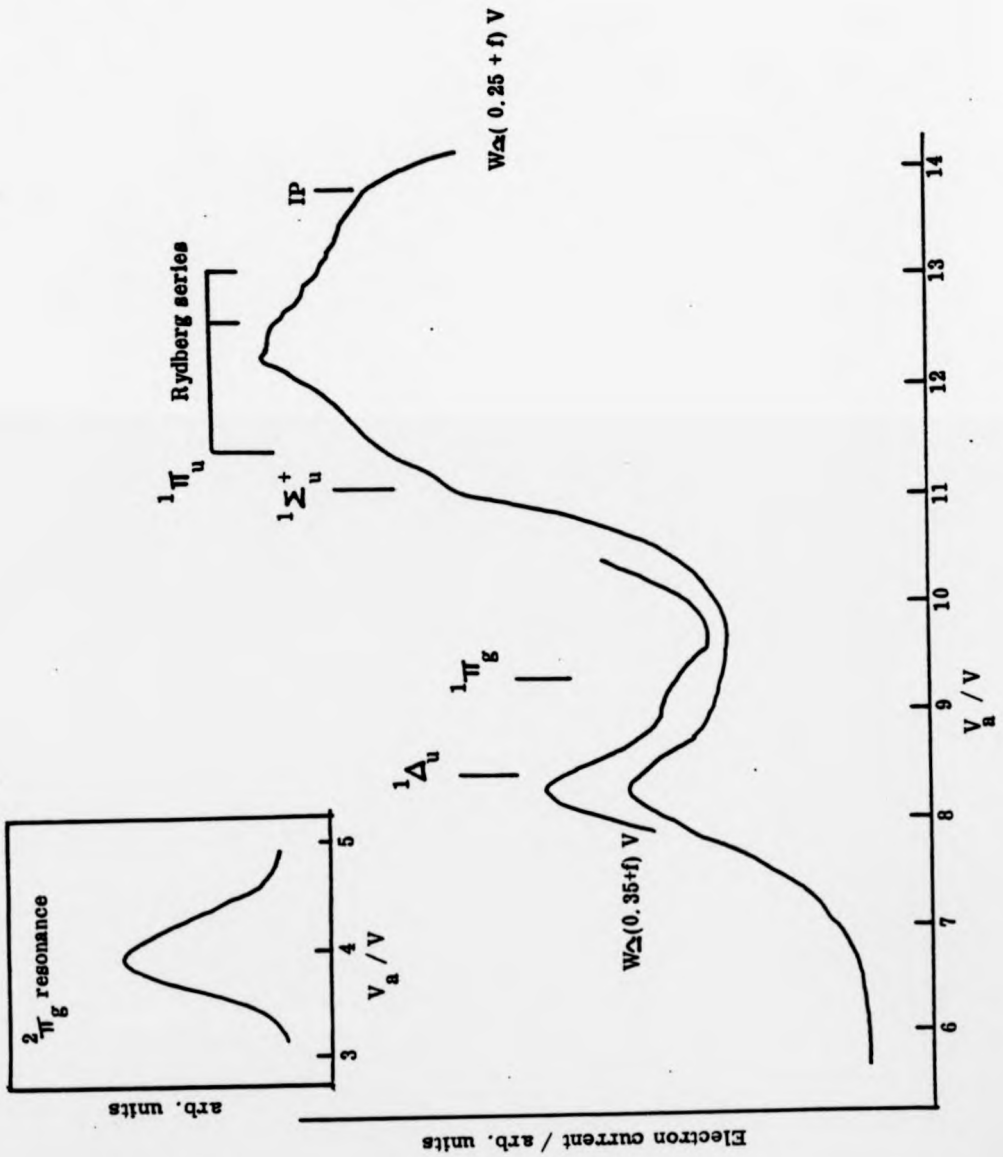

FIG. 42

Energy Loss Spectra of CS_2

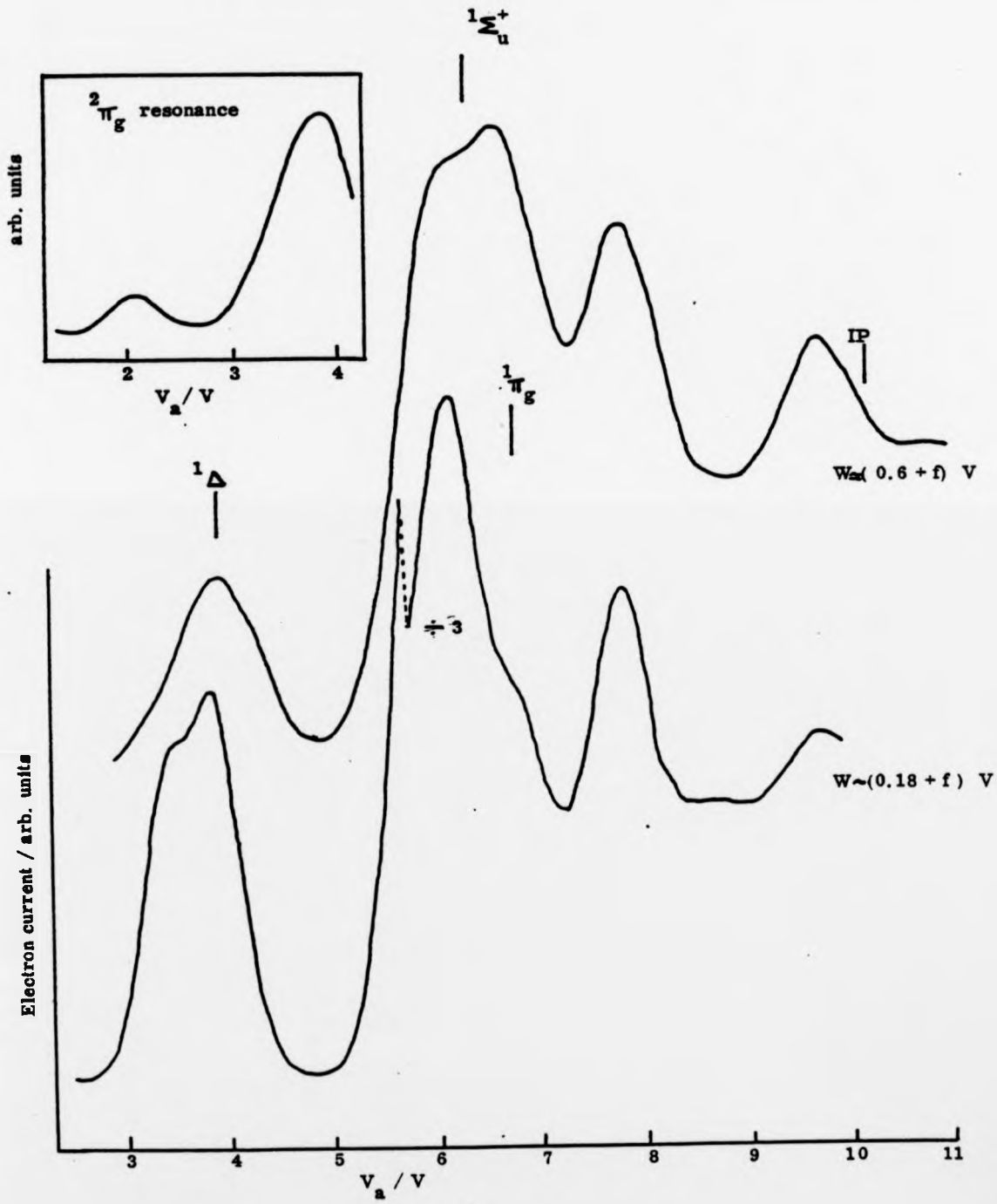

FIG. 43

Energy Loss Spectra of COS

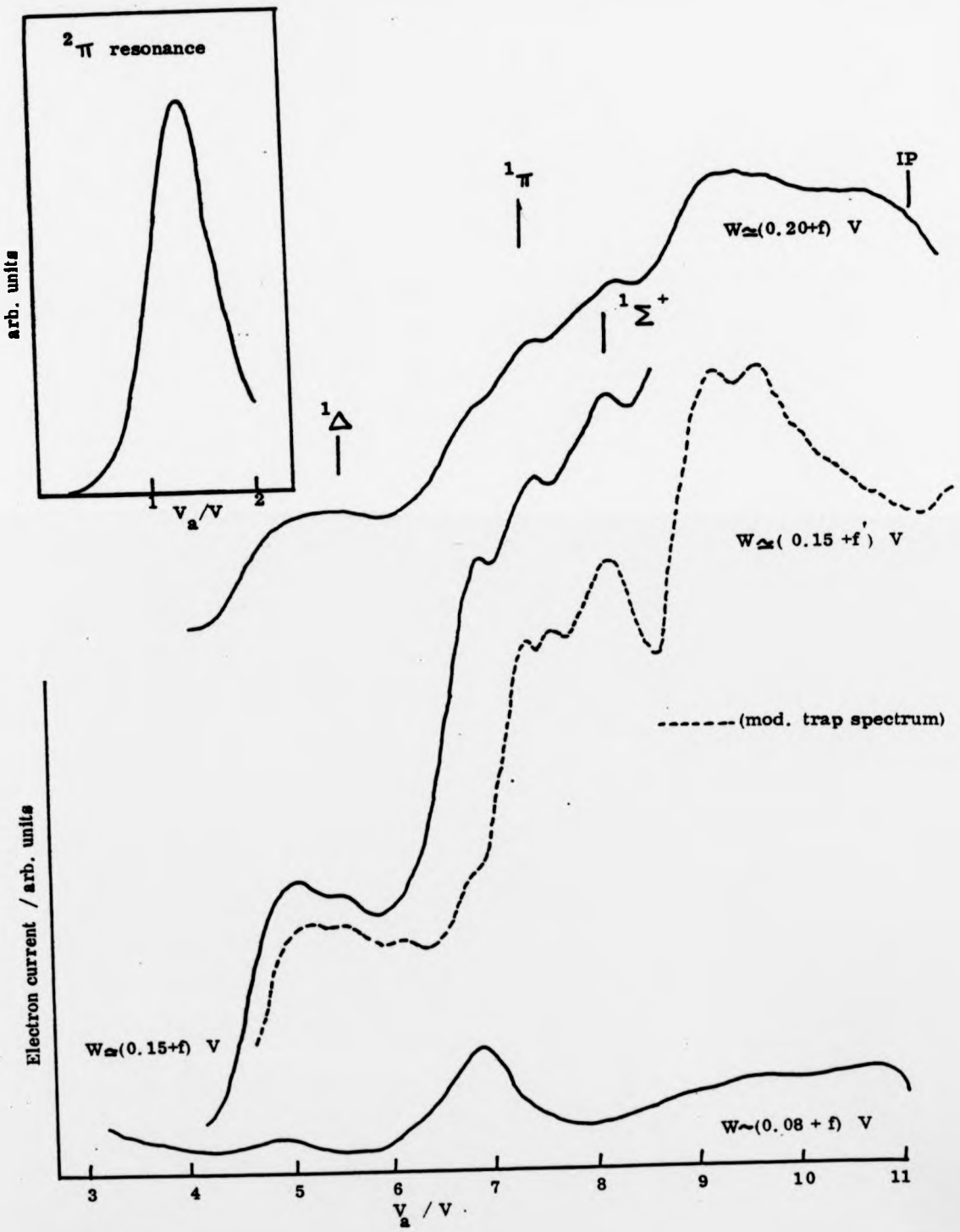

(a) Carbon Dioxide

We use CO_2 simply as a reference gas. The low well-depth spectrum of Fig. 41 agrees with the truly threshold spectrum of ref. 166 obtained using the SF_6 scavenger technique. At the high energy end, excitation of the $^1\Sigma_u^+$ state at ≈ 11.0 eV is apparent, together with a Rydberg series (minor I series of ref. 167). At lower energies the peak at 8.24 eV is clearly dominated by optically forbidden transitions. On increasing W, the $^1\pi_g$ state emerges at ≈ 9.3 eV. This particular feature, not accessible in the SF_6 scavenger experiment, is important to our interpretation of the spectra of CS_2. The CO_2 spectrum is detailed in Table 11.

(b) Carbon Disulphide

The various spectra of CS_2 shown in Fig. 42 demonstrate nicely how markedly relative excitation cross-sections can change for very small changes in incident energy. The strongest transition in the u.v. spectrum corresponds to excitation of the optically allowed $^1\Sigma_u^+$ state (or more correctly, $^1B_2$) between 5.8 and 6.7 eV, maximum intensity 6.27 eV. This transition also dominates electron energy loss spectra at higher incident energies (e.g. 10 eV and above).[171],[172] Our results show that this is not the strongest transition at near threshold energies. Then the position of maximum intensity is ≈ 6.1 eV. Other threshold spectra agree with this.[166] A 6.1 eV transition is not apparent in a 10 eV electron scattering spectrum. We have somewhat tentatively assigned it as a $^3\pi_g$ state. As the electron energy is increased above threshold the intensity of this feature drops while a peak at ≈ 6.8 eV emerges. This we labelled as $^1\pi_g$ (12), an assignment which has since gained support from

TABLE 11

ELECTRONIC EXCITATION OF CO_2

excitation energy (T_{max})/eV.

Electron Scattering				u.v.	Theory	Assignment
Present results	(ref.166)	(ref.13)	(ref.168)	(ref.169)	(ref.170)	
∿ 7.2	7.2-7.3		∿ 7.3		7.35	$^3\Sigma_u^+$
∿ 7.85	7.7-7.8		∿ 8.1		7.83	$^3\Delta_u$
8.24	8.3		∿ 8.3		8.24	$^3\Sigma_u^-$
					8.27	$^1\Sigma_u^-$
		8.6	∿ 8.6	8.41	8.38	$^1\Delta_u$
	9.1		∿ 8.8		8.95	$^3\pi_g$
9.25		9.35	∿ 9.4	9.31	9.23	$^1\pi_g$
11.0	11.0	11.04		11.08	11.07	$^1\Sigma_u^+$
11.4	11.4	11.41			11.53	$^1\pi_u$

ionisation potential = 13.79 eV (ref.167)

angular distribution measurements at high incident energies.[171][172] Our spectrum in the region 6-7 eV also is compatible with the presence of a feature at 6.74 eV, picked up by Wilden and Comer, but not assigned.[172] Clearly, this spectral region merits further investigation with improved electron energy resolution at near-threshold energies. As we pointed out, the threshold peak at ≐ 7.7 eV is anomalously strong.[12] Wilden and Comer have since accounted for this by resolving a number of spin-forbidden transitions in this energy region, transitions which clearly become increasingly important at low incident energies.

A number of excited states are expected to lie between 3 eV and 4 eV. Our spectra show that the $^1\Delta_u$ state (or $^1A_2$) at 3.9 eV dominates as the well is increased. At lower energies spectral behaviour is consistent with the existence of more than one transition. Mulliken[173] has postulated that the lowest excited state, $^3\Sigma^+$, lies at ≈ 2.4 eV above the ground state and Fukui et al.[174] point out that CS_2 excited by electrons of energy ≲ 3.1 eV (below the origin of the $^3\Delta_u$ or $^3A_2$ state which is 3.25 eV) emits radiation in the energy region 3.1-2.1 eV. However, we can detect no electron energy loss in this region at low well-depths. At higher well-depths the expected $^2\pi_u$ shape resonance decaying to the vibrationally excited ground state species, appears at ≈ 2 eV and this could mask an underlying weak feature. Neither can we confirm the presence of a transition at ≈ 5.5 eV, first reported by Hubin-Franskin and Collin[166] and later by Wilden and Comer.[172] Flicker et al.[171] observe no transitions between 4.5-5.5 eV despite a careful search. As indicated above, we locate the $^2\pi_u$ shape resonance at ≈ 2 eV. Calculations place this at 1.85 eV.[176] The CS_2 spectra are detailed in Table 12 .

TABLE 12

ELECTRONIC EXCITATION OF CS_2

excitation energy (T_{max})/eV							
	Electron Scattering					u.v.	Assignment
Present results (ref.12)	(ref. 171)	(ref. 13)	(ref. 166)	(ref. 172)	(ref. 167)	(ref. 169)	
3.4	3.36	3.36	3.3			3.49	$^3\Delta_u$ triplet
	3.65	3.65					
3.8	3.91	3.91	3.9		3.9	3.89	$^1\Delta_u$
			5.5	5.5-5.8			$^3B_2$
6.1			6.1				$^3\pi_g$
	6.27	6.27		5.8-6.7	6.3	6.29	$^1\Sigma_u^+$
				6.74			
6.85	6.79	6.79	6.6	6.81	6.8	6.79	$^1\pi_g$
				6.93			$^3\Sigma_u^+$ or $^3\pi_u$
		7.12		7.0-7.6			$^1\Sigma_u^+$ or $^1\pi_u$
		7.22				7.2	
		7.33					
				7.67			$^3\pi_u$
7.75		7.78	7.7				Rydberg (I)
		7.97		7.86			4d triplet
		8.23				8.18	
8.7		8.61	8.5				
9.6		9.53	9.5				

ionisation potential = 10.08 eV (ref. 167)

(c) Carbonyl Sulphide

As for CS_2, our COS d.c. spectra vary dramatically with changing well-depth. Some are illustrated in Fig. 43 , together with a modulated trap spectrum.

The most prominent transition in the u.v. spectrum and high energy electron energy loss spectra is to the $^1\Sigma^+$ state which maximises at 8.12 eV. This peak is apparent in all our spectra, although it appears to be contaminated with a slightly higher energy state. In the COS molecule, the $^1\pi$ state at 7.4 eV also apparently contributes to our electron energy loss. Between these two transitions, our modulated trap picks up a hitherto undetected transition at 7.7 eV energy loss. Very recently, a high resolution spectrum of COS has revealed a transition at 7.59 eV.(177) Also, prominent in our simple d.c. spectrum is a peak at 6.9 eV. In fact, this is the strongest peak at very low well-depths. This feature is still present in the modulated trap spectrum although it is less intense than in the d.c. spectra. This may mean that the d.c. trap is collecting some negative ion signal at this energy. In any event, it seems clear that there are at least two "new" transitions at 7.7 eV and 6.9 eV, presumably to triplet states, which have yet to be assigned. The 9.7 eV transition in our modulated trap spectrum fits a Rydberg series (Series II of ref. 177). At lower energy losses, a number of states are expected. The $^1\Delta$ state is at 5.5 eV. Below this, in both the d.c. and a.c. spectra, the peak shapes change in intensity with changing W in a way which suggests the presence of several transitions between about 4.9 eV and 6 eV. We locate the COS $^2\pi_u$ shape resonance at about 1.2 eV, in good agreement with

total collision cross-section measurements.[178] Data are presented in Table 13.

TABLE 13

ELECTRONIC EXCITATION OF COS

excitation energy (T_{max})/eV								
	Electron Scattering						u.v.	Assignment
Present results (ref.12)	Present results (mod.trap)	(ref.177)	(ref.171)	(ref.13)	(ref.175)	(ref.167)	(ref.169)	
4.9 (low W)			4.94	4.94	4.85			$^3\Sigma^+$
								$^3\Delta$
5.2	5.1							$^1,^3\Sigma^-$
5.6	5.6		5.53	5.53	5.35	5.5	5.54	$^1\Delta$
	6.25							
6.9	6.9				6.8			$^3\pi$
7.4	7.4		7.36	7.36	7.35	7.4	7.44	$^1\pi$
	7.7	7.59						$^3\pi$
8.2	8.2		8.11	8.11	8.05	8.1	8.12	$^1\Sigma^+$
				9.11				
	9.3							
	9.7	9.6		9.59				Rydberg II
				10.07				

ionisation potential = 11.25 eV (ref. 167)

CHAPTER 6

CONCLUSION

CHAPTER 6

CONCLUSION

We now have a versatile electron scattering spectrometer with a demonstrated ability to probe inelastic excitation cross-sections close to threshold. These processes, both direct and resonance enhanced, may be studied in

(a) constant residual electron energy spectra

(b) constant electron energy loss traces

(c) energy loss spectra at fixed incident energy

(d) composite (ΔE_{in} + ΔW), constant residual electron energy spectra

and (e) electron transmission spectra.

We have studied the ionisation of helium close to threshold in a new fixed incident electron energy mode. The discrepancy between our results and those of Pichou et al., if real, is important, as is our ability to place the excitation functions of helium on an absolute basis.

The energy resolution of the instrument, however, falls short of our expectations. The reasons for this are being investigated and a new trochoidal electron monochromator has been designed and built. Appendix IV contains details.

We feel that to fully realise the potential of our spectrometer, a data handling system for accumulation and analysis of results, perhaps based on an Apple microcomputer, will be necessary. This would allow us to operate with increased sensitivity and resolution at reduced sample pressures and electron beam currents. A more detailed study of nitrogen

would then be possible without the restrictions enforced, at the moment, by secondary inelastic collisions via the $^2\pi_g$ resonance.

Preliminary computer studies on the operation of the d.c. electron trap have been encouraging. This approach is being extended and developed to simulate a.c. trap operation in its various modes.

APPENDIX (I)

Electrical equipment used:

Bryans X-Y Recorder

Solartron A220 DVM

Motor-driven Helipot: MP120 (Beckman helipot)

A.P.T. stabilised power supplies

V.G. ionisation gauge units

Edwards Peltier baffle power supply units

Magnet power supply (Stirling University STS)

Current stabilised filament supply (Stirling University STS)

Storage oscilloscope. Tektronix Inc. 560 series.

APPENDIX (II)

Construction materials

Electrodes - ARCAP AP4

Support tubes - stainless steel (Immac. V and EN58B)

Scattered electrode supports - quartz

Synthetic saphire for location and spacing

Corning machinable glass ceramic for miscellaneous bushes and insulators

Electrical wiring - fibre glass insulated copper

Phillips Thermocoax resistive heating cable, Inconel.

Filament - thoriated tungsten

APPENDIX (III)

ELECTRON TRAP PROG. FLOW DIAGRAM

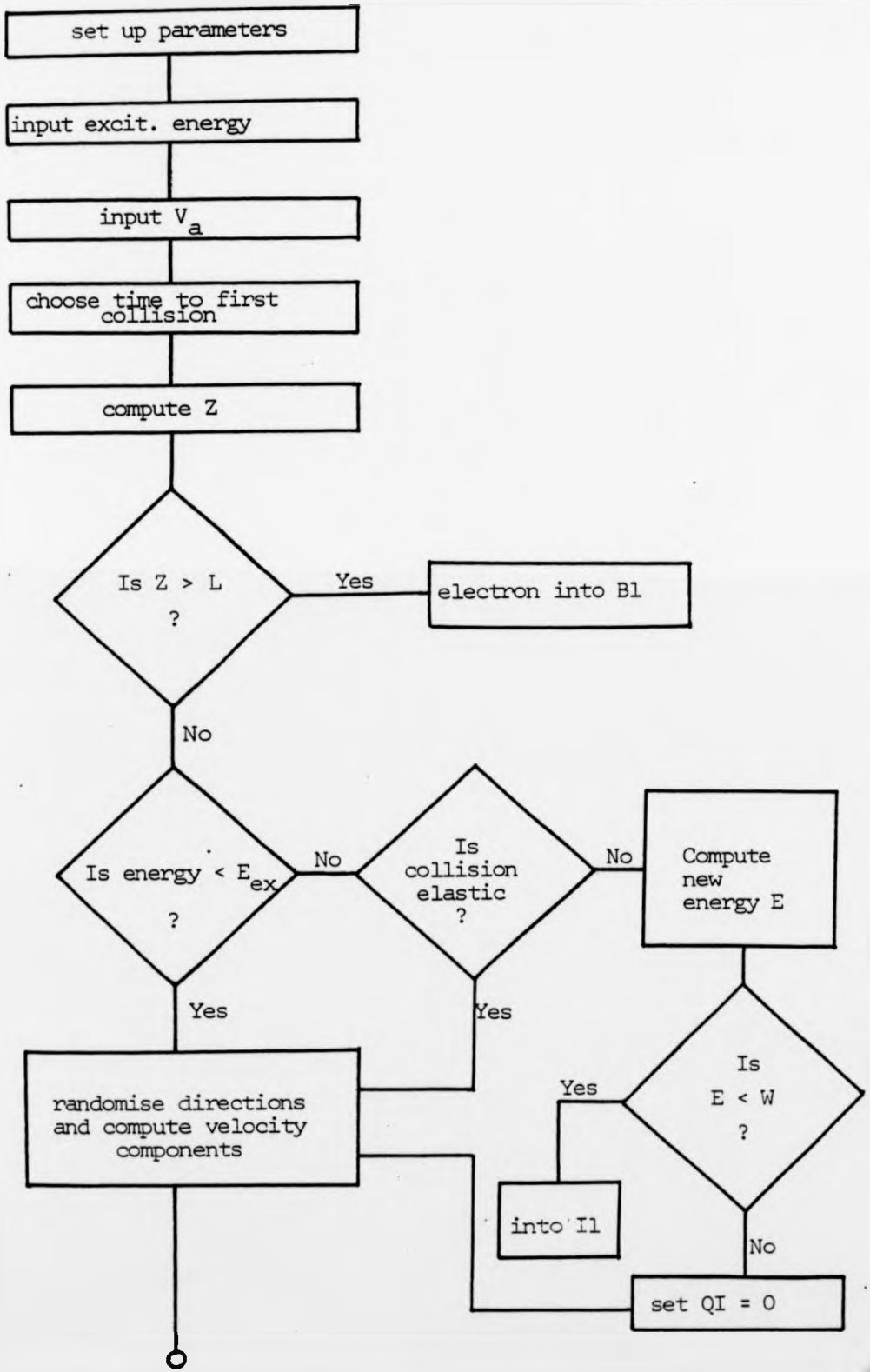

ELECTRON TRAP PROG. FLOW DIAGRAM (cont.)

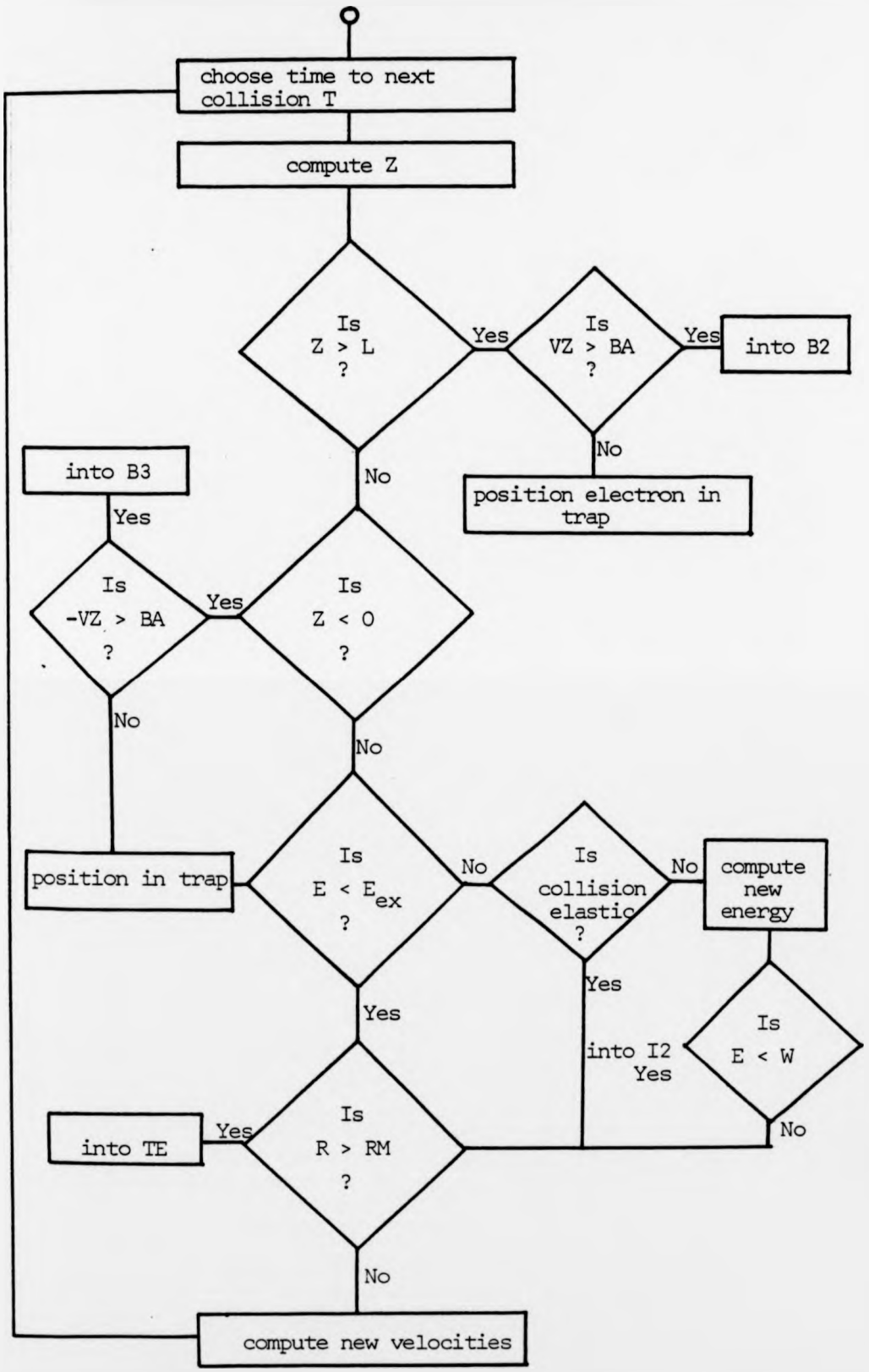

```
MTRAPVA      20-SEP-1981 16:20

100 EV=1.60291*10↑(-19)
110 ME=9.10956*10↑(-31)
120 NA=6.023*10↑23
130 RG=8.314
140 F=101325*NA/(760*RG)
150 L=.03
160 RN=.01
170 B=.01
200 INPUT"PRESSURE";PR
210 INPUT"TEMPERATURE";DK
220 INPUT"ACCELERATING VOLTAGE";VA
230 INPUT"EXCITATION ENERGY";EA
240INPUT"WELL-DEPTH";W
250 INPUT"ELASTIC X-SECTION";QE
260 INPUT"INELASTIC X-SECTION";QV
270 INPUT"NUMBER OF ELECTRONS";NTK
290 QE=QE*10↑(-20)
292 QV=QV*10↑(-20)
300 BA=SQR(2*W*EV/ME)
310 N=PR*F/DK
320 FW=ME/(B*EV)
350 TE=0
351 TX=0
352EL=0
353 B3=0
355B1=0
356B2=0
357 I1=0
358 I2=0
500 FOR K=1 TO NTK
502 ES=VA+W
504 QI=QV
506 IF ES<EA THEN QI=0
510X=0
511 Y=0
512 Z=0
515 CX1=0
520TT=0
521 ZT=0
530 KE=ES*EV
540VS=2*KE/ME
550 V=SQR(VS)
600 RANDOMIZE
610 P=RND
620Q=QE+QI
630 QR=QE/Q
640 T=-LOG(P)/(N*Q*V)
650 TT=TT+T
660 Z=Z+V*T
670IF Z>L GOTO 2000
680 IF ES<EA THEN GOTO 712
690 P=RND
700 IF QR<P GOTO 2100
712 P=RND
720TA=P*3.142
732 P=RND
740PHI=P*2*3.142
750CX2=SIN(TA)*COS(PHI)
760CY=SIN(TA)*SIN(PHI)
770 CZ=COS(TA)
780R1=0
800 VZ=CZ*V
810 VX=CX2*V
820VY=CY*V
832 P=RND
840 T=-LOG(P)/(N*Q*V)
850 Z=Z+VZ*T
860 IF Z>L THEN GOTO 2200
870 IF Z<W THEN GOTO 2410
880 IF ES<EA THEN GOTO 900
882 P=RND
890 IF QR<P GOTO 2300
900 RH=FW*SQR(VX↑2+VY↑2)
910 BN=SQR((1-CX2↑2)*(1-CX1↑2))+CX1*CX2
920R= SQR(R1↑2+RH↑2-2*R1*RH*BN)
930 IF R>RN GOTO 2400
940 CX1=CX2
942R1=R
952 P=RND
960 CX=P*3.142
972 P=RND
980 CY = P* 3.142
992 P=RND
1000CZ=P*3.142
1010 CX= COS(CX)
1020 CY = COS(CY)
1030 CZ= COS(CZ)
1040 C= SQR(CX↑2+CY↑2+CZ↑2)
1050CX2=CX/C
1060 CY=CY/C
1062CZ=CZ/C
1070 GOTO 800
2000B1=B1+1
```

APPENDIX (III) cont.

```
2010 GOTO 2500
2100 ES=ES-EA
2110 KE=ES+EV
2120 VS=2*KE/ME
2130 V=SQR(VS)
2140 IF ES<W THEN I1=I1+1
2150 IF ES<W GOTO 2500
2160 QI=0
2162 Q=QE
2164 QR=1
2170 GOTO 712
2190 GOTO 2500
2200 IF VZ>BA THEN B2=B2+1
2210 IF VZ>BA GOTO 2500
2220 G=INT(Z/L)
2222Z=(G+1)*L-Z
2230TX=TX+1
2240 GOTO 880
2300 ES=ES-EA
2305 IF ES<W THEN GOTO 2380
2310 KE=ES*EV
2320 VS=2*KE/ME
2330 VS =SQR(VS)
2360 QI=0
2362 Q=QE
2364 QR=1
2370 GOTO 900
2380 I2=I2+1
2385 GOTO 2500
2400TE=TE+1
2405 GOTO 2500
2410 IF -VZ>BA THEN GOTO 2440
2420 G=INT(-Z/L)
2430 Z=(G+1)*L+Z
2435 GOTO 880
2440 B3=B3+1
2500 NEXT K
3000 PRINT"PRESSURE ";PR
3005 PRINT"INCIDENT ENERGY";VA+W
3007 PRINT"RESIDUAL ENERGY";VA+W-EA
3008 PRINT
3010 PRINT"ELASTIC X-SECTION ";QE
3020 PRINT"INELASTIC X-SECTION ";QI
3025 PRINT
3030 PRINT"INELASTICALLY SCATTERED I1 ";I1
3035 PRINT"INELASTICALLY SCATTERED I2";I2
3040 PRINT"STRAIGHT THRO ELECTRONS ";B1
3045 PRINT"BC AFTER COLLISION";B2
3050 PRINT"ELECTRONS STOPPED AT EXIT";TX
3060 PRINT"ELASTICALLY TRAPPED";TE
3065 PRINT"TOTAL BEAM CURRENT";B1+B2
 3070 PRINT"BACKSCATTERED ELECTRONS";B3
3072 PRINT"DERIVED INELASTIC X-SECTION I1";I1/(NTR+N*L)
3074 PRINT"ERIVED INELASTIC X-SECTION I1+I2 ";(I1+I2)/(NTR+N*L)
3080 PRINT "SQR(W/E) "; SQR(W/ES)
3085 PRINT
4000 INPUT"CONTINUE Y/N";A$
4010 IF A$="Y" GOTO 4050
4020 GOTO 5000
4050 INPUT"NEW VA ";VA
4060 GOTO 300
5000 END

Ready
```

APPENDIX (IV)

T. E. M. mk II

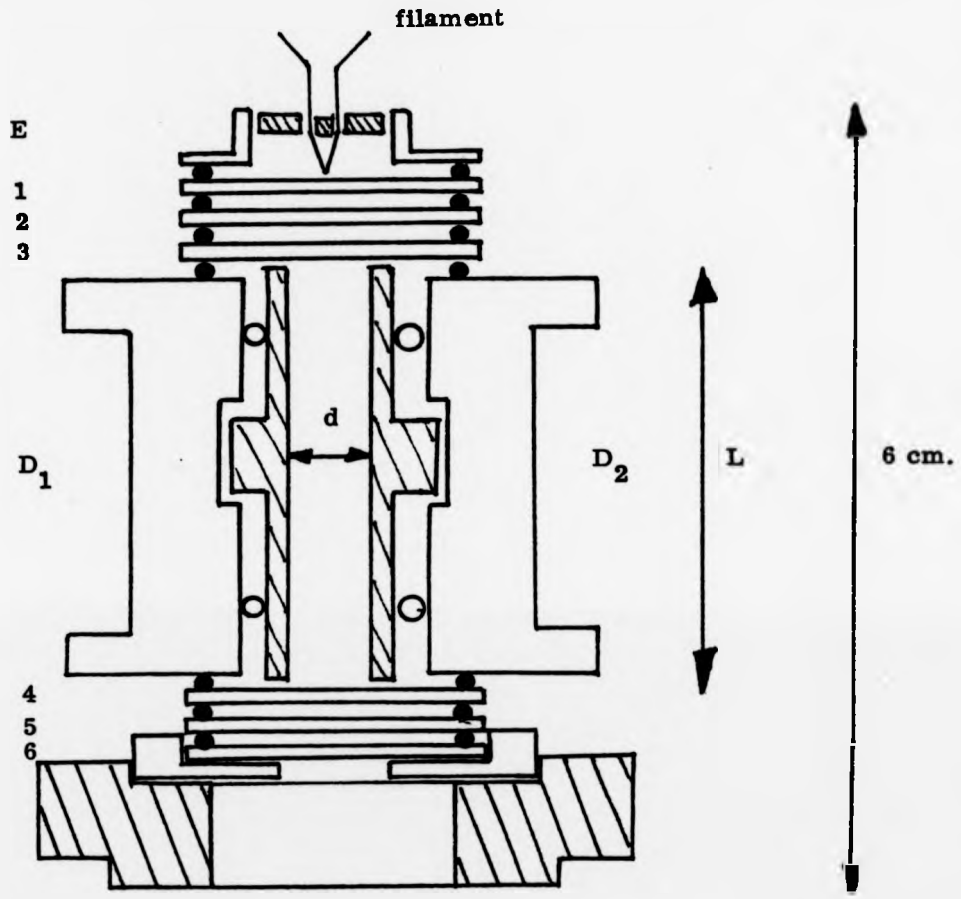

E	1	2	3	4	5	6
Aperture (mm)	1	1	0.5	1	1	2

D_1 -D_2 : L=30 mm. d = 3.6 mm.

BIBLIOGRAPHY

1. D. E. Golden and M. Ormonde, U.S. Patent 4,121,176 (1978)
2. N. J. Turro, J.Chem.Ed. 46, 2, (1969)
3. R. H. Huddlestone and S. L. Leonard, "Plasma Diagnostic Techniques", New York; Academic Press, (1965)
4. L. G. Christophorou and R. N. Compton, Health Physics 13, 1277, (1967)
5. R. S. Stolarski and N. P. Johnson, J.Atmos. and Terrestial Phys. 34, 1691, (1972)
6. A.E.S. Green and R. S. Stolarski, J.Atmos. and Terrestial Phys. 34, 1703, (1972)
7. J. B. Hasted, "Physics of Atomic Collisions", 2nd Edn. London; Butterworths, (1972)
8. A. Kuppermann, J. K. Rice and S. Trajmar, J.Phys.Chem. 72, 3894, (1968)
9. M. Born, Z.Phys. 37, 863, (1926); " 38, 803, (1926).
10. J. R. Oppenheimer, Phys.Rev. 32, 361, (1928)
11. D. F. Dance and I. C. Walker, Proc.R.Soc.Lond.A 334, 259, (1973)
12. D. F. Dance, G. A. Keenan and I. C. Walker, J.Chem.Soc.Faraday Trans.II, 74, 440, (1978)
13. A. Kuppermann, W. M. Flicker and O. A. Mosher, Chem.Rev. 79(1), 77, (1979)
14. G. J. Schulz, Rev.Mod.Phys. 45(3), 378, (1973)
15. ibid. 45(3), 423, (1973)
16. J. N. Bardsley and F. Mandl, Rep.Progr.Phys. 31(2), 471, (1968)

16a. R. McDiarmid and J. P. Doering, J.Chem.Phys. 73(9), 4192, (1980)

17. H. S. Taylor, Advan.Chem.Phys. 38, 91, (1970)

18. A. Herzenberg, J.Chem.Phys. 51, 4942, (1969)

19. G. J. Schulz and R. K. Asundi, Phys.Rev. 158, 25, (1967)

20. J. N. Bardsley, A. Herzenberg and F. Mandl, Proc.Phys.Soc.Lond. 89, 321, (1966)

21. G. J. Schulz and S. F. Wong, Phys.Rev.Lett. 35(21), 1429, (1975)

22. F. Linder and H. Schmidt, Z.Naturforsch, 26a, 1617, (1971

23. I. C. Walker, A. Stamatovic and S. F. Wong, J.Chem.Phys. 69(12), 5532, (1978)

24. G. J. Schulz, Phys.Rev. 125, 229 (1962)
" " 135, A988 (1964)

25. D. T. Birtwistle and A. Herzenberg, J.Phys.B. 4, 53, (197

26. D. Spence, Phys.Rev.A. 10(4), 1045, (1974)

27. G. J. Schulz, "Principles of Laser Plasmas", ed. G. Bekefi, John Wiley, New York, (1976)

28. K. D. Jordan and P. D. Burrow, Accounts of Chem.Res. 11, 341, (1978)

29. I. Nenner and G. J. Schulz, J.Chem.Phys. 62(5), 1747, (197

30. K. D. Jordan, J. A. Michejda and P. D. Burrow, Chem.Phys.Lett. 42, 227, (1976)

31. K. N. Houk and L. L. Munchausen, J.A.C.S. 98(4), 937, (197

32. K. N. Houk, Accounts Chem.Res. 8(11), 361, (1975)

33. I. Nenner, Ph.D. Thesis (Universite de Paris-Sud) (1975)

34. C. A. Coulson, B. O'Leary and R. B. Mallion, "Hückel Theory for Organic Chemists", Academic Press, London, (197

35. M. Polyani, "Atomic Reactions", Williams & Norgate, London (1932)

36. D. R. Herschbach, Adv.Chem.Phys. Vol.X, 368, (1966)

37. N. F. Lane, Rev.Mod.Phys. 52(1), 29, (1980)

38. R. D. Young, Phys.Rev. 113, 110, (1959)

39. J. B. Hasted, Contemp.Phys. 14, 357, (1973)

40. A. Stamatovic and G. J. Schulz, Rev.Sci.Instrum. 41, 423, (1970)

41. L. Sanche and G. J. Schulz, Phys.Rev. A6, 69, (1972)

42. E. H. Van Veen, W. L. Van Dijk and H. H. Brongersma, Chem.Phys. 16, 337, (1976)

43. J. R. Frazier, L. G. Christophorou, J. G. Carter and H. C. Schweinler, J.Chem.Phys. 69(8), 3807, (1978)

44. W.-C. Tam and S. F. Wong, Rev.Sci.Instrum. 50(3), 302, (1979)

45. G. J. Schulz, Phys.Rev. 112, 150, (1958)

46. F.W.E. Knoop, Ph.D. Thesis (Leyden), (1972)

47. F. H. Read, J.Phys.B (Proc.Phys.Soc.), Ser.II, Vol.I, 893, (1968)

48. K. D. Jordan, J. A. Michejda and P. D. Burrow, J.A.C.S. 98, 1295, (1976)

49. L. Sanche and G. J. Schulz, Phys.Rev.Lett. 26, 943, (1971)

50. L. Sanche and G. J. Schulz, Phys.Rev.Lett. 27, 1333, (1971)

51. L. Sanche and G. J. Schulz, J.Chem.Phys. 58, 479, (1973)

52. K. D. Jordan, J. A. Michejda and P. D. Burrow, J.A.C.S. 98, 7189, (1976)

53. P. D. Burrow, J. A. Michejda and K. D. Jordan, J.A.C.S. 98, 6392, (1976)

54. P. D. Burrow and K. D. Jordan, Chem.Phys.Lett. 36, 594, (1975)

55. E. H. Van Veen, Chem.Phys.Lett. 41, 535, (1976)

56. P. D. Burrow and J. A. Michejda, Chem.Phys.Lett. 42, 223, (1976)

57. G. J. Verhaart, W. J. Van der Hart and H. H. Brongersma, Chem.Phys. 34, 161, (1978)

58. R. I. Hall, J. Mazeau, J. Reinhardt and C. Schermann, J.Phys.B:Atom.Molec.Phys. 3, 991, (1970)

59. J. T. Dowell and T. E. Sharp, J.Chem.Phys. 47(12), 5068, (1967)

60. P. D. Burrow and G. J. Schulz, Phys.Rev. 187(1), 97, (1969)

61. H. H. Brongersma, A.J.H. Boerboom and J. Kistemaker, Physica, 44, 449, (1969)

62. C. R. Bowman and W. D. Miller, J.Chem.Phys. 42(2), 681, (1965)

63. G. J. Schulz and J. T. Dowell, Phys.Rev. 128(1), 174, (1962)

64. J. Bensimon, M. Cotte, J. F. Pedenan and C. Regnaut, Phys.Lett. 30A(4), 255, (1969)

65. R. N. Compton, J. A. Stockdale and P. W. Reinhardt, Phys.Rev. 180(1), 111, (1969)

66. M. N. Pisanias, L. G. Christophorou, J. G. Carter and D. L. McCorkle, J.Chem.Phys. 58(5), 2110, (1973)

67. L. G. Christophorou, D. L. McCorkle and J. G. Carter, J.Chem.Phys. 60(10), 3779, (1974)

68. J. T. Grissom, R. N. Compton and W. R. Garrett, Phys.Rev.A. 6(3), 977, (1972)

69. E. Manguelle Dicoum, Fr. Tran Minh and J. Bensimon, J.Phys.B:Atom.Molec.Phys. 6, L27, (1973)

70. D. F. Dance and I. C. Walker, J.Chem.Soc., Faraday Transactions II, 71, 1903, (1975).

71. D. F. Dance and I. C. Walker, Chem.Phys.Lett. 18(4), 601, (1973)

72. P. D. Burrow and G. J. Schulz, Phys.Rev.Lett. 22(24), 1271, (1969)

73. D. Spence, J.Phys.B:Atom.Molec.Phys. 13, L73, (1980)

74. G. J. Verhaart, P. Brasem and H. H. Brongersma, Chem.Phys.Lett. 62(3), 519, (1979)

75. G. J. Verhaart and H. H. Brongersma, Chem.Phys.Lett. 72(1), 176, (1980)

76. E. H. Van Veen and F. L. Plantenga, Chem.Phys.Lett. 30(1), 28, (1975)

77. E. H. Van Veen, Chem.Phys.Lett. 41(3), 540, (1976)

78. H. H. Brongersma, F.W.E. Knoop and C. Backx, Chem.Phys.Lett. 13(1), 16, (1972)

79. F.W.E. Knoop, H. H. Brongersma and L. J. Oosterhoff, Chem.Phys.Lett. 13(1), 20, (1972)

80. E. H. Van Veen and F. L. Plantenga, Chem.Phys.Lett. 38(3), 493, (1976)

81. G. J. Schulz, Phys.Rev. 116(5), 1141, (1959)

82. G. J. Schulz, J.Chem.Phys. 33(6), 1661, (1960)

83. G. J. Schulz, J.Chem.Phys. 34(5), 1778, (1961)

84. H. H. Brongersma and L. J. Oosterhoff, Chem.Phys.Lett. 1, 169, (1967)

85. M. N. Pisanias, L. G. Christophorou and J. G. Carter, Chem.Phys.Lett. 13, 433, (1972)

86. M. N. Pisanias, L. G. Christophorou and J. G. Carter, Bull.Am.Phys.Soc.Ser.II, 16, 1347, (1971)

87. J. A. Michejda, Ph.D. Thesis (Univ.Yale), (197)

88. H. H. Brongersma, Ph.D. Thesis (Univ.Leyden), (1968)

89. M. N. Pisanias, Ph.D. Thesis (Univ.Tennessee), (1972)

90. R. I. Hall, Ph.D. Thesis (Univ.London), (1971)

91. D. F. Dance and I. C. Walker, Unpublished results.

92. L. G. Christophorou, D. L. McCorkle and J. G. Carter, Excited States Biol.Mol., Proc.Int.Conf. (1974) pub. (1976) ed. J. B. Birks.

93. J. Bensimon, M. Cotte, Ph.Lemaire, J. F. Pedenon, R. Poitterin, A. Pozwolski and Fr. Tran Minh, 3e Colloque Nat.Phys.Coll.Atom. et Electr., Toulouse (1969)

94. R. D. Rempt, Ph.D. Thesis (Univ.California), (1969)

95. R. D. Rempt, Phys.Rev.Lett. 22(20), 1034, (1969)

96. R. I. Hall, J. Mazeau and J. Reinhardt, Compt Rendus, 266B, 774, (1968)

97. R. D. Rempt, U.S.Govt.Res.Develop.Rep. 70(2), 66, (1970)

98. P. D. Burrow, Phys.Rev.A. 2(5), 1774, (1970)

99. D. Spence, J. L. Mauer and G. J. Schulz, J.Chem.Phys. 57(12), 5516, (1972)

100. D. Spence, R. H. Huebner and P. D. Burrow, Bull.Am.Phys.Soc. 23, 143, (1978)

101. D. Spence and R. H. Huebner, Bull.Am.Phys.Soc. 23, 143, (1978)

102. D. Spence, J.Phys.B:Atom.Molec.Phys. 13(8), 1611, (1980)

103. G. J. Verhaart and H. H. Brongersma, Chem.Phys.Lett. 71(2), 345, (1980)

104. F.W.E. Knoop, H. H. Brongersma and A.J.H. Boerboom, Chem.Phys.Lett. 5(8), 450, (1970)

105. F.W.E. Knoop and J. Kistemaker, Phys.Lett. 46A(1), 27, (1973)

106. D. Spence and P. D. Burrow, J.Phys.B:Atom.Molec.Phys. 12(5), L179, (1979)

107. D. Spence, Phys.Rev.A. 11(5), 1539, (1975)

108. D. Spence, Phys.Rev.A. 12(6), 2353, (1975)

109. J. C. Giordan, M. R. McMillan, J. H. Moore and S. W. Staley, J.A.C.S. 102, 4870, (1980)

110a. D. Spence, J.Phys.B.Atom.Molec.Phys. 11(7), L243, (1978)

110b. D. Spence, Comm.Atom Molec.Phys. 5, 159, (1976)

110c. D. Spence, J.Phys.B.Atom.Molec.Phys. 14, 129, (1981)

110d. D. Spence, J.Chem.Phys. 74(7), 3898, (1981)

110e. D. Spence and P. D. Burrow, J.Phys.B.Atom.Molec.Phys. 13, 2809, (1980)

111a. D. F. Dance and I. C. Walker, J.Chem.Soc.Faraday Trans.II, 70, 1426, (1974)

111b. J. Reinhardt, R. I. Hall, G. Joyez and J. Mazeau, J.Phys.B.Atom.Molec.Phys. 4(8), L61, (1971)

111c. G. J. Verhaart and H. H. Brongersma, Chem.Phys. 52, 431, (1980)

112. A. Stamatovic and G. J. Schulz, Rev.Sci.Instrum. 39, 1752, (1968)

113. L. Page and N. I. Adams, Jr., "Electrodynamics" (Chapman & Hall Ltd., London) (1941)

114. H.S.W. Massey and H. Kestelman, "Ancillary Mathematics", (Sir Isaac Pitman & Sons Ltd., London) (1959)

115. J. R. Pierce, "Theory of Design of Electron Beams" (D. van Nostrand Co.Inc., New York) (1954)

116. D. Roy, Rev.Sci.Instrum. 43, 535, (1972)

117. J. A. Simpson, "Methods of Experimental Physics" 4A (Academic Press Inc., New York) (1967)

118. R. W. Hayward, "Advan. Electronics", 5, 104, (1953)

119. G. J. Verhaart, Ph.D. Thesis, Univ. of Leyden (1980)

120. M. R. McMillan and J. H. Moore, Rev.Sci.Instrum., 51(7), 944, (1980)

121. W. C. Martin, J.Phys.Chem.Ref.Data, 2, 257, (1973)

122. J.N.H. Brunt, G. C. King and F. H. Read, J.Phys.B:Atom.Molec.Phys., 10, 433, (1977)

123. R. S. Oberoi and R. K. Nesbet, Phys.Rev.A., 8(6), 2969, (1973)

124. R. K. Nesbet, J.Phys.B:Atom.Molec.Phys., 11(1), L21, (1978)

125. D.W.O. Heddle, R.G.W. Keesing and A. Parkin, Proc.R.Soc.Lond.A, 352, 419, (1977)

126. F. Pichou, A. Huetz, G. Joyez, M. Landau and J. Mazeau, J.Phys.B:Atom.Molec.Phys., 9, 933, (1976)

127. D. Andrick, J.Phys.B:Atom.Molec.Phys., 12(5), L175, (1979)

128. F. H. Read, Proc.IX ICPEAC, Seattle, (1975) ed. J. S. Risley and R. Geballe, p.176.

129. G. H. Wannier, Phys.Rev., 90, 817, (1953)

130. R. Peterkop, J.Phys.B:Atom.Molec.Phys., 4, 513, (1971)

131. A.R.P. Rau, Phys.Rev.A., 4, 207 (1971)

132. S. Cvejanovic and F. H. Read, J.Phys.B:Atom.Molec.Phys., 7(14), 1841, (1974)

133. P. Marchand, C. Paquet and P. Marmet, Phys.Rev., 180, 123, (1969)

134. P. G. Burke, J. W. Cooper and S. Ormonde, Phys.Rev., 183, 245, (1969)

135. F. Pichou, A. Huetz, G. Joyez and M. Landau, J.Phys.B:Atom.Molec.Phys., 11(21), 3683, (1978)

136. H. Ehrhardt, K. H. Hesselbacher, K. Jung and K. Willmann, J.Phys.B:Atom.Molec.Phys., 5, 1559, (1972)

137. H. Klar, Proc.Euro.Conf.Atom.Phys., Heidelberg (1981) Section M23, p.737.

138. D. Rapp and P. Englander-Golden, J.Chem.Phys., 43, 1464, (1965)

139. A. R. Johnston and P. D. Burrow, Proc.XII ICPEAC, Gatlinberg, (1981) Vol.1, p.140

140. R. J. Fleming and G. S. Higginson, Proc.Phys.Soc., 84, 531, (1964)

141. H. K. Holt and R. Krotkov, Phys.Rev., 144, 82, (1966)

142. W. L. Borst, Phys.Rev.A., 9, 1195, (1974)

143. G. J. Schulz and R. E. Fox, Phys.Rev., 106, 1179, (1957)

144. H. Maier-Leibnitz, Z.Phys., 95, 499, (1935)

145. K. A. Berrington, P. G. Burke and A. L. Sinfailam, J.Phys.B:Atom.Molec.Phys., 8, 1459, (1975)

146. P. G. Burke, unpublished results cited in ref. 108.

147. S. Cvejanovic, J. Comer and F. H. Read, J.Phys.B:Atom.Molec.Phys., 7, 468, (1974)

148. A. Chutjian and L. D. Thomas, Phys.Rev.A., 11(5), 1583, (1975)

149. J. G. Showalter and R. B. Kay, Phys.Rev.A., 11(6), 1899, (1975)

150. R. I. Hall, J. Reinhardt, G. Joyez and J. Mazeau, J.Phys.B:Atom.Molec.Phys., 5, 66, (1972)

151a. F. J. de Heer and R. H. Jansen, J.Phys.B:Atom.Molec.Phys., 10(18), 3741, (1977)

151b. D. F. Register, S. Trajmar and S. K. Srivastava, Phys.Rev.A., 21(4), 1134, (1980)

152. J. T. Dowell, Ph.D. Thesis, University of California (1965)

153. F.M.J. Pichanick and J. A. Simpson, Phys.Rev., 168, 64, (1968)

154. W. C. Fon, K. A. Berrington, P. G. Burke and A. E. Kingston, J.Phys.B:Atom.Molec.Phys., 12(11), 1861, (1979)

155a. W. Benesh, J. T. Vanderslice, S. G. Tilford and P. G. Wilkinson, Astrophys.J., 142, 1227, (1965).

155b. R. S. Mulliken, "The Threshold of Space", ed. M. Zelikoff, (New York: Pergamon) (1957).

156. D. G. Wilden, P. J. Hicks and J. Comer, J.Phys.B:Atom.Molec.Phys., 12(9), 1579, (1979)

157. A. Huetz, F. Gresteau and J. Mazeau, J.Phys.B:Atom.Molec. Phys., 13, 3275, (1980)

158. J. Mazeau, F. Gresteau, R. I. Hall, G. Joyez and J. Reinhardt, J.Phys.B:Atom.Molec.Phys., 6, 862, (1973)

159. J.N.H. Brunt, G. C. King and F. H. Read, J.Phys.B:Atom. Molec.Phys., 11(1), 173, (1978)

160. J. Mazeau, R. I. Hall, G. Joyez, M. Landau and J. Reinhardt, J.Phys.B:Atom.Molec.Phys., 6, 873, (1973)

161. S. A. Lawton and F. M. Pichanick, Phys.Rev.A., 7, 1004, (1973)

162. D. E. Golden, D. J. Burns and V. C. Sutcliffe, Jr., Phys.Rev.A., 10, 2123, (1974)

163. S. Trajmar, D. C. Cartwright, A. Chutjian and W. Williams, Phys.Rev.A., 16(3), 1041, (1977)

164. R. S. Stolarski and A. E. Green, J.Geophys.Res., 72, 3967, (1967)

165. C. E. Moore, Atomic Energy Levels, Vol.2 (N.B.S. Circular No. 467), (1952)

166. M.-J. Hubin-Franskin and J. E. Collin, J.Electr.Spectr. Related Phenomena, 7, 139, (1975)

167. V. Y. Foo, C. E. Brion and J. B. Hasted, Proc.Roy.Soc.A., 322, 535, (1971)

168. R. I. Hall, A. Chutjian and S. Trajmar, J.Phys.B:Atom.Molec.Phys., 6, L264, (1973)

169. J. W. Rabelais, J. M. McDonald, V. Scherr and S. P. McGlynn, Chem.Rev., 71, 73, (1971)

170. N. W. Winter, C. F. Bender and W. A. Goddard, III., Chem.Phys.Letts., 20, 489, (1973)

171. W. M. Flicker, O. A. Mosher and A. Kuppermann, J.Chem.Phys., 69(9), 3911, (1978)

172. D. G. Wilden and J. Comer, Chem.Phys., 53, 77, (1980)

173. R. S. Mulliken, Can.J.Chem., 36, 10, (1958)

174. K. Fukui, I. Fujita and K. Kuwata, Mass.Spec.(Japan), 23(2), 105, (1975)

175. M.-J. Hubin-Franskin and J. E. Collin, Bull.Soc.R.Sci.(Liège), 40, 361, (1971)

176. M. G. Lynch and D. Dill, J.Chem.Phys., 71(11), 4249, (1979)

177. D. Roy, M.-J. Hubin-Franskin, B. Leclerc, A. Paulin and J. Delwiche, Proc.XII ICPEAC, Gatlinberg, Tennessee (1981), p.362

178. C. Szmytkowski and M. Zubek, Chem.Phys.Lett., 57(1), 105, (1978)

Acknowledgements

Firstly, I wish to record my gratitude to Dr. Isobel Walker for supervising this research and for her encouragement and guidance throughout. I thank Mr. Don Dance for his assistance and advice in many stages of this work, and also the members of Shared Technical Services for their technical advice and cooperation, in particular Messrs. Bill Stirling, Brian Povey, Willie Grant and the late Joe Jason. Finally, I record my appreciation to Professor J.M.G. Cowie for financial support and laboratory facilities, and the SRC for a maintenance grant.

Attention is drawn to the fact that the copyright of this thesis rests with its author.

This copy of the thesis has been supplied on condition that anyone who consults it is understood to recognise that its copyright rests with its author and that no quotation from the thesis and no information derived from it may be published without the author's prior written consent.

4 26 89'8 2

END